UNIVERSITY OF CALIFORNIA SAN DIEGO

Atomic Layer Deposition for Continued Scaling of Interconnects

A dissertation submitted in partial satisfaction of the requirements for the degree Doctor of Philosophy

in

Materials Science and Engineering

by

Michael Christopher Breeden

Committee in charge:

Professor Andrew C. Kummel, Chair
Professor Prabhakar Bandaru, Co-chair
Professor William Trogler
Professor Wei Xiong

2022

The dissertation of Michael Christopher Breeden is approved, and it is acceptable in quality and form for publication on microfilm and electronically.

University of California San Diego

2022

DEDICATION

To my friends, family, and labmates, for always supporting me.

EPIGRAPH

Any sufficiently advanced technology is indistinguishable from magic.

Arthur C. Clarke

If you ever code something that “feels like a hack but it works”, just remember that a CPU is literally a rock that we tricked into thinking.

Anonymous

TABLE OF CONTENTS

LIST OF SYMBOLS AND ABBREVIATIONS

Å	angstrom
AC	alternating current
AFM	atomic force microscopy
ALD	atomic layer deposition
BEOL	back-end-of-line
C	capacitance
CMOS	complementary metal-oxide-semiconductor
CMP	chemical-mechanical polishing
C-V	capacitance-voltage
CVD	chemical vapor deposition
DC	direct current
D_{it}	interface trap state density
DMADMS	dimethylamino-dimethylsilazane
EELS	electron energy loss spectroscopy
FEOL	front-end-of-line
FGA	forming gas anneal
G-V	conductance-voltage
HF	hydrofluoric acid
HRTEM	high-resolution transmission electron microscopy
I	electric current
I-V	current-voltage
MOL	middle-of-line

MOCVD	metalorganic chemical vapor deposition
MOS	metal-oxide-semiconductor
MOSCAP	metal-oxide-semiconductor capacitor
MOSFET	metal-oxide-semiconductor field-effect transistor
pBN	pyrolytic boron nitride
RF	radio frequency
SRC	Semiconductor Research Corporation
TDMAH	tetrakis(dimethylamino) hafnium
TMA	trimethylaluminum
TMDS	tetramethyl-disilazane
UHV	ultra-high vacuum
V	voltage
XPS	X-ray photoelectron spectroscopy
XRD	X-ray diffraction
XRR	X-ray reflectometry

LIST OF FIGURES

ACKNOWLEDGEMENTS

I would first like to acknowledge my advisor, Professor Andrew Kummel, for all of the guidance and support throughout my time in graduate school. Prof. Kummel's mentorship has helped me develop my research and engineering skills immensely, as well as given me valuable insight into the semiconductor industry. I appreciated the opportunity he has given me to present at several conferences and the connections I have made with people in the field. Additionally, Prof. Kummel's understanding and support offered when I was faced with personal issues gave me the motivation to press on, and I am eternally grateful for the opportunity he has given me to complete this journey.

Secondly, I would like to thank Dr. Steven Wolf for being a wonderful lab mate, mentor, and friend. Without his guidance on the fundamentals of vacuum science and patience in training me to maintain the vacuum chambers, I would have been lost. Our many hours spent interpreting data and preparing for our weekly group meetings has been valuable, and without his guidance on presenting at conferences, I would feel far less confident. I will also never forget the times we attended conferences together (especially at the bar), and random discussions in lab. I would also like to thank Victor Wang, a fellow colleague and friend over the past 3 years we have worked together. He has been an excellent learner and his assistance preparing samples, running depositions, and performing characterization on samples has been immensely helpful. His work ethic is second to none and I am confident he will be an excellent engineer.

Other former and current members of the Kummel group I would like to give thanks to are Dr. Christopher Ahles, Dr. Jong Choi, Dr. Scott Ueda, Dr. Iljo Kwak, Dr. Mahmut Kavrik, Dr. Evgeniy Chagarov, Aaron McLeod, Yunil Cho, James Huang, Ashay Anurag, Harshil Kashyap, Jimmy Kuo, Chelsea Swank, and Ping-che Lee. Whether at conference, in lab, or at the

bar after a long day in lab, it has been a pleasure working with them, and I will always treasure the times we have worked together on building and maintaining the lab equipment, chatted with while waiting on experiments in lab, or at the bar after a long day of conference talks.

I would also like to thank the many supporters in industry whom we have collaborated with: the SRC, TSMC, RASIRC, Applied Materials, and EMD Electronics. Their financial and technical support has been invaluable. I would especially like to thank Dan Alvarez and Jeff Spiegelman from RASIRC, from which the undergraduate internship I had at RASIRC was what motivated me to pursue graduate school in the first place. From UC San Diego, I would like to thank Dr. Fruhberger and the staff from Nano3, Kristen Itahara and Heather Sears from the Procurement office who helped immensely with payment issues and managing conference travel, and the Campus Research Machine Shop for helping me repair the many vacuum leaks that have developed during my research.

I want to also thank the members of my committee for their participation in and advice given for my senate exam and dissertation defense. My committee includes Professor Andrew Kummel, Professor Prabhakar Bandaru, Professor Wei Xiong, and Professor William Trogler.

Finally, I would like to thank my father, Daniel, for raising me with a curiosity in the sciences and technology, and to my mother, Virginia. Although she is no longer with us, I know she would be proud of me.

Chapter 2, in full, is a reprint of the material as it appears in Applied Surface Science: M. Breeden, S. Wolf, S. Ueda, Z. Fang, C.Y. Chang, K. Tang, P. McIntyre, A. C. Kummel. "*$Al_2O_3/Si_{0.7}Ge_{0.3}$(001) & $HfO_2/Si_{0.7}Ge_{0.3}$(001) Interface Trap State Reduction via In-Situ N_2/H_2 RF Downstream Plasma Passivation.*" Appl. Surf. Sci., 2019. **478**: p. 1065-1073. The dissertation author was the primary investigator and author of this paper.

Chapter 3, in full, is a reprint of the material as it appears in ACS Applied Nano Materials: M. Breeden, V. Wang, J. Spiegelman, A. Anurag, S. F. Wolf, D. Moser, R. K. Kanjolia, M. Moinpour, J. Woodruff, S. Nemani, K. Wong, C. H. Winter, A. C. Kummel. *Proximity Effects of the Selective Atomic Layer Deposition of Cobalt on the Nanoscale: Implications for Interconnects*. ACS Appl. Nano Mater., 2021. **4**: p. 8447-8454. The dissertation author was the primary investigator and author of this paper.

Chapter 4, in full, is currently being prepared for submission for publication of the material, and reprinted with permission from M. Breeden, V. Wang, R. Kanjolia, M. Moinpour, D. Moser, J. Woodruff, H. Simka, A. Jog, D. Gall, and A. C. Kummel. *Ruthenium atomic layer deposition with near-bulk resistivity for interconnects*. (manuscript in preparation). The dissertation author was the primary investigator and author of this paper.

VITA

EDUCATION

2016 Bachelor of Science in Chemical Engineering, University of California San Diego

2018 Master of Science in Materials Science and Engineering, University of California San Diego

2022 Doctor of Philosophy in Materials Science and Engineering, University of California San Diego

PUBLICATIONS

M. Breeden, V. Wang, R. Kanjolia, M. Moinpour, D. Moser, J. Woodruff, H. Simka, A. Jog, D. Gall, A. C. Kummel. *Ruthenium atomic layer deposition with near-bulk resistivity for interconnects*. (manuscript in preparation).

M. Breeden, V. Wang, J. Spiegelman, A. Anurag, S. F. Wolf, D. Moser, R. K. Kanjolia, M. Moinpour, J. Woodruff, S. Nemani, K. Wong, C. H. Winter, A. C. Kummel. *Proximity Effects of the Selective Atomic Layer Deposition of Cobalt on the Nanoscale: Implications for Interconnects*. ACS Appl. Nano Mater., 2021. **4**: p. 8447-8454.

M. Breeden, V. Wang, F. Yu and A. C. Kummel, *Grain Structure – Resistivity Relationship of Ru ALD Precursors*, Proceedings of VLSI-TSA (2021): pp. 1-2.

M.J. Li, M. Breeden, V. Wang, J. Hollin, N.M.K. Linn, C.H. Winter, A.C. Kummel, M.S. Bakir. *Cu-Cu Bonding Using Selective Cobalt Atomic Layer Deposition for 2.5-D/3-D Chip Integration Technologies*, IEEE Trans. Components, Packaging and Manufacturing Technology, 2020. **10**(12): p. 2125-2128

S. Wolf, M. Breeden, S. Ueda, J. Woodruff, M. Moinpour, R. Kanjolia, A.C. Kummel. *The role of oxide formation on insulating versus metallic substrates during Co and Ru selective ALD*. Appl. Surf. Sci., 2020. **510**: p. 144804

M. Breeden, S. Wolf, S. Ueda, Z. Fang, C. Chang, K. Tang, P. McIntyre, A.C. Kummel. *Al_2O_3 & $HfO_2/Si_{0.7}Ge_{0.3}$ Interface Trap State Reduction via In-Situ H_2/N_2 RF Downstream Plasma Passivation*. Appl. Surf. Sci., 2019. **478**: p. 1065-1073

S. Wolf, M. Breeden, I. Kwak, J. Park, M. Kavrik, M. Naik, D. Alvarez, J. Spiegelman, A.C. Kummel. *Low-temperature thermal ALD TaN_x and TiN_x films from anhydrous N_2H_4*. Appl. Surf. Sci., 2018. **462**: p. 1029-1035.

J.H. Park, S. Vishwanath, S. Wolf, K. Zhang, I. Kwak, M. Edmonds, M. Breeden, X. Liu, M. Dobrowolska, J. Furdyna., J.A. Robinson, H.G. Xing, A.C. Kummel. *Selective Chemical Response*

of Transition Metal Dichalcogenides and Metal Dichalcogenides in Ambient Conditions. ACS Appl. Mater. Interfaces. 2017. **9**: p. 29255–29264.

S. Sukrittanon, R. Liu, M. Breeden, J. L. Pan, K. L. Jungjohann, C. W. Tu, S. A. Dayeh. *Radial direct bandgap p-i-n GaNP microwire solar cells with enhanced short circuit current*. J. Appl. Phys., 2016. **120**: p. 055702

FIELD OF STUDY

Major Field: Materials Science and Engineering

Studies in Surface Science and Thin Film Deposition
Professor Andrew C. Kummel

ABSTRACT OF THE DISSERTATION

Atomic Layer Deposition for Continued Scaling of Interconnects

By

Michael Christopher Breeden

Doctor of Philosophy in Materials Science and Engineering

University of California San Diego, 2022

Professor Andrew C. Kummel, Chair

Professor Prabhakar Bandaru, Co-chair

With the need for more compute performance, smaller semiconductor device dimensions and denser interconnections have required the use of ultra-thin layers conformally deposited in three-dimensional structures such as the gate-all-around MOSFET and in high-aspect-ratio interconnect vias. Atomic layer deposition (ALD), with the ability to precisely control thickness as well as selectively deposit layers on different materials, is used in current process nodes for gate oxides and barrier layers, but new channel materials such as silicon-germanium (SiGe) and new

interconnect metals such as cobalt (Co) and ruthenium (Ru) require new surface preparation techniques and ALD processes.

Chapter 2 of this dissertation describes the passivation of defects in gate oxides deposited by ALD in SiGe-channel devices. SiGe's high carrier mobility shows promise for future devices, but the presence of unstable germanium oxides (GeO_x) in the interface between oxide and channel results in high defect densities, limiting device performance. By nitridating the surface prior to gate oxide ALD using an RF plasma, a reduction in defect densities is demonstrated. TEM and XPS studies confirmed the formation of a GeN_x interfacial layer suppressing GeO_x formation during ALD, improving gate oxide nucleation and decreasing defect densities.

With shrinking device dimensions, interconnect via widths correspondingly shrink. While copper has long been used for due to its low bulk resistivity, ultra-narrow (<10 nm) via widths show high resistance with Cu. Co has been proposed as an alternative as it maintains its resistivity to smaller widths, with several selective Co ALD processes developed. However, surface defects can result in unwanted deposition, and in Chapter 3, the passivation of surface defects to enhance selectivity of Co ALD is studied, with XPS and SEM studies showing that a low-temperature reflow process can further enhance selectivity. Ru is also a promising metal for interconnects due to its potential for a barrier-less via fill, and in Chapter 4, the deposition of Ru with a resistance close to the bulk value by ALD is demonstrated. XRD and TEM studies confirm the deposition of Ru layers with low O and C content and grain sizes similar to the film thickness, minimizing grain boundary scattering.

Chapter 1

Introduction

1.1 ALD for Transistor and Interconnect Scaling

To meet the needs of the modern computer industry, the scaling of metal-oxide-semiconductor field effect transistor (MOSFET) to smaller dimensions has resulted in the refinement of the MOSFET design from planar devices microns in size to the three-dimensional gate-all-around FETs with gate-to-gate pitches 30 nm across [1]. At the same time, the size and pitch of interconnects between transistors decreases, with 2 nm process nodes requiring the vias connecting each layer to be scaled under 10 nm in width [2]. To fabricate these devices, new channel materials such as silicon-germanium (SiGe) and replacement interconnect metals are desired [3] [4]. Atomic layer deposition (ALD), with its ability to finely control the growth of ultra-thin layers and deposit conformally even in three dimensional structures, is currently employed to deposit the gate oxides and interconnect barrier layers.

The goal of this dissertation is to highlight additional applications of ALD for the continued scaling of MOSFETs and the interconnects between them. With the use of higher-performance channel materials such as silicon-germanium (SiGe) comes an increase in interfacial defects introduced by gate oxide deposition. In Chapter 2, a method to passivate the defects present during gate oxide ALD on SiGe using an RF plasma to nitridate the surface prior to gate oxide deposition is demonstrated through electrical characterization and TEM and XPS studies of the SiGe-gate oxide interface.

Chapters 3 and 4 focus on the replacement of copper as interconnect metal with cobalt and ruthenium deposited by ALD. Copper's low bulk resistivity has made it the interconnect

metal of choice, but as via widths decrease, Cu vias increase in resistivity due to increased electron scattering. Cobalt and ruthenium have both been proposed as replacement metals for these vias as their shorter electron mean free paths allow it to maintain resistivity to smaller widths, with ruthenium also showing the promise for a barrier-less via fill. ALD processes for both metals exist, with selective ALD processes especially desired to enable bottom-up growth for a full via fill. In Chapter 3, a vapor-phase passivation method to improve the selectivity of the selective Co ALD process is demonstrated on a metal/dielectric pattern, while in Chapter 4, a low-resistivity Ru ALD process is demonstrated on metal and insulator surfaces to determine its suitability for process integration.

1.2 Basics of Atomic Layer Deposition

The key deposition technique to enable the deposition of the ultra-thin films in modern semiconductor devices is atomic layer deposition (ALD). As an offshoot of chemical vapor deposition (CVD), in which one or more precursors react to form the desired film on a surface, ALD relies on the principle of sequential, self-limiting reactions on surfaces [5]. The prototypical ALD process is illustrated in Figure 1.1 as a four-step process. First, a reactant (A) must react with the surface in a self-limiting manner, after which no additional deposition occurs. Second, the chamber must be purged or evacuated to eliminate the presence of reactant A in the gas phase. Third, a second reactant (B) is introduced to the chamber and reacts with the surface in a second self-limiting reaction, and in the fourth step the chamber is again purged or evacuated of reactant B, leaving the surface ready to react with reactant A. Together, these four processes comprise one ALD cycle, which can be run repeatedly to the desired thickness. Due to the self-limiting nature

of each half-cycle, the deposition rate is determined by the inherent adsorption and desorption characteristics of the precursors, allowing more control over the growth of ultra-thin films [6].

ALD processes exist for a wide variety of materials, from metal oxides and nitrides to metals [7] [8] [9]. Typical deposition temperatures vary with each process chemistry, but for most ALD processes a range of temperatures exists where the growth rate during deposition remains constant per cycle in what is known as the ALD temperature window [10]. Above this window, the growth rate may increase due to decomposition or decrease due to early precursor desorption, while growth rates below the window typically drop due to slow reaction kinetics. Furthermore, as ALD relies heavily on the chemical environment at the surface, differences in reactivity between surfaces can be exploited to deposit materials selectively in area-selective ALD (AS-ALD) [11]. In addition, the reliance on surface saturation allows deposition to occur uniformly even in high-aspect ratio trenches and three-dimensional structures. These processes have been exploited for a wide variety of applications, from the high-dielectric constant gate oxides used in modern MOSFETs [12] to the metals and metal nitrides used as barrier layers in interconnects [13].

1.3 Vacuum Chamber Design

As ALD and CVD processes are run under vacuum to prevent undesired vapor-phase reactions and control gas flows to minimize the amount of precursor necessary, the studies in Chapter 3 and 4 of this dissertation heavily relied upon the use of a multiple-chamber vacuum system for both deposition and film analysis (Scienta Omicron). This system, illustrated in Figure 1.2, consisted of a load lock for sample loading, two deposition chambers pumped down to a base pressure of ~10^{-6} Torr by means of a turbomolecular pump backed with a rotary mechanical pump,

and an analysis chamber held at ultra-high-vacuum (UHV, ~10^{-10} Torr) chamber with a pyrolytic boron nitride (pBN) sample heater and X-ray photoelectron spectroscopy (XPS) analysis system, with ion pumps and titanium sublimation pumps used to maintain the pressure at UHV conditions. Both deposition chambers contained a custom-fabricated heater to allow for sample heating without exposing heater elements to the process gases and conductive films deposited. By having deposition chambers attached to the analysis chamber, samples were transferred under vacuum to prevent air exposure between deposition and XPS analysis.

In addition to this main analysis and deposition chamber used in Chapters 3 and 4, the work presented in Chapter 2 was performed using a second system with a load lock and deposition chamber pumped by rotary mechanical pump for deposition of Al_2O_3 and HfO_2 by ALD, illustrated in Figure 1.3. An RF remote plasma source (PIE Scientific) with a sapphire tube was attached above the sample stage for surface functionalization.

1.4 X-ray Photoelectron Spectroscopy

As the surface condition is vital to understanding ALD processes, the work in this dissertation relied extensively on X-ray photoelectron spectroscopy (XPS). XPS takes advantage of the photoelectric effect to infer information regarding the chemical identity and state of atoms at or near (<5-10 nm) the surface of a sample. When a photon of energy *hv* strikes an atom, an electron is ejected with a specific kinetic energy defined by the binding energy of the electron, with a correction for the work function of the spectrometer [14]. Equation 1.4.1 rearranges this relationship in terms of the binding energy of the electron.

$$E_{binding} = h\nu - E_{kinetic} - \Phi_{spec} \tag{1.4.1}$$

Illustrated in Figure 1.4, a typical XPS system contains four components – the X-ray source, electrostatic lenses used to collect electrons emitted from the sample, an electron analyzer and detector. The X-ray source uses the thermionic emission of electrons from a heated filament to bombard an anode kept at high voltage (15 kV). The metal anode (in this work, Al) emits photons of characteristic energies; for Al, Al kα photons are emitted with an energy of 1486.7 eV. To filter out undesired emission lines and eliminate Bremsstrahlung radiation which can produce false satellite peak features and decrease energy resolution, the anode is aimed at a quartz crystal monochromator, which uses the Bragg condition for diffraction to reflect only Al kα photons [15]. The photons strike the sample and eject electrons with kinetic energies corresponding to binding energies for atoms present on the sample, which are then sent through electrostatic lenses to the hemispheric analyzer, consisting of two concentric hemispheric shells held at different voltages. Only electrons with specific energies defined by the pass energy will be accelerated all the way to the detector, with higher energy electrons striking the outer shell and lower energy electrons striking the inner shell. The collected electrons are then sent through photomultipliers and sent to a preamplifier for conversion to a kinetic energy spectrum. By varying the shell voltages, a full spectrum of binding energies can be captured [16].

The binding energies of an atom's electrons will shift based on its oxidation state. By comparison of the captured spectrum with a known calibration spectrum, this chemical shift can be measured. In addition, after identification of all atoms present on the sample, relative intensities can be compared to determine atomic fractions, which when combined with chemical shift information can determine material stoichiometry, making XPS a powerful tool for the study of surface reactions and composition [17].

1.5 MOSCAP Electrical Characterization

In Chapter 2 of this dissertation, interfacial defects present in an oxide layer with and without treatment were investigated. As the switching characteristics of a MOSFET are affected greatly by the quality of the oxide and its interface with the channel, a related structure, the MOS capacitor (MOSCAP), is fabricated to determine its capacitance- and current-voltage characteristics [18]. Figure 1.5 illustrates a cross-sectional diagram of the MOSCAP and the types of defects that may be present. The metal gate and the semiconductor channel act as parallel plates with a capacitance C_{ox}. In addition, the presence of charge in the semiconductor adds an additional contribution C_{SC}. These capacitances are treated in series as shown in Equation 1.5.1:

$$\frac{1}{C_{tot}} = \frac{1}{C_{ox}} + \frac{1}{C_{SC}} \tag{1.5.1}$$

In a MOSCAP, there are four regimes of operation: accumulation, flatband, depletion, and inversion. At flatband, the Fermi levels of the gate and semiconductor are equal, with a voltage V_{FB} determined by the difference in work function between the metal and semiconductor. For a p-type channel, when the gate voltage is below V_{FB}, the MOSCAP is operating in accumulation, where C_{SC} increases as voltage decreases due to the accumulation of charge at the semiconductor surface until $C_{SC} >> C_{ox}$, and therefore, $C_{tot} = C_{ox}$. Conversely, an increase in voltage will deplete the channel of holes, resulting in a widening depletion region, lowering C_{SC} (often referred to as C_D while in depletion) and therefore C_{tot}. Increasing voltage further results in an inversion of the majority carriers at the surface, until the concentration of electrons at the surface equals that of the holes in the semiconductor at flatband. After this point, the inversion charge increases, resulting in $C_{SC} >> C_{ox}$. However, at high frequencies, these carriers cannot respond quickly enough and the

widening depletion layer in the channel results in a minimum capacitance C_{min}, with the depletion capacitance and oxide capacitance in series.

Since the interface between the oxide and the semiconductor represents a discontinuity in the crystal lattice, the unfulfilled bonds represent energy levels that act as charges [19]. In an equivalent circuit model, this is represented in Equation 1.5.2 as an additional capacitor in parallel with C_{SC}, C_{it}.

$$\frac{1}{C_{tot}} = \frac{1}{C_{ox}} + \frac{1}{C_{SC}+C_{it}} \tag{1.5.2}$$

The conductance method is a powerful tool in measuring the density of these interface states. By rearranging the sum of C_{SC} and C_{it} as a capacitor C_P and resistor G_P, the new equivalent circuit model is that of an oxide capacitor in series with a capacitor and resistor in parallel, represented by the following equations [20]:

$$C_P = C_{SC} + \frac{C_{it}}{1+\omega^2\tau^2} \quad (1.5.3) \qquad \frac{G_p}{\omega} = \frac{C_{it}\omega\tau}{1+\omega^2\tau^2} \quad (1.5.4)$$

where $C_{it} = q^2 D_{it}$. By measuring the impedance of a MOSCAP in the depletion regime using an AC signal overlaid over a gate bias, these components can be measured and the interface state density, D_{it}, determined. In addition, models such as the distributed bulk-oxide trap model can be used to extract the densities of other defects such as border traps present in the gate oxide not captured by the conductance method [21].

1.6 Scanning & Transmission Electron Microscopy

Much of the work in this dissertation involved films and features too small for optical microscopy and relied on the use of scanning (SEM) and transmission electron microscopy (TEM) for surface imaging and chemical analysis of the films deposited [22]. In SEM, a beam of electrons generated by a tungsten filament or field emission gun are accelerated with a voltage of 1-30 kV through a series of electromagnetic lenses towards the sample under high vacuum ($<10^{-4}$ Torr). As the beam is rastered across the surface, the electrons interact with the sample to generate secondary electrons which are then collected by a biased grid to strike a scintillator, generating a photon sent through a photomultiplier to be interpreted as a pixel [23]. The primary electrons in the beam are also scattered and can either be collected by the same detector or by a detector mounted around the aperture of the beam.

By choosing which electrons to detect, valuable information on the morphology and chemical composition of the surface can be obtained. The incident electron strikes the sample and interacts over a volume depending on the voltage of the beam and the angle of incidence. The secondary electrons generated within the interaction volume are scattered with an intensity related to the angle of incidence, resulting in an image with high contrast based on the surface morphology. Backscattered primary electrons, conversely, are emitted proportionally to the Z-number of atoms present in the interaction volume, producing an image with contrast based on chemical composition. Furthermore, the interaction of electrons with atoms also generates both Bremsstrahlung and characteristic X-rays, which can be used to identify the chemical composition of areas on the surface in energy dispersive X-ray spectroscopy (EDS/EDX). However, spatial resolution of EDS in SEM is limited by the size of the interaction volume, typically on the order of ~ 1 μm [24].

In TEM, electrons are accelerated by a higher voltage (~100-300 kV) through additional electromagnetic lenses and transmitted through the sample. The transmitted electrons are then focused by lenses and either focused on a phosphor plate for live viewing or a charge-coupled device (CCD) which converts the electron signal to an image. The sample must be thin enough (~ 100 nm) to allow for sufficient electron transmission, but cross-sections can be prepared by focused ion beam (FIB) cross-sectioning [25]. Electrons can pass through a sample with or without scattering; in the bright-field imaging mode, a signal is collected proportionally to the amount of unscattered electrons, while in the dark-field imaging mode, only scattered electrons are detected. Elastically scattered electrons can constructively or destructively interfere to form a diffraction pattern, useful for crystallographic studies [26].

As with SEM, X-rays generated by electron-atom interactions can be used for chemical analysis with EDS. The thickness of the sample limits the size of the electron interaction volume, greatly improving spatial resolution, enabling the use of EDS for cross-sectional elemental analysis of the films deposited by ALD in this work. Additionally, the energy loss of electrons through inelastic scattering events can be used to infer physical and chemical characteristics of the sample through electron energy-loss spectroscopy (EELS) [27]. Energy loss due to core-electron scattering can be used to identify elemental composition and even chemical bonding information with potentially atomic-scale resolution, making EELS a powerful tool for studying ultra-thin films and their interfaces with materials used in modern semiconductor devices [28].

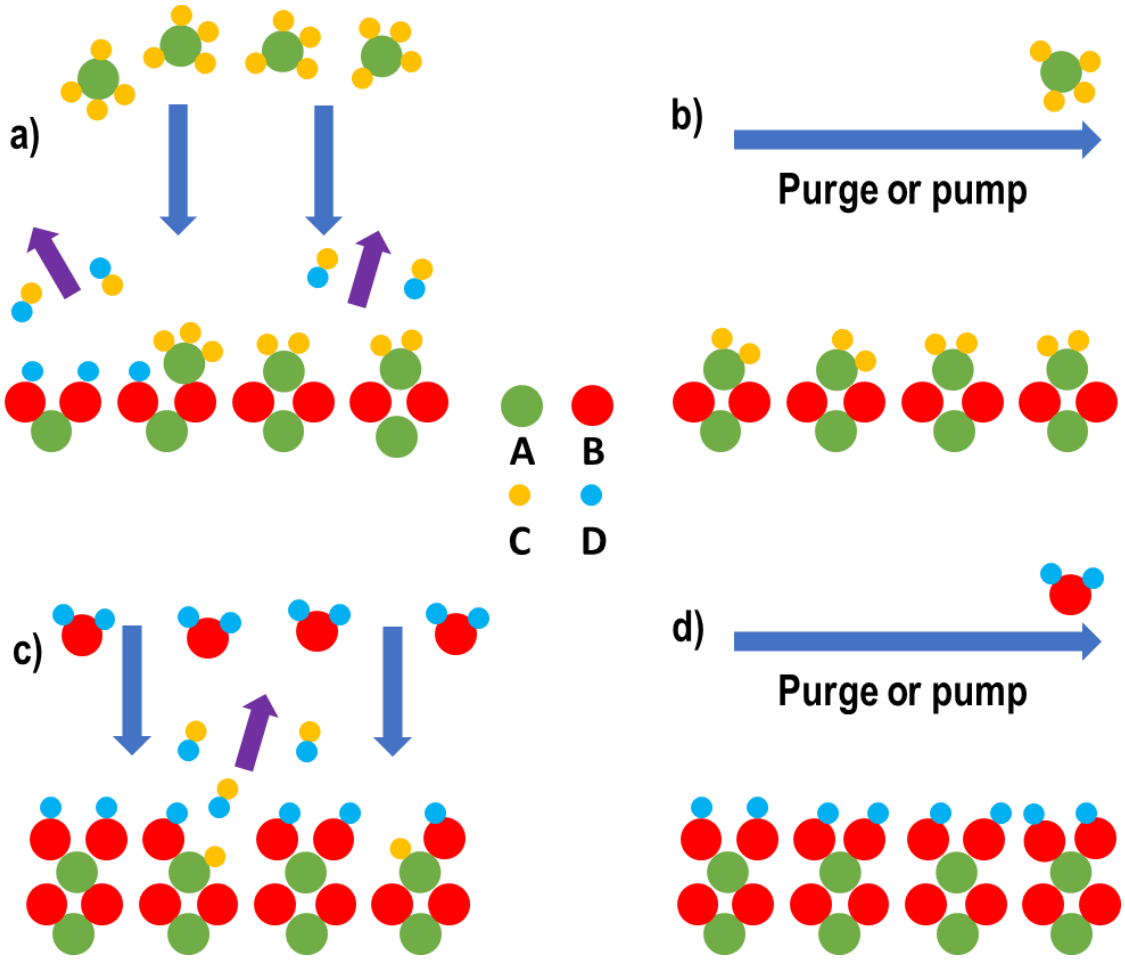

Figure 1.1: Schematic of a typical ALD process. Four phases: a) Gas-phase dosing of reactant AC_4 until saturation on a surface of AB_2 terminated by D (AB_2—D) from the previous cycle. b) Purge or pump-out of remaining reactant AC_4 to avoid gas-phase reactions. c) Gas-phase dosing of reactant BD_2, which will react to form AB_2—D + $(CD)_2$ as a leaving product. d) Purge or pump-out of remaining reactant BD to avoid gas-phase reactions. At the end of step d), surface is in the same condition as at the start of step a). An example of this is the deposition of HfO_2 using TDMAH (Hf—$(NEtMe)_4$) and water.

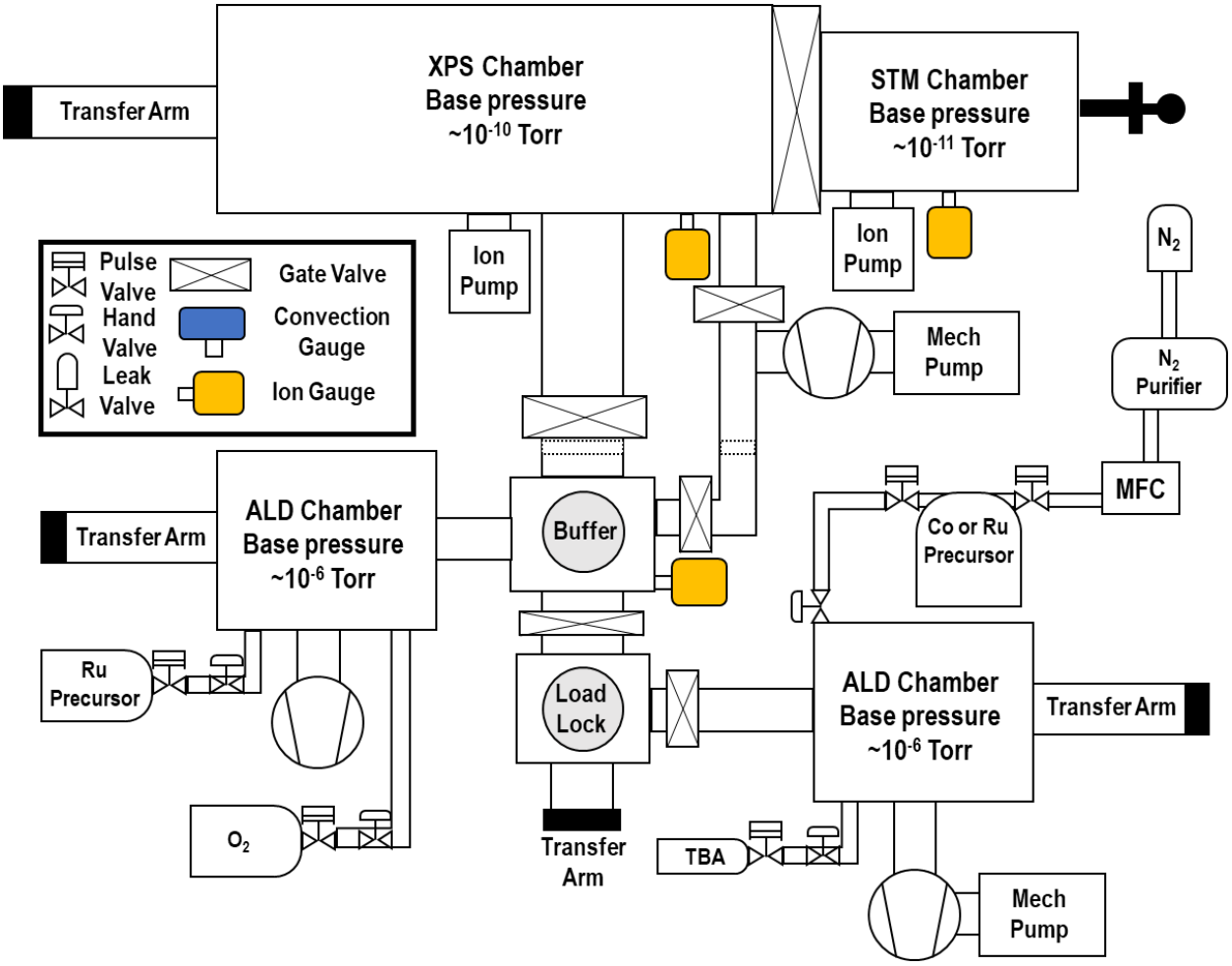

Figure 1.2: Schematic of ALD/XPS analysis system. Load-lock is used to prevent air exposure of the chambers and to allow transfer of sample under vacuum to avoid oxidation between precursor doses or deposition cycles.

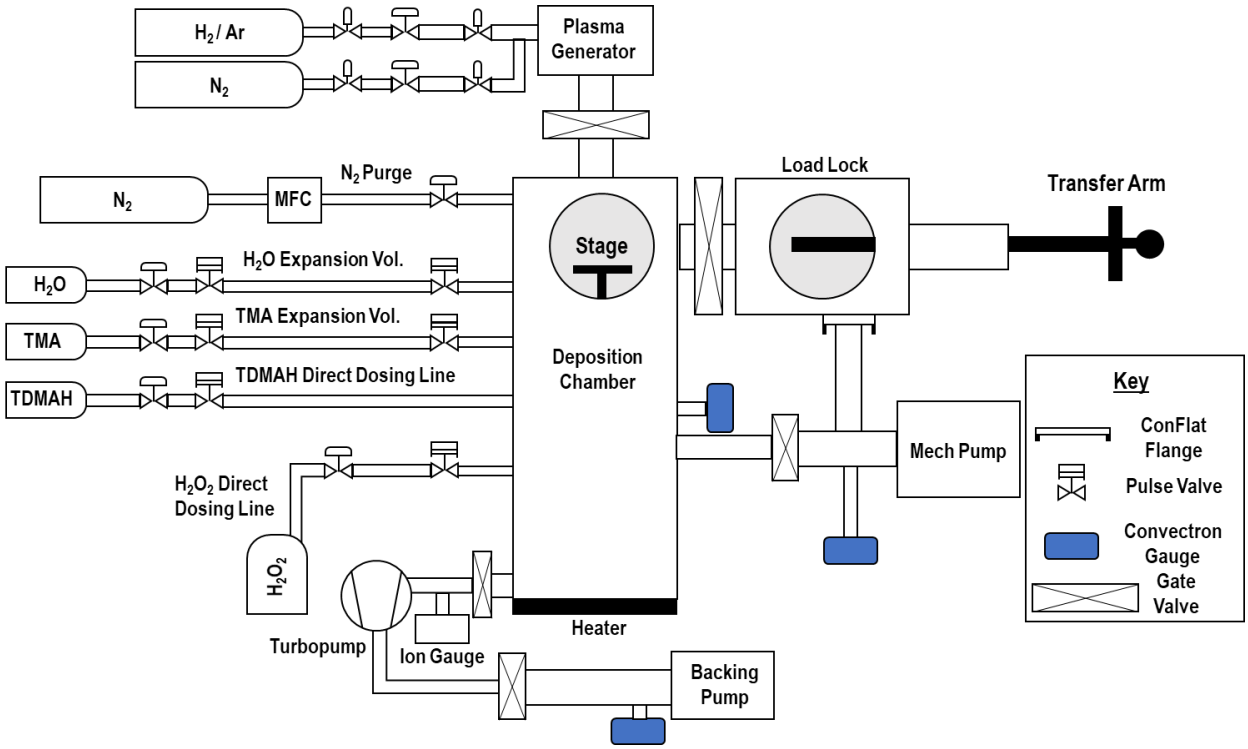

Figure 1.3: Schematic of gate oxide + RF plasma system. Schematic of the vacuum chamber used to deposit gate oxide by ALD and functionalize surface with a remote RF plasma generator.

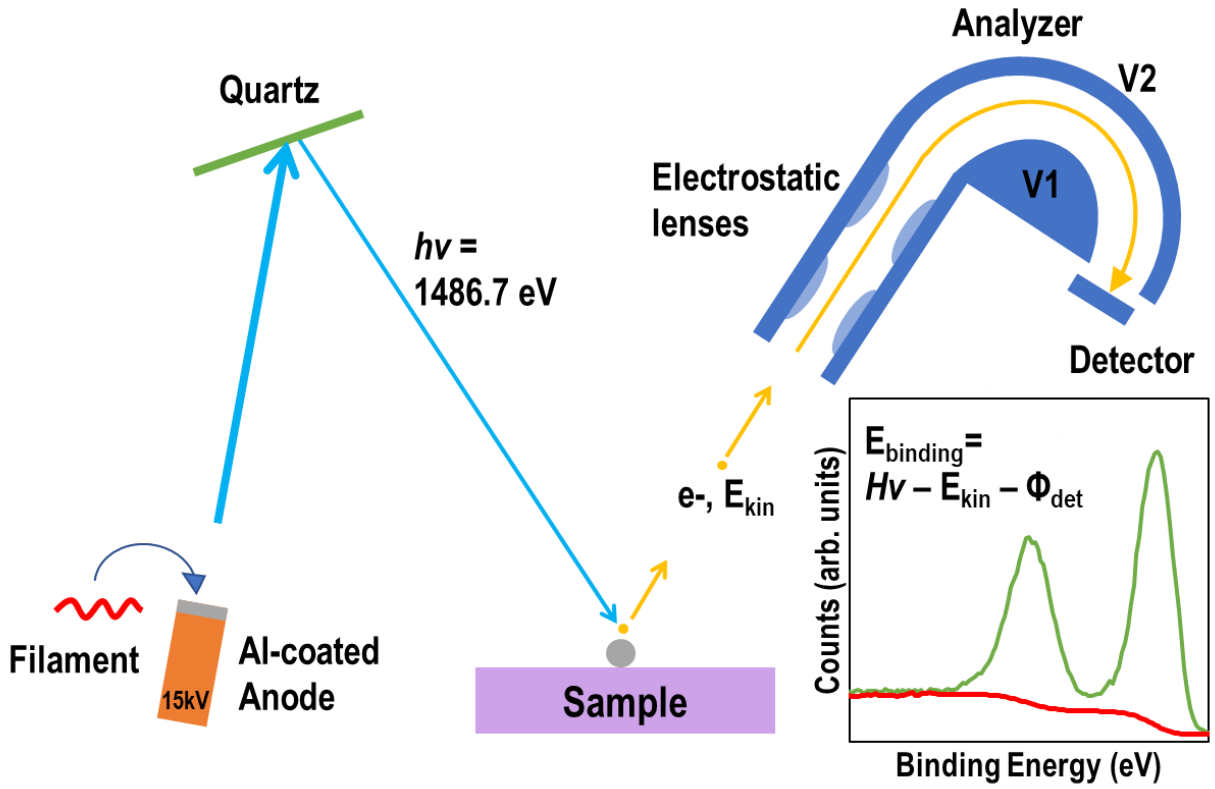

Figure 1.4: Principle of XPS. Al Kα X-rays are emitted from an anode and reflected off a quartz crystal monochromator with a precise energy, bombarding the surface and causing electrons to be ejected with a specific kinetic energy. The electron then passes through electrostatic lenses to a hemispherical detector tuned to only permit electrons of specific energies corresponding to the energy region of interest through to the detector. The difference between the X-ray energy and the kinetic energy of the electrons is the binding energy of the electron with the atom.

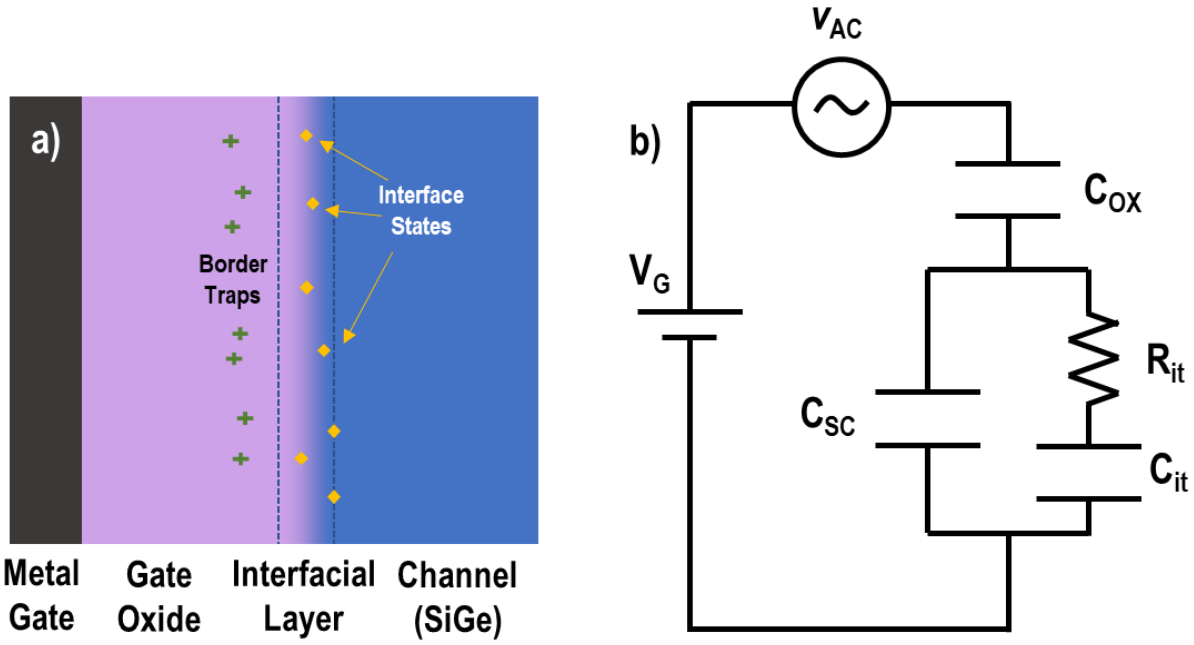

Figure 1.5: Electrical characterization of a MOSCAP. a) The metal-oxide-semiconductor structure, with interfacial layer and the presence of interfacial defects, along with border traps near the interface in the gate oxide. B) Equivalent circuit diagram of MOSCAP showing C_{ox} in series with a parallel circuit with C_{sc} and an interface state resistor and capacitor in series. The metal gate is biased against the semiconductor, with a small AC signal overlaid to measure the capacitance and conductance as a function of gate bias.

1.7 References

[1] R. Ritzenthaler, H. Mertens, V. Pena, G. Santoro, A. Chasin, K. Kenis, K. Devriendt, G. Mannaert, H. Dekkers, A. Dangol, Y. Lin, S. Sun, Z. Chen, M. Kim, J. Machillot, J. Mitard, N. Yoshida, N. Kim, D. Mocuta and N. Horiguchi, *Vertically stacked gate-all-around Si nanowire CMOS transistors with reduced vertical nanowires separation, new work function metal gate solutions, and DC/AC performance optimization,* in IEEE International Electron Devices Meeting (IEDM), San Francisco, 2018.

[2] O. Varela Pedreira, K. Croes, A. Lesniewska, C. Wu, M. H. van der Veen, J. de Messemaeker, K. Vandersmissen, N. Jourdan, L. G. Wen, C. Adelmann, B. Briggs, V. Vega Gonzalez, J. Bommels and Z. Tokei, *Reliability Study on Cobalt and Ruthenium as Alternative Metals for Advanced Interconnects,* in IEEE IRPS, 2017.

[3] C. W. Liu, M. Östling and J. B. Hannon, *New materials for post-Si computing,* MRS Bull., 2014. **39**(8): p. 658.

[4] D. Gall, *The search for the most conductive metal for narrow interconnect lines*, J. Appl. Phys., 2020. **127**: p. 050901.

[5] R. L. Puurunen, *Surface chemistry of atomic layer deposition: A case study for the trimethylaluminum/water process*, J. Appl. Phys., 2005. **97**: p. 121301.

[6] M. Ylilammi, *Monolayer thickness in atomic layer deposition,* Thin Solid Films, 1996. **279**: pp. 124-130.

[7] M. Edmonds, S. Wolf, E. Chagarov, T. Kent, J. H. Park, R. Holmes, D. Alvarez, R. Droopad and A. C. Kummel, *Self-limiting CVD of a passivating SiO_x control layer on InGaAs(001)-(2x4) with the prevention of III-V oxidation*, Surf. Sci., 2017. **660**: pp. 31-38.

[8] J. Elam, M. Schuisky, J. D. Ferguson and S. George, *Surface chemistry and film growth during TiN atomic layer deposition using TDMAT and NH_3,* Thin Solid Films, 2003. **436**: pp. 145-156.

[9] M. L. Green, M. E. Gross, L. E. Papa, K. J. Schnoes and D. Brasen, *Chemical Vapor Deposition of Ruthenium and Ruthenium Dioxide Films,* J. Elec. Soc., 1985. **132**: p. 2677.

[10] M. Leskelä and L. Niinistö, *Atomic layer epitaxy: chemical opportunities and challenges,* Thin Solid Films, 1993. **225**: pp. 130-135.

[11] G. N. Parsons and R. D. Clark, *Area-Selective Deposition: Fundamentals, Applications, and Future Outlook,* Chem. Mater., 2020. **32**: pp. 4920-4953.

[12] E. P. Gusev, E. Cartier, D. A. Buchanan, M. Gribelyuk, M. Copel, H. Okorn-Schmidt and C. D. Emic, *Ultrathin high-K metal oxides on silicon: processing, characterization and integration issues,* Microelectron. Eng., 2001. **59**: pp. 341-349.

[13] K. E. Elers, V. Saanila, P. J. Soininen, W. M. Li, J. T. Kostamo, S. Haukka, J. Juhanoja and W. F. Besling, *Diffusion barrier deposition on a copper surface by atomic layer deposition,* Chem. Vapor Dep., 2002. **8**: pp. 149-153.

[14] J. M. Hollander and W. L. Jolly, *X-ray photoelectron spectroscopy,* Acc. Chem. Res., 1970. **3**: pp. 193-200.

[15] K. Siegbahn, D. Hammond, H. Fellner-Feldegg and E. F. Barnett, *Electron spectroscopy with monochromatized X-rays,* Science, 1972. **176**: pp. 245-252.

[16] F. A. Stevie and C. L. Donley, *Introduction to x-ray photoelectron spectroscopy*, J. Vac. Sci. Technol. A, 2020. **38**: p. 063204.

[17] A. G. Shard, *Practical guides for x-ray photoelectron spectroscopy: Quantitative XPS,* J. Vac. Sci. Technol. A, 2020. **38**: p. 041201.

[18] A. S. Grove, E. H. Snow, B. E. Deal and C. T. Sah, *Simple physical model for the space-charge capacitance of metal-oxide-semiconductor structures,* J. Appl. Phys., 1964. **35**: p. 2458.

[19] L. M. Terman, *An investigation of surface states at a silicon/silicon oxide interface employing metal-oxide-silicon diodes,* Solid State Elec., 1962. **5**: pp. 285-299.

[20] E. H. Nicollian and A. Goetzberger, *The Si-SiO interface - electrical properties as determined by the metal-insulator-silicon conductance technique,* Bell Sys. Tech. Journal, 1967. **46**: pp. 1033-1055.

[21] Y. Yuan, B. Yu, P. C. McIntyre, P. M. Asbeck, M. J. W. Rodwell and Y. Taur, *A distributed bulk-oxide trap model for Al_2O_3 InGaAs MOS devices,* IEEE Trans. Electron Devices, 2012. **59**: p. 2100.

[22] B. J. Inkson, *Materials Characterization Using Nondestructive Evaluation (NDE) Methods,* Cambridge: Woodhead Publishing, 2016.

[23] T. E. Everhart and R. F. M. Thornley, *Wide-band detector for micro-microampere low-energy electron currents,* J. Sci. Instrum., 1960. **37**: pp. 246-248.

[24] D. C. Bell and A. J. Garratt-Reed, *Energy Dispersive X-ray Analysis in the Electron Microscope,* London: Garland Science, 2003.

[25] L. A. Giannuzi and F. A. Stevie, *A review of focused ion beam milling techniques for TEM specimen preparation*, Micron, 1999. **30**: pp. 197-204.

[26] J. M. Cowley, *Electron microdiffraction*, Adv. Electronic and Electron Phys., 1978. **46**: pp. 1-53.

[27] R. F. Egerton, *Electron energy-loss spectroscopy in the TEM*, Rep. Prog. Phys., 2008. **72**: pp. 1-25.

[28] P. E. Batson, *Simultaneous STEM imaging and electron energy-loss spectroscopy with atomic-column sensitivity*, Nature, 1993. **366**: pp. 727-728.

Chapter 2

$Al_2O_3/Si_{0.7}Ge_{0.3}(001)$ & $HfO_2/Si_{0.7}Ge_{0.3}(001)$ Interface Trap State Reduction via In-Situ N_2/H_2 RF Downstream Plasma Passivation

2.1 Abstract

A novel method for passivating the interface between $Si_{0.7}Ge_{0.3}$ using an in-situ downstream RF plasma consisting of a nitrogen-rich mixture of H_2 and N_2 gases at 250 °C prior to atomic layer deposition (ALD) of Al_2O_3 and HfO_2 was demonstrated. XPS spectra of the interface with Al_2O_3 indicated the presence of a nitride layer enriched in $SiON_x$ and depleted in Ge relative to the substrate. The electrical properties of this interface were characterized using I-V and variable frequency C-V measurements of MOS capacitors. The N_2/H_2 plasma passivation process produced a reduced density of interface trap states (D_{it}) and lower gate leakage compared with ex-situ HF clean and sulfur passivation for Al_2O_3 gate oxides. The lowered leakage current and D_{it} observed compared with HF(aq) or sulfur-passivated surfaces were consistent with enhanced oxide nucleation due to N_2/H_2 plasma passivation lowering carbon surface contamination and dangling bonds. TEM/EELS analysis of the interface was consistent with the presence of a thin interfacial nitride layer suppressing the formation of Ge-O bonds at the interface to form an SiO_x-rich interlayer (IL).

2.2 Introduction

To meet the demands of higher-performance, lower-power computing devices, the continued scaling of complementary metal-oxide-semiconductor (CMOS) devices requires the use of high-dielectric constant insulators (high-k dielectrics) and new channel materials. One promising class of channel materials are silicon-germanium (SiGe) alloys. The enhancement of hole mobility compared with Si due to splitting of the valence band heavy and light-hole band degeneracies makes tunable-Ge content SiGe channels desirable for use in p-type MOSFETs [1][2][3]. In comparison with other channel materials such as III-V compounds, SiGe alloys can be introduced into existing CMOS process flows, and growth of epitaxial SiGe layers by low-pressure chemical vapor deposition (LPCVD) or molecular beam epitaxy (MBE) has been well-studied and is in commercial use for heterojunction bipolar transistors, [4][5] as well as for stressor materials in strained-Si channel MOSFETs [6].

High-k dielectrics containing Al and/or Hf have been integrated successfully with commercial Si-channel CMOS processes since the 45 nm node [7][8]. On Si, the density of interfacial defects is low, and attempts at improving the quality of the gate oxide have focused on the suppression of SiO_2 formation at the interface using a Ti- or La- doped HfO_2 dielectric to ensure an amorphous microstructure and formation of Hf-silicate at the interface to improve capacitance [9][10]. Conversely, formation of low defect interfaces between high-k oxides and higher-mobility channel materials such as GaAs or InGaAs has been challenged by high densities of defects with HfO_2, Al_2O_3, and TiO_2 gate oxides, or mixed metal oxides and silicates [11]. Chemical passivation of these surface defects prior to high-k deposition by ALD has been achieved on III-V substrates by employing thin Al_2O_3 layers to suppress As-O and Ga-O formation [12], as well as the use of dimethylaluminum hydride and O_2 in an MOCVD process to remove native

oxides on InGaAs prior to deposition of HfTiO dielectric [13]. Suppression of an interfacial layer on the high-k/GaAs system has been achieved through nitrogen reactive sputtering of HfTi to form HfTiON [14]. In-situ plasma nitridation has also been reported on InGaAs using alternating pulses of N_2 plasma and trimethylaluminum prior to HfO_2 deposition [15]. Two-dimensional materials such as graphene offer the potential for zero interfacial layer thickness, but the chemically-inert surface of graphene has limited nucleation density of oxide layers. Nucleation of Al_2O_3 on graphene has been achieved by pre-pulsing H_2O prior to ALD, with physisorbed H_2O acting as a seed for subsequent reaction with trimethylaluminum (TMA) [16][17].

Passivation of interfacial defects on SiGe-channel CMOS devices requires a different approach than on III-V semiconductor channel devices. In-situ nitridation has been extensively studied on Ge MOS devices in suppressing the formation of thermally-unstable GeO_2 and diffusion of Ge into the high-k dielectric by terminating the surface with Ge nitrides and oxynitrides, resulting in high thermal stability and low interface state densities (D_{it}) [18][19][20]. However, the relative stability of Si-N bonds compared with Ge-N bonds has resulted in higher interface state defect densities for SiGe alloys. Low D_{it} values for SiGe have been reported by using post-deposition plasma nitridation by N_2 [21], passivation of SiGe by aqueous sulfur treatment [22], and NH_3 plasma nitridation [23]. However, post-deposition nitridation limits equivalent oxide thickness scaling and control over initial nucleation and growth, while aqueous sulfur passivation presents reliability concerns while requiring ex-situ treatment. NH_3 plasma nitridation, while successfully employed for plasma-enhanced ALD processes of metal nitrides, results in a fixed ratio of N and H species in plasma, which may result in suboptimal nitridation conditions for surface passivation [24].

This work demonstrates the use of a tunable mixture of H_2 and N_2 species in an RF downstream plasma to passivate the surface of SiGe prior to deposition of gate oxide. Capacitance-voltage and current-voltage measurements were used to determine the effectiveness of the N_2/H_2 RF plasma process on the interface state density and leakage current, while X-ray photoelectron spectroscopy (XPS), transmission electron microscopy (TEM), and electron energy-loss spectroscopy (EELS) were employed to investigate the chemical environment of the SiGe/high-k interface, as well as the interfacial layer thickness and composition using Al_2O_3 and HfO_2 as gate dielectrics.

2.3 Experimental

In this study, to demonstrate the effectiveness of the N_2/H_2 downstream plasma passivation method, metal-oxide-semiconductor capacitors (MOSCAPs) were fabricated with Al_2O_3 and HfO_2 dielectrics on a $Si_{0.7}Ge_{0.3}$ channel with (001) orientation. The SiGe channel layer consisted of a 9-nm-thick p-type $Si_{0.7}Ge_{0.3}$(001) layer with $1x10^{18}$ cm^{-3} dopant density epitaxially grown on p-type Si(001) by molecular beam epitaxy (Applied Materials, Inc.). Prior to dielectric deposition, each sample underwent an organic clean via a rinse of acetone, methanol, and DI H_2O, followed by native oxide removal via 2.5 cycles of 1 minute immersion in 2% HF(aq) and 1 minute immersion in DI H_2O, following the method of Oshima, et al., on high-Ge content substrates [18]. To benchmark N_2/H_2 plasma passivation in comparison with other methods, three methods were compared – HF(aq) only clean in which no further preparation prior to dielectric deposition was performed, ex-situ sulfur passivation in which the sample was immersed in a 25% solution of $(NH_4)_2S$ for 15 minutes, and in-situ N_2/H_2 plasma pre-deposition. After ex-situ sample preparation, samples were transferred to the ALD chamber within 2 minutes to minimize air exposure.

Fig. 2.1 depicts the chamber used to perform dielectric deposition and in-situ plasma passivation. The main deposition chamber is pumped to a base pressure of 2 x 10^{-2} Torr via rotary vane mechanical pump and is connected to a load lock for sample transfer. Above the chamber, an RF downstream plasma source (PIE Scientific, Inc.) was mounted to generate the N_2/H_2 plasma mixture. A sapphire plasma tube was employed to resist attack from atomic H generated in the plasma [25]. An ultra-high purity mixture of N_2 and 5% H_2 in Ar (Praxair) at 1 Torr pressure was employed for the plasma source with an N-to-H ratio of 20:1, which was maintained at an RF power of 20 W. Plasma processing was performed after the sample was pre-heated for 5 minutes at 250 °C.

For ALD of the dielectric layer, trimethylaluminum (TMA, Strem Chemicals, Inc.), tetrakis(dimethylamino) hafnium (TDMAH, Strem Chemicals, Inc.), and 18 MΩ·cm DI H_2O were mounted to the chamber for Al_2O_3 and HfO_2 deposition. TMA and H_2O sources were kept at 25 °C, while the TDMAH source was heated to 70 °C. All chamber walls, precursor dosing lines, and pump lines were held at a temperature of 130 °C to ensure precursors would not condense on the wall prior to reaching the sample and to minimize powder formation. To maintain the deposition temperature at 250 °C, a UHV pedestal heater (Heatwave Labs, Inc.) was utilized, and samples were pre-heated for 5 minutes prior to in-situ processing. Pneumatic valves controlled via custom LabVIEW program were employed to control dosing times of precursors. Expansion volume dosing was used for TMA and H_2O dosing due to their high vapor pressures. During Al_2O_3 cycles, TMA was dosed into the expansion volume for 600 ms, followed by a 5s dose to the chamber and 1s inert purge. Subsequently, water was dosed into the expansion volume for 700 ms, followed by a 5s dose and 1s inert purge. For HfO_2 cycles, TDMAH was dosed directly to the chamber for 250 ms, followed by a 25 s inert purge, and the water half-cycle was dosed to the expansion volume

for 600 ms, dosed to the chamber for 5 s and inert purge for 10 s. The TDMAH and H_2O purge times were increased to avoid the possibility of gas-phase reactions inducing CVD, as the lower vapor pressure of the TDMAH precursor resulted in incomplete gas evacuation before the next half-cycle without extension. A constant 100 mTorr UHP N_2 (Praxair) purge was run during deposition to prevent mixing of precursors in the reaction chamber.

To complete the MOSCAP structure, 30 nm of Ni was thermally evaporated to form 150 μm diameter circular gates, and a backside 100 nm Al contact was deposited via DC sputtering. After fabrication, MOSCAPs were annealed in forming gas (5% H_2, 95% N_2) at 300 °C for 15 minutes, 330 °C for 10 minutes, and 350 °C for 5 minutes, following the method described by Kavrik, et al [26]. Capacitance-, conductance- and current-voltage (C-V/G-V/I-V) characteristics of the MOSCAPs were performed using an Agilent B1500 semiconductor analyzer with an AC modulation amplitude of 30 mV between a gate bias of -2 and +2 V at frequencies from 2 kHz to 1 MHz. Using the C-V and G-V relationships measured, interface state densities (D_{it}) were measured using both the conductance method [27] and the full interface state distribution and density of bulk-oxide trap states was calculated using the method of Chen and Yuan [28] [29]. The gate leakage current was measured between -2 and +2 V bias.

To investigate the chemical environment at the high-k/SiGe interface, 5 cycles of Al_2O_3 were deposited on SiGe samples after organic and HF preclean, and with or without N_2/H_2 plasma passivation. These samples were removed and rapidly transferred (with a maximum of 2 minutes of air exposure) to a surface analysis tool consisting of load lock and UHV chamber at a base pressure of $1x10^{-10}$ Torr with a monochromatic XM1000 MkII/SPHERA XPS system (Omicron Nanotechnology GmbH) for collection of XPS spectra. The source used was a monochromatic Al kα source at 1486.7 eV with an analyzer pass energy of 50 eV and linewidth of 0.1 eV, and XPS

spectra were collected at 30° with respect to parallel to the sample. XPS analysis was performed using CASA XPS 2.3 software, with raw peak areas corrected via Schofield photoionization cross-sectional relative sensitivity factors. Elemental analysis of the high-k/SiGe interface was performed using TEM/EELS at electron acceleration of 80 keV to minimize beam damage to the Al_2O_3 layer. Principal component analysis was used to de-noise EELS spectra [30].

2.4. Results & Discussion

2.4.1. Al_2O_3/SiGe

To compare the effects of N_2/H_2 plasma passivation with HF(aq) only clean and sulfur passivation, 40 ALD cycles of Al_2O_3 were deposited at 250 °C and MOSCAPs were fabricated. Fig. 2.2 displays the C-V characteristics of three of the devices, with the HF(aq) only cleaned sample exhibiting a larger low-frequency "bump" between 0 and 0.5 V gate bias than either the N_2/H_2 plasma passivated surface or the sulfur-passivated surface. By the conductance model [27], interface state densities were found to be 3.6×10^{12}, 8.9×10^{11}, and 7.2×10^{11} $cm^{-2}eV^{-1}$ at midgap for HF only, HF + ex-situ sulfur, and HF + in-situ N_2/H_2 plasma passivation, respectively. The in-situ N_2/H_2 plasma passivation D_{it} is comparable to the peak value obtained by post-deposition plasma nitridation and demonstrates a factor of 3 improvement in interface state density over in-situ ammonia plasma nitridation [21] [23]. Oxide capacitances derived from the full interface state model were 1.02, 1.13, and 1.10 $\mu F \cdot cm^{-2}$, respectively [28]. Equivalent oxide thickness (EOT) for the three Al_2O_3 devices were 3.4, 3.1, and 3.1 nm. The sulfur-cleaned and N_2/H_2 plasma-cleaned samples exhibited similar oxide capacitances, illustrating that the N_2/H_2 plasma passivation technique is effective in preventing unwanted interfacial oxide growth during Al_2O_3 ALD.

Fig. 2.3 shows the leakage current density and interface state density as a function of energy across the bandgap for the three devices as derived by the Chen full interface state model. Integrated interface state densities across the bandgap were 1.5 x 10^{12} cm^{-2} for the HF(aq) only sample, 3.4 x 10^{11} cm^{-2} for the HF(aq) + ex-situ sulfur-passivated sample, and 2.4 x 10^{11} cm^{-2} for the HF(aq) + in-situ N_2/H_2 plasma-passivated sample. The peak of the interface state density is located at 0.2 to 0.5 eV above the valence band edge for all three devices. The energy range of this interface state density peak corresponds with that of the peak interface state density reported for the Si/SiO_2 interface, which was found to be due to the formation of dangling bonds at Si P_b centers acting as amphoteric defects [31] [32]. By comparison, interface states at the Ge/GeO_2 interface have been found to act as acceptors, and observed interface state densities are consistent with GeO_x-induced defects in the oxide interfacial layer [33] [34]. This result is consistent with the formation of Si-O-Al bonds at the interface which are effectively passivated by hydrogen after forming gas anneal. Border trap densities (N_{bt}) were calculated with the model of Yuan, with N_{bt} values for HF only, HF + sulfur, and HF + plasma passivated devices being 3.9 x 10^{19} $cm^{-3}eV^{-1}$, 1.8 x 10^{19} $cm^{-3}eV^{-1}$, and 1.8 x 10^{19} $cm^{-3}eV^{-1}$, respectively [29]. Care in interpreting these values should be taken, as the model does not consider substrate series-resistance or correct for the effect of gate leakage current density [29].

The effect of the forming gas anneal on the plasma-cleaned devices is illustrated in Fig. 2.4. The temperatures and times used for the forming gas anneal were chosen after an optimization of anneal conditions, from which it was found that a ramped temperature anneal from 300 °C to 350 °C for 30 minutes improved the interface quality over a constant temperature anneal, following the method of Kavrik, et al [26]. This is reflected in the reduction in D_{it} from 3.6 x 10^{12} $cm^{-2}eV^{-1}$ for the HF(aq)-only sample before anneal, to 1.1 x 10^{12} $cm^{-2}eV^{-1}$ for the 15 minute 300 °C annealed

sample and 7.2 x 10^{12} $cm^{-2}eV^{-1}$ for the 30 minute ramped forming gas anneal. It is hypothesized that the interfacial defects as reflected in the conductance-voltage characteristics have a distribution of activation energies and preexponential factors; ramping the temperature of anneal over time, these defects can be more effectively passivated while minimizing the total thermal budget extended, limiting Ge diffusion through the interface during anneal.

To evaluate the chemical structure of the interface between Al_2O_3 and SiGe, 5 cycles of Al_2O_3 were deposited on SiGe at 250 °C. Prior to deposition, samples were cleaned with HF(aq) only or with HF(aq) + in-situ N_2/H_2 RF plasma passivation to compare the effectiveness of the passivation techniques. XPS spectra for a) Si 2p, b) Ge 3d, c) N 1s, and d) O 1s are shown in Fig. 2.5, and the integrated XPS spectrum area of each peak and the $SiON_x$ and $GeON_x$ peaks are shown in Fig. 2.5(e). The composition of the nitride peaks corresponding to SiN_x and GeN_x components are observed at 102.1 eV and 31.8 eV, respectively, for the N_2/H_2 plasma-passivated surface. The N 1s peak is absent from the HF only cleaned sample, reflecting the lack of nitrogen treatment, while on the N_2/H_2 plasma cleaned sample, the peak is centered at 398.0 eV, consistent with values reported previously for $SiON_x$ [35] [36].

The ratio of the nitride signal to the elemental XPS peak is approximately 39% for the Si peak and 17% for the Ge peak on the plasma-passivated surface, suggesting preferential formation of Si-N bonds over Ge-N bonds. This is consistent with previous XPS studies of preferential formation of Si_3N_4 compared with Ge_3N_4 and is consistent with the higher heat of formation for Si_3N_4 at -744 kJ/mol compared with -63 kJ/mol for Ge_3N_4. Due to the lower Ge_3N_4 heat of formation, only a small component of stoichiometric Ge oxynitride within the $SiON_x$ layer is observed [37]. The resulting $SiON_x$-rich layer is more thermally stable and more likely to inhibit H_2O and Ge diffusion through the interface during ALD oxide growth, improving interface quality

compared with HF(aq) only cleaned interfaces [36]. Furthermore, a small GeO_x shoulder on the Ge peak located at 30.5 eV is observed on the HF(aq) only cleaned sample, while the N_2/H_2 plasma passivated sample lacks this feature. This is also consistent with the suppression of Ge-O bonding in the nitrided sample. The intensity of the Si and Ge peaks is suppressed for the N_2/H_2 plasma-passivated surface compared with the surface cleaned only by HF(aq) prior to deposition, suggesting a thicker layer of Al_2O_3. This is consistent with the N_2/H_2 plasma passivation enhancing initial nucleation of the gate dielectric, which is reflected in the plasma-passivated devices exhibiting lower leakage currents.

The formation of the nitride interfacial layer is hypothesized to be due to the reaction of NH_x- radicals at the surface of the SiGe channel. A plasma power of 20 W is sufficient to ionize N_2 and H_2, but since the pressure in the chamber exceeds 1 mTorr, ion recombination of these species occurs before the plasma gases can reach the surface of the sample. Instead, it is expected that atomic N formed in the plasma reacts with Si and Ge to form SiN_x and GeN_x, while the NH_x-radicals react with surface defect sites and C contamination on the surface. Previous studies of plasma nitridation on SiGe with ammonia have hypothesized the nitridation species to be atomic N, while residual carbon defects on the surface are cleaned up through reaction with NH_x radicals [21] [23]. A higher N-to-H ratio is then expected to promote atomic N in the plasma gases, enhancing surface nitridation.

To investigate the thickness of the interfacial layer and the chemical structure of the interface in a full MOSCAP device after forming gas anneal, high-resolution transmission electron microscopy (HRTEM) was used to image a cross section of the interface. Additionally, electron energy-loss spectroscopy (EELS) was employed to capture the chemical structure of the interface on the HF(aq) only, sulfur-passivated, and N_2/H_2 plasma passivated devices. Fig. 2.6 shows

HRTEM and EELS spectra across the gate stack on the HF(aq) only, sulfur-passivated, and N_2/H_2 passivated devices. From inspection of the HRTEM and EELS data, the interfacial layer thickness of the plasma-cleaned device was 1.5 nm, compared with 1.3 nm for the sulfur cleaned device and 1.6 nm for the HF(aq) only cleaned device. However, the nonuniformity of the interfacial thickness suggests no correlation of interfacial thickness with improved interfacial quality. Fig. 2.6f contains the EELS data for the sample passivated by N_2/H_2 plasma, which illustrates a nitride layer 1.5 nm thick at the interface. At the center of the N peak, the ratio of Ge relative to Si is 0.14, which is consistent with an interlayer mostly consisting of $SiON_x$ with low Ge content relative to the HF(aq) only cleaned surface. This suggests that the nitride formed during plasma-passivation is effective in suppressing the formation of Ge-O bonds by preventing the diffusion of Ge through to the gate oxide during growth.

2.4.2. HfO_2/SiGe

To determine if the N_2/H_2 plasma passivation is effective in passivating the interface between SiGe and a higher-dielectric constant insulator, MOSCAPs with 40 and 50 ALD cycles of HfO_2 were fabricated. Fig. 2.7 illustrates the C-V characteristics of five of these devices, with the HF(aq) only clean exhibiting a larger low-frequency "bump" between 0 and 0.5 V gate bias than the N_2/H_2 plasma passivated surface. Unlike the Al_2O_3 MOSCAPs, sulfur passivation of the HfO_2 MOSCAPs was unsuccessful in yielding devices with lower leakage and defect densities than the HF(aq) only device, and 40 cycle MOSCAPs prepared by HF(aq) only clean had a leakage current density too large to accurately extract the interface state density profile from the measured C-V data. Furthermore, while interface state analysis was performed for the 40 cycle sulfur-passivated device, the high leakage current density may call into question the validity of the

extracted profile. It is noted that the poor performance of the sulfur passivated HfO_2 MOSCAPs may be deposition system and precursor specific. By the conductance model, interface state densities for the 40 cycle HfO_2 devices were found to be 6.1 x 10^{12}, 4.9 x 10^{12}, and 3.8 x 10^{12} $cm^{-2}eV^{-1}$ at midgap for the HF(aq) only, HF(aq) + ex-situ sulfur, and HF(aq) + in-situ N_2/H_2 plasma passivation, respectively. For the 50 cycle devices, the HF(aq) only cleaned device had a D_{it} of 4.8 x 10^{12} $cm^{-2}eV^{-1}$, while the HF(aq) + N_2/H_2 plasma-passivated device had a D_{it} of 2.9 x 10^{12} $cm^{-2}eV^{-1}$. Oxide capacitances derived from the full interface state model were 1.90, 1.85, and 2.48 $\mu F \cdot cm^{-2}$ for the 40 cycle devices, and 1.95 and 2.14 $\mu F \cdot cm^{-2}$ for the 50 cycle devices, respectively, demonstrating that an improvement in the interface state density through the N_2/H_2 plasma passivation technique can also be extended to higher dielectric constant materials than Al_2O_3, yielding a lower equivalent oxide thickness.

Fig. 2.8 details the interface state density across the bandgap and leakage current characteristics for 40 and 50 cycle HfO_2 MOSCAPs. Comparing the leakage current at -2 V bias for 40 cycle HfO_2 MOSCAPs, a 10000x reduction in leakage is observed for the N_2/H_2 plasma passivated device after forming gas anneal, compared with the HF(aq) only cleaned device. This is indicative of a significant improvement in oxide nucleation and growth on the nitrided interfacial layer. The full interface state model developed by Chen et al. was applied to HfO_2 MOSCAPs with lower leakage to characterize the integrated interface state density across the bandgap [28]. The 50 cycle HF(aq) only sample had an integrated interface state density across the bandgap of 1.6 x 10^{12} cm^{-2}, while the 50 cycle N_2/H_2 plasma passivated sample had an integrated interface state density of 8.0 x 10^{11} cm^{-2}, a 2x improvement. The 40 cycle HF(aq) + ex-situ sulfur-passivated sample had an integrated interface state density of 1.2 x 10^{12} cm^{-2}, and the 40 cycle N_2/H_2 plasma-passivated sample 1.1 x 10^{12} cm^{-2}. Integrated interface state density is significantly higher than

that of Al_2O_3 MOSCAPs, which is consistent with poor diffusion barrier properties of deposited HfO_2 compared with Al_2O_3. It is hypothesized that the higher integrated D_{it} for the 40 cycle vs 50 cycle ALD processes are consistent with HfO_2 being a poorer diffusion barrier for the ex-situ transfer for metal gate deposition than Al_2O_3. Finally, border-trap densities (N_{bt}) were calculated for the non-leaky devices, as the 40 cycle HF only and 50 cycle HF + sulfur passivated devices were too leaky for a meaningful model fit. The 50 cycle HF only device had an N_{bt} of 3.3 x 10^{19} $cm^{-3}eV^{-1}$, while the 40 cycle HF + sulfur passivated device had an N_{bt} of 6.0 x 10^{19} $cm^{-3}eV^{-1}$. Conversely, the 40 and 50 cycle HF + plasma-passivated devices had N_{bt} values of 1.3 x 10^{19} $cm^{-3}eV^{-1}$ and 1.1 x 10^{19} $cm^{-3}eV^{-1}$. Under the border trap model developed by Yuan et al., a single border trap state is assumed and series resistance is neglected, yet these results are still consistent with effective oxide nucleation at the plasma-passivated interface decreasing tunneling into oxide trap states close to the interface [29].

TEM and EELS were used to characterize the thickness and chemical composition of the interfacial layer for the HfO_2 MOSCAPs. Fig. 2.9 shows the HRTEM images and EELS data for the HF(aq) only, sulfur, and N_2/H_2 plasma passivated devices. The interfacial layer thickness of the plasma-cleaned device was 1.3 nm compared with 1.2 nm for the sulfur cleaned device, and 1.4 nm for the HF(aq) only device. Similar to the Al_2O_3 MOSCAPs, the ratio of Ge to Si in the interface is observed to decrease relative to the SiGe layer for the N_2/H_2 plasma passivated devices compared with the HF(aq) only devices, with the ratio of Ge to Si at the middle of the interfacial layer being 0.16 for the plasma-passivated device compared with 0.35 for the HF(aq) only device and 0.26 for the sulfur-passivated device. Additionally, the Ge content falls off 0.4 nm than the Si content in the HF(aq) only device, suggesting that the HF(aq) treated surface causes the interlayer on HfO_2 to be a poorer diffusion barrier for Ge compared with plasma and sulfur passivation. The

maximum of the N peak observed in Fig. 2.9f corresponds to a region with lower Ge content relative to Si and significant oxygen, consistent with an interlayer consisting of mostly SiO_yN_x.

2.5 Conclusion

An in-situ, tunable mixture of N and H in an RF downstream plasma has been demonstrated to effectively passivate the surface of SiGe prior to deposition of high-k gate dielectrics Al_2O_3 and HfO_2. As opposed to ex-situ aqueous sulfur-containing treatment or post-deposition plasma nitridation, the pre-deposition in-situ nitridation by N_2/H_2-containing plasma reduces interfacial trap state density by 80% compared with HF(aq) only treatment, and by 20% compared with aqueous sulfur passivation. Investigation of the interfacial composition carried out by XPS illustrates that the formation of an SiO_xN_y interfacial layer both decreases D_{it} and lowers leakage currents, which is consistent with an enhancement in gate oxide nucleation. TEM/EELS analysis illustrates that this interfacial nitride layer is effective in suppressing the presence of Ge-O bonds in the interface.

2.6 Acknowledgments

This work was performed in part at the San Diego Nanotechnology Infrastructure (SDNI) of UCSD, a member of the National Nanotechnology Coordinated Infrastructure, which is supported by the National Science Foundation (Grant ECCS-1542148). Wafers were supplied by Applied Materials, Inc. This work was partially supported by gifts from Applied Materials, Inc. and Taiwan Semiconductor Manufacturing Company, Ltd.

Chapter 2, in full, is a reprint of the material as it appears in Applied Surface Science. M. Breeden, S. Wolf, S. Ueda, Z. Fang, C.Y. Chang, K. Tang, P. McIntyre, A. C. Kummel. *$Al_2O_3/Si_{0.7}Ge_{0.3}$(001) & $HfO_2/Si_{0.7}Ge_{0.3}$(001) Interface Trap State Reduction via In-Situ N_2/H_2 RF Downstream Plasma Passivation.* Appl. Surf. Sci, 2019. **478**: p. 1065-1073. The dissertation author was the primary investigator and author of this paper.

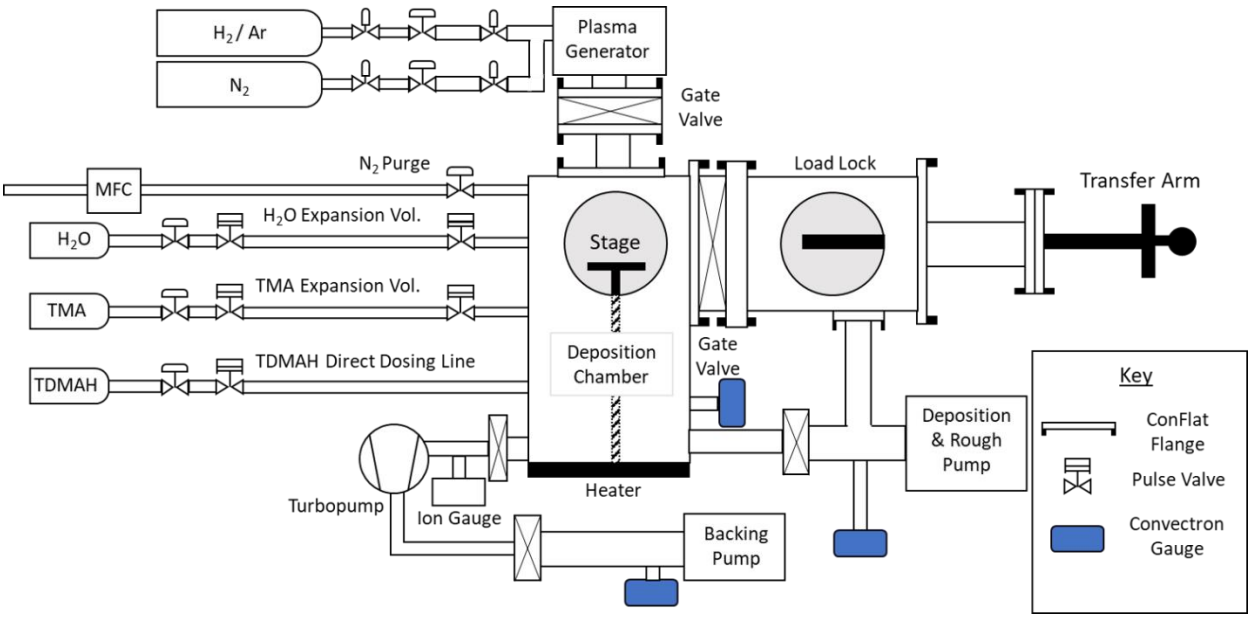

Figure 2.1: Schematic of chamber used for gate oxide ALD. Showing the load-locked deposition chamber with attached RF downstream plasma source, heated sample stage, and precursor dosing lines.

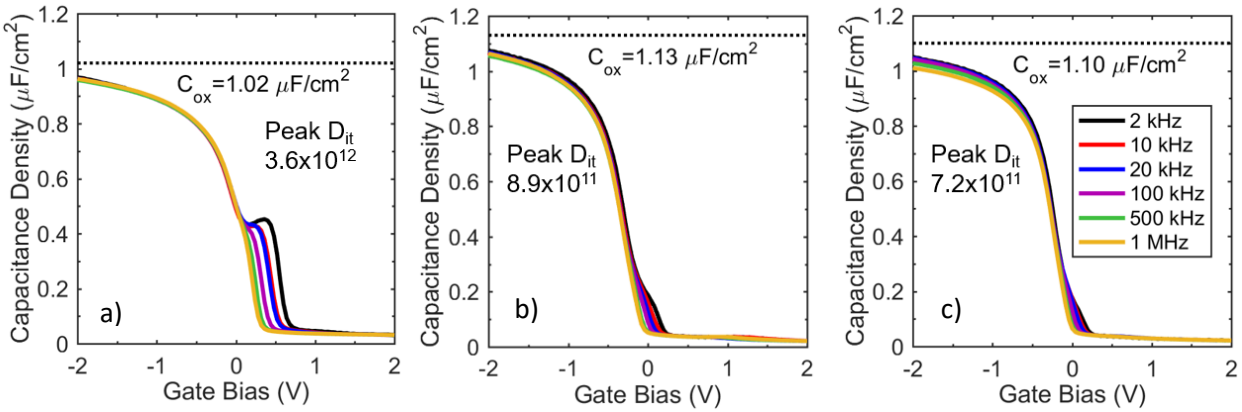

Figure 2.2: Effect of surface treatment before Al_2O_3 ALD. 2 kHz – 1 MHz C-V characteristics of 40 cycle Ni/Al_2O_3/$Si_{0.7}Ge_{0.3}$ MOSCAPs after forming gas anneal. (a) HF(aq) pre-clean only – 5.9 nm oxide + interlayer thickness (b) HF(aq) clean + ex-situ $(NH_4)_2S$ treatment – 6.1 nm oxide + interlayer thickness (c) HF(aq) clean + N_2/H_2 plasma treatment – 6.0 nm oxide + interlayer thickness. C_{ox} values were estimated using quasi-static C-V simulations.

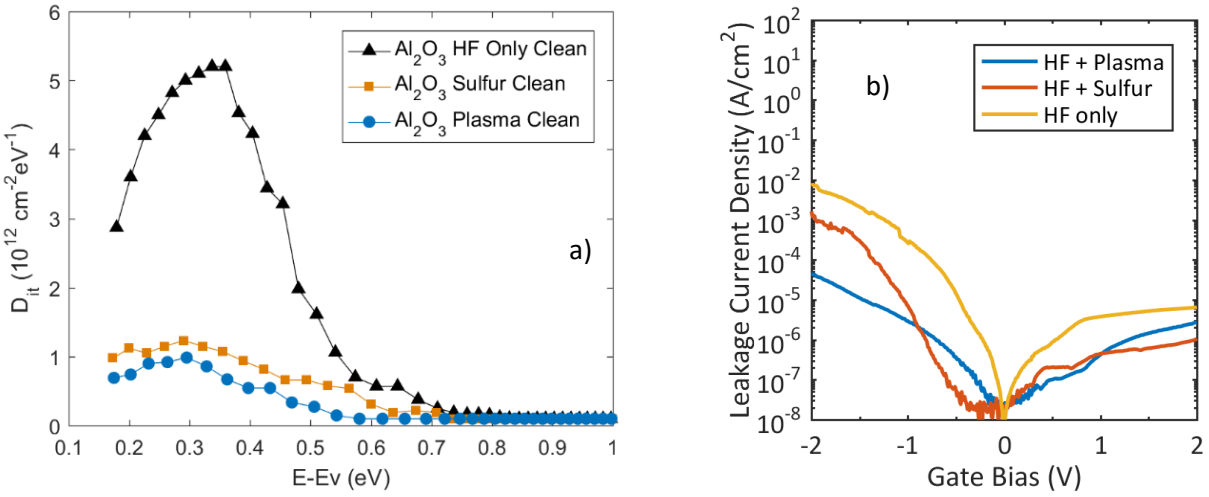

Figure 2.3: Effect of surface treatment before Al_2O_3 ALD on interface state density and I-V characteristics. (a) Full interface state model [29] and (b) I-V characteristics of 40 cycle $Ni/Al_2O_3/Si_{0.7}Ge_{0.3}$ MOSCAPs after forming gas anneal.

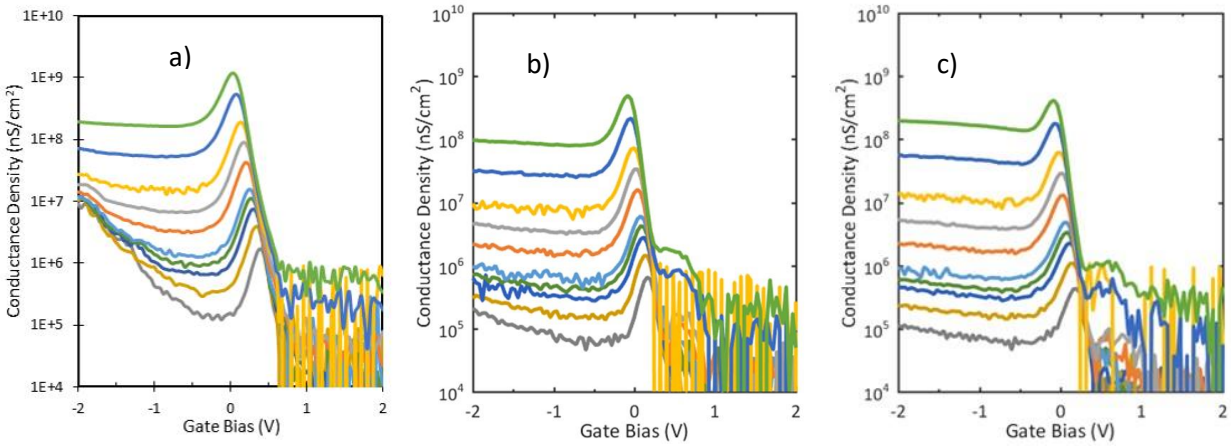

Figure 2.4: Effect of surface treatment before Al_2O_3 ALD on G-V characteristics. Conductance-voltage characteristics of Ni/Al_2O_3/$Si_{0.7}Ge_{0.3}$ MOSCAPs with 40 cycles of Al_2O_3 ALD after N_2/H_2 plasma passivation (a) before ramped forming gas anneal, (b) after 15 minute 300 °C forming gas anneal, and (c) after 30 minute ramped forming gas anneal from 300-330-350 °C.

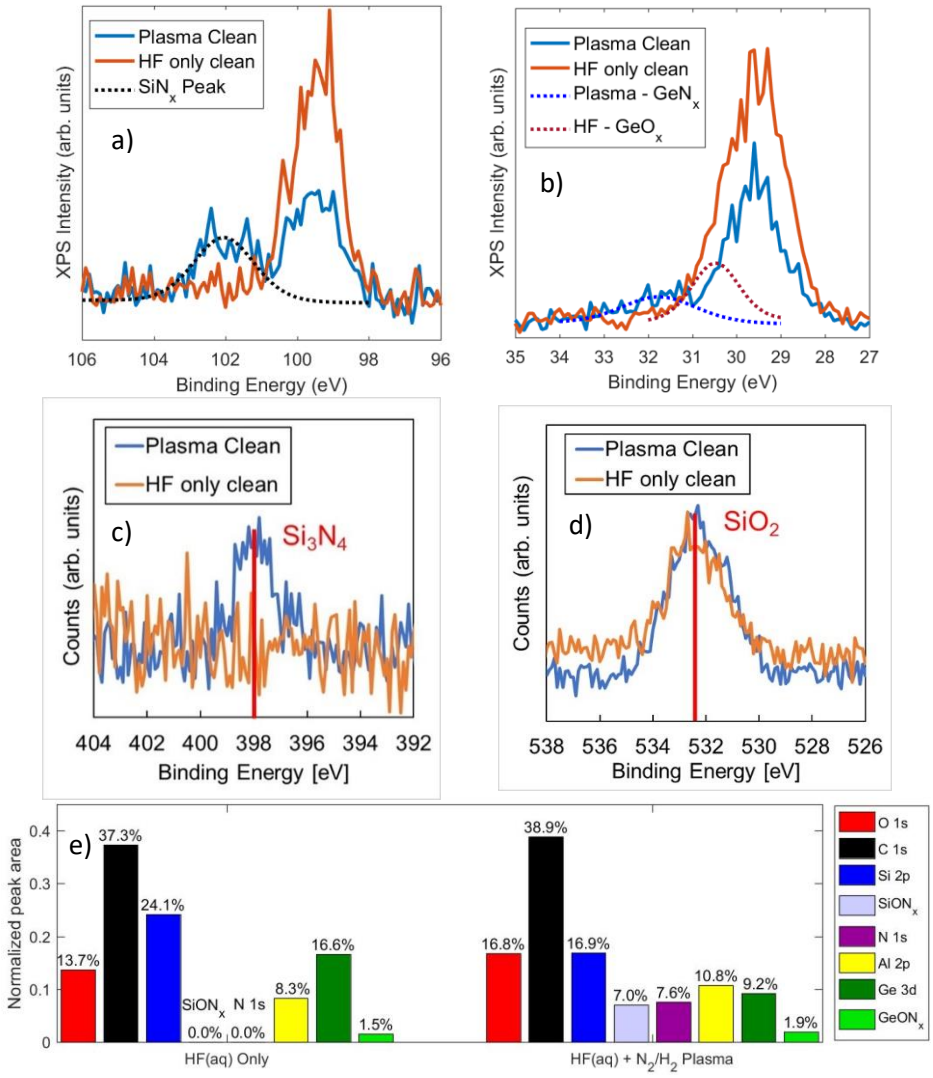

Figure 2.5: XPS study of Si and Ge chemical states before and after plasma clean. XPS spectra for (a) Si 2p peak (b) Ge 3d peak (c) N 1s peak (d) and O 1s peak for 5 cycles of $Al_2O_3/Si_{0.7}Ge_{0.3}$. (e) Normalized XPS integrated signal values for HF(aq) only and HF(aq) + N_2/H_2 plasma passivated SiGe.

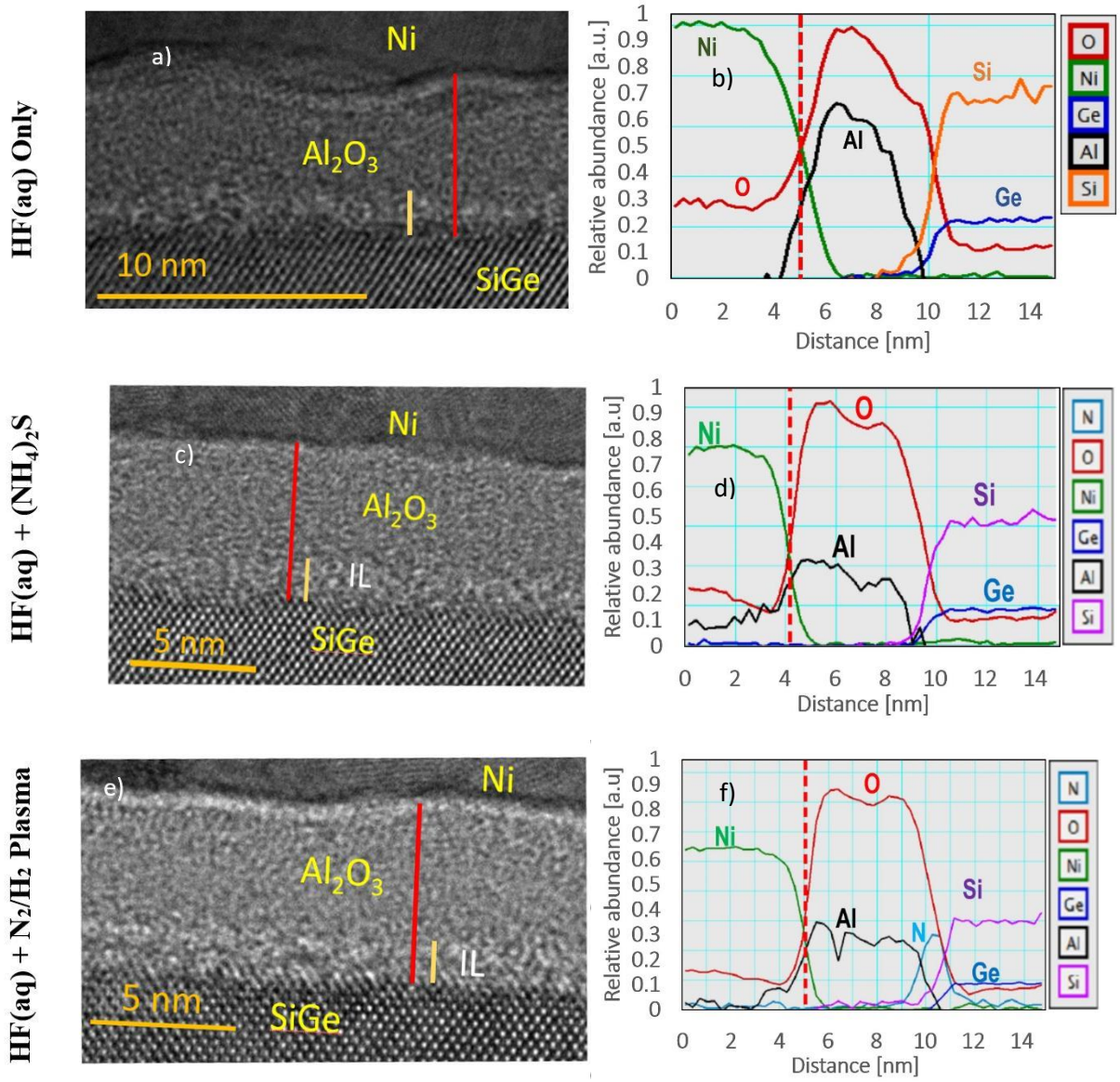

Figure 2.6: TEM and EELS of Ni/Al_2O_3/SiGe MOSCAP before and after plasma clean. (a) HRTEM of Al_2O_3/SiGe MOSCAP treated with 2% HF(aq) pre-deposition, (b) EELS spectrum line trace of Al_2O_3/SiGe treated with 2% HF(aq) pre-deposition, (c) HRTEM of Al_2O_3/SiGe MOSCAP passivated by aqueous sulfur pre-deposition, (d) EELS spectrum line trace of Al_2O_3/SiGe passivated by aqueous sulfur pre-deposition, (e) HRTEM of Al_2O_3/SiGe MOSCAP passivated by N_2/H_2 plasma pre-deposition, (f) EELS spectrum line trace of Al_2O_3/SiGe passivated by N_2/H_2 plasma pre-deposition

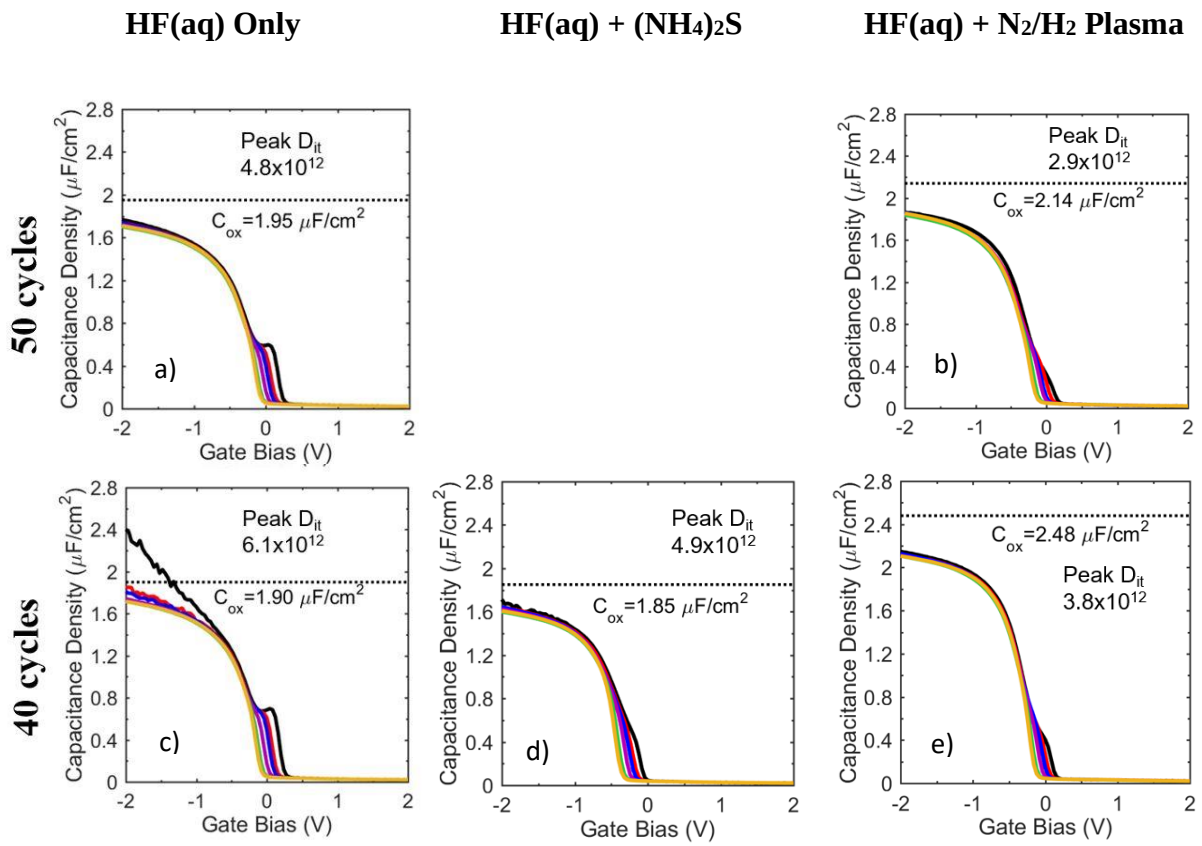

Figure 2.7: Effect of surface treatment before HfO_2 ALD on C-V characteristics. 2 kHz – 1 MHz C-V characteristics of 40 and 50 cycle Ni/HfO_2/$Si_{0.7}Ge_{0.3}$ MOSCAPs after forming gas anneal. (a) HF(aq) pre-clean only, 50 cycles ALD (b) HF(aq) clean + N_2/H_2 plasma treatment, 50 cycles ALD (c) HF(aq) pre-clean only, 40 cycles ALD (d) HF(aq) clean + ex-situ $(NH_4)_2S$ treatment, 40 cycles ALD (e) HF(aq) + N_2/H_2 plasma treatment, 40 cycles ALD. C_{ox} values were estimated using quasi-static C-V simulations.

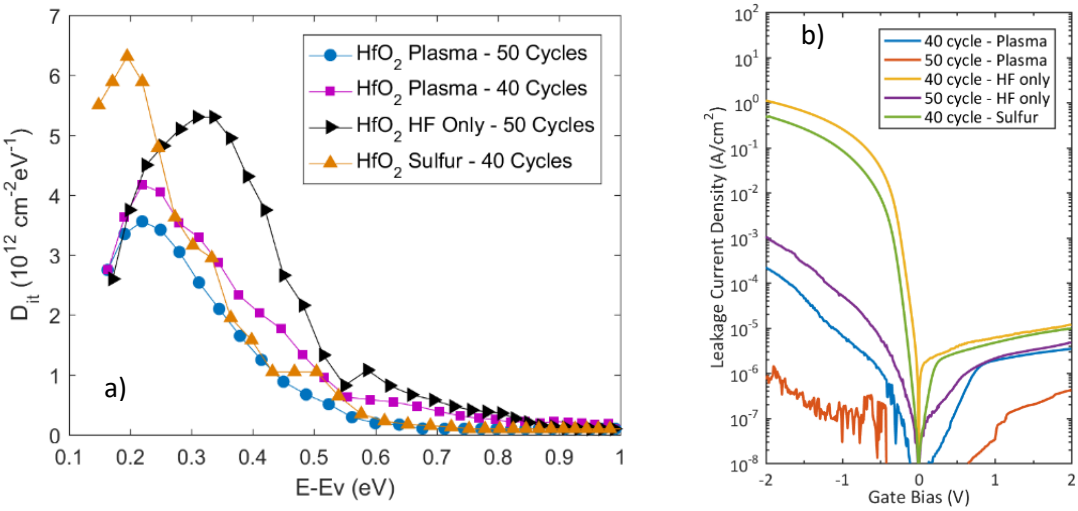

Figure 2.8: Effect of surface treatment before HfO_2 ALD on interface state density and I-V characteristics. (a) Full interface state model [29] and (b) I-V characteristics of 40 and 50 cycle Ni/HfO_2/$Si_{0.7}Ge_{0.3}$ MOSCAPs after forming gas anneal.

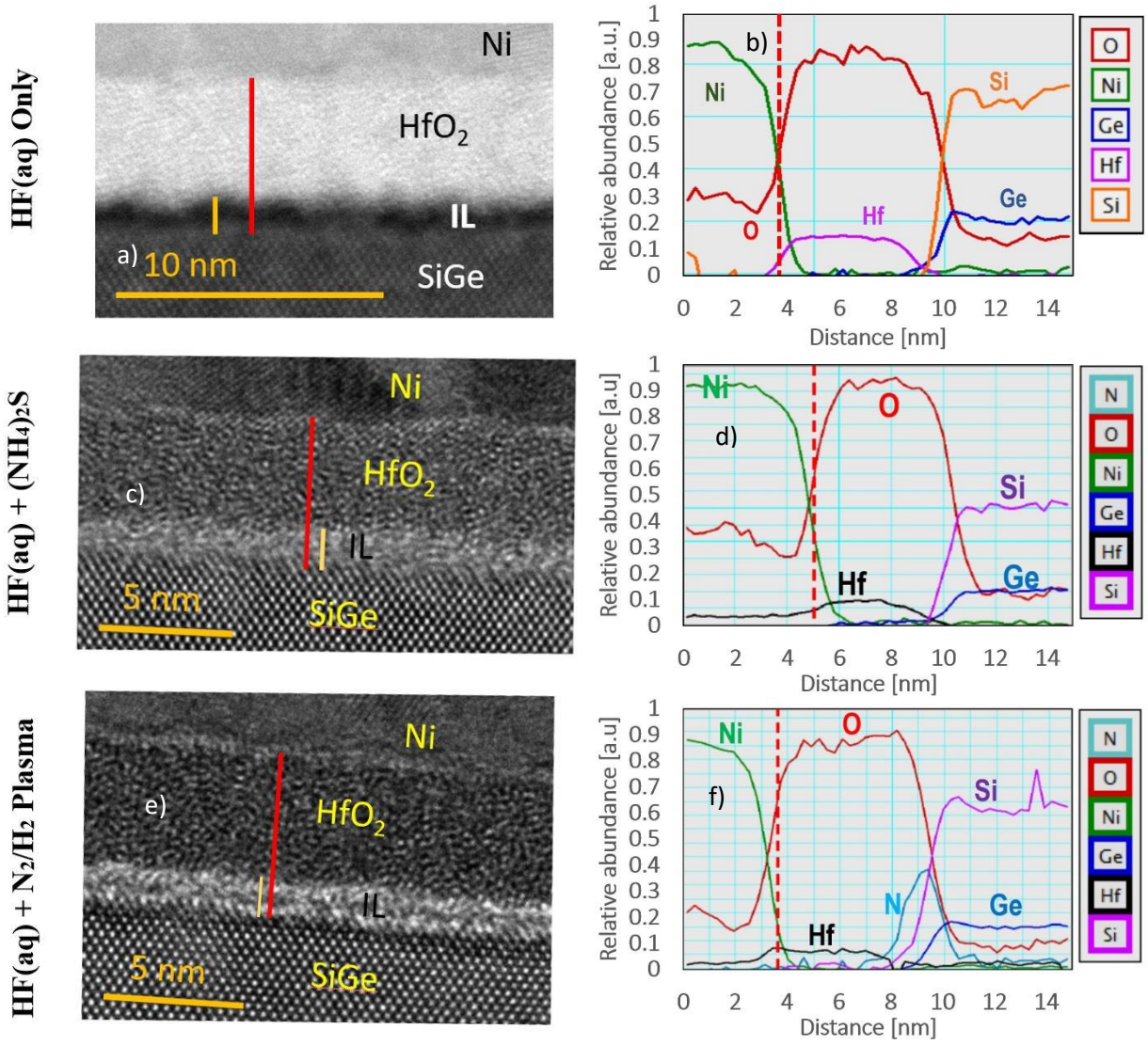

Figure 2.9: TEM and EELS of Ni/HfO_2/SiGe MOSCAP before and after plasma clean. (a) HRTEM of HfO_2/SiGe MOSCAP treated with 2% HF(aq) pre-deposition, (b) EELS spectrum line trace of HfO_2/SiGe treated with 2% HF(aq) pre-deposition, (c) HRTEM of HfO_2/SiGe MOSCAP passivated by aqueous sulfur pre-deposition, (d) EELS spectrum line trace of HfO_2/SiGe passivated by aqueous sulfur pre-deposition, (e) HRTEM of HfO_2/SiGe MOSCAP passivated by N_2/H_2 plasma pre-deposition, (f) EELS spectrum line trace of HfO_2/SiGe passivated by N_2/H_2 plasma pre-deposition

2.7 REFERENCES

[1] M. V. Fischetti and S. E. Laux, *Band structure, deformation potentials, and carrier mobility in strained Si, Ge, and SiGe alloys,* J. Appl. Phys., 2001. **80**: p. 2234.

[2] C. W. Liu, M. Östling and J. B. Hannon, *New materials for post-Si computing,* MRS Bull., 2014. **39**(8): p. 658.

[3] O. Weber, J. F. Damlencourt, F. Andrieu, F. Ducroquet, T. Ernst, J. M. Hartmann, A. M. Papon, O. Renault, B. Guillaumot and S. Deleonibus, *Fabrication and mobility characteristics of SiGe surface channel pMOSFETs with a HfO_2/TiN gate stack,*" IEEE Trans. Electron Devices, 2006. **53**(3): p. 449.

[4] A. Pruijmboom, J. W. Slotboom, D. J. Gravesteijn, C. W. Fredriksz, A. A. van Gorkum, R. A. van de Heuvel, J. M. L. van Rooij-Mulder, G. Streutker and G. F. A. van de Walle, *Heterojunction Bipolar Transistors with SiGe Base Grown by Molecular Beam Epitaxy,* IEEE Electron Device Lett., 1991. **12**(7): p. 357.

[5] J. M. Hartmann, V. Loup, G. Rolland and M. N. Séméria, *Effects of temperature and HCl flow on the SiGe growth kinetics in reduced pressure–chemical vapor deposition,* J. Vac. Sci. Technol. B., 2003. **21**(6): p. 355.

[6] T. Ghani, M. Armstrong, C. Auth, P. Charvat, G. Glass, T. Hoffmann, K. Johnson, C. Kenyon, J. Klaus, B. McIntyre, K. Mistry, J. Sandford, M. Silberstein, S. Sivakumar, P. Smith, K. Zawadzki, S. Thompson and M. Bohr, *A 90nm high volume manufacturing logic technology featuring novel 45nm gate length strained silicon CMOS transistors,* IEDM Tech Dig., 2003. **1**: p. 6-11.

[7] K. Mistry, C. Allen, C. Auth, B. Beattie, D. Bergstrom, M. Bost, M. Brazier, M. Buehler, A. Cappellani, R. Chau, C. H. Choi, G. Ding, K. Fischer, T. Ghani, R. Grover, W. Han, D. Hanken, M. Hattendorf, J. He, J. Hicks, R. Huessner, D. Ingerly, P. Jain, R. James, L. Jong, S. Joshi, C. Kenyon, K. Kuhn, K. Lee, H. Liu, J. Maiz, B. McIntyre, P. Moon, J. Neirynck, S. Pae, C. Parker, D. Parsons, C. Prasad, L. Pipes, M. Prince, P. Ranade, T. Reynolds, J. Sandford, L. Shifren, J. Sebastian, J. Seiple, D. Simon, S. Sivakumar, P. Smith, C. Thomas, T. Troeger, P. Vandervoorn, S. Williams and K. Zawadzki, *A 45 nm logic technology with high-k+metal gate transistors, strained silicon, 9 Cu interconnect layers, 193nm dry patterning, and 100% Pb-free packaging,* in IEEE Intl. Elec. Dev. Meeting, 2007: Washington, DC.

[8] E. P. Gusev, E. Cartier, D. A. Buchanan, M. Gribelyuk, M. Copel, H. Okorn-Schmidt and C. D. Emic, *Ultrathin high-K metal oxides on silicon: processing, characterization and integration issues,* Microelectron. Eng., 2001. **59**: p. 341-349.

[9] J. W. Zhang, G. He, L. Zhou, H. S. Chen, X. S. Chen, X. F. Chen, B. Deng, J. G. Lv and Z. Q. Sun, *Microstructure optimization and optical and interfacial properties modulation of sputtering-derived HfO_2 thin films by TiO_2 incorporation*, J. Alloys Compd., 2014. **611**: p. 253-259.

[10] L. Y. Huang, A. D. Li, W. Q. Zhang, H. Li, Y. D. Xia and D. Wu, *Fabrication and characterization of La-doped HfO_2 gate dielectrics by metal-organic chemical vapor deposition*, Appl. Surf. Sci., 2010. **256**: p. 2496-2499.

[11] G. He, X. Chen and Z. Sun, *Interface engineering and chemistry of Hf-based high-k dielectrics on III–V substrates*, Surf. Sci. Rep., 2013. **68**: p. 68-107.

[12] G. He, J. Gao, H. Chen, J. Cui, Z. Sun and X. Chen, *Modulating the Interface Quality and Electrical Properties of HfTiO/InGaAs Gate Stack by Atomic-Layer-Deposition-Derived Al_2O_3 Passivation Layer*, ACS Appl. Mater. Interfaces, 2014. **6**(24): p. 22013-22025.

[13] G. He, B. Deng, H. Chen, J. Lv, Y. Ma and Z. Sun, *Effect of dimethylaluminumhydride-derived aluminum oxynitride passivation layer on the interface chemistry and band alignment of HfTiO-InGaAs gate stacks*, APL Mater., 2013. **1**: p. 012104, 2013.

[14] G. He, J. Liu, H. Chen, Y. Liu, Z. Sun, X. Chen, M. Liu and L. Zhang, *Interface control and modification of band alignment and electrical properties of HfTiO/GaAs gate stacks by nitrogen incorporation*, J. Mater Chem. C., 2014. **2**: p. 5299-5308.

[15] V. Chobpattana, J. Son, J. J. M. Law, R. Engel-Herbert, C. Y. Huang and S. Stemmer, *Nitrogen-passivated dielectric/InGaAs interfaces with sub-nm equivalent oxide thickness and low interface trap densities*, Appl. Phys. Lett., 2013. **102**: p. 022907.

[16] L. Zheng, X. Cheng, D. Cao, G. Wang, Z. Wang, D. Xu, C. Xia, L. Shen, Y. Yu and D. Shen, *Improvement of Al_2O_3 Films on Graphene Grown by Atomic Layer Deposition with Pre-H_2O Treatment*, ACS Appl. Mater. Interfaces, 2014. **6**(10) p. 7014-7019.

[17] L. Zheng, X. Cheng, D. Cao, Z. Wang, C. Xia, Y. Yu and D. Shen, *Property transformation of graphene with Al_2O_3 films deposited directly by atomic layer deposition*, Appl. Phys. Lett., 2014. **104**: p. 023112.

[18] Y. Oshima, Y. Sun, D. Kuzum, T. Sugawara, K. C. Saraswat, P. Pianetta and P. C. McIntyre, *Chemical Bonding, Interfaces, and Defects in Hafnium Oxide/Germanium Oxynitride Gate Stacks on Ge(100)*, J. Electrochem. Soc., 2008. **155**(12): p. G304.

[19] P. Bhatt, K. Chaudhuri, S. Kothari, A. Nainani and S. Lodha, *Germanium oxynitride gate interlayer dielectric formed on Ge(100) using decoupled plasma nitridation*, Appl. Phys.

Lett., 2013. **103**: p. 172107.

[20] N. Lu and W. Bai, *Ge diffusion in Ge metal oxide semiconductor with chemical vapor deposition HfO_2 dielectric,* Appl. Phys. Lett., 2005. **87**: p. 051922.

[21] J. Han, R. Zhang, T. Osada, M. Hata, M. Takenaka and S. Takagi, *Reduction in Interface Trap Density of Al_2O_3/SiGe Gate Stack by Electron Cyclotron Resonance Plasma Post-nitridation,* Appl. Phys. Express, 2013. **6**: p. 051302.

[22] K. Sardashti, K. T. Hu, K. Tang, S. Park, H. Kim, S. Madisetti, P. McIntyre, S. Oktyabrsky, S. Siddiqui, B. Sahu, N. Yoshida, J. Kachian and A. Kummel, *Sulfur passivation for the formation of Si-terminated Al_2O_3/SiGe(0 0 1) interfaces,* Appl. Surf. Sci., 2016. **366**: p. 455-463.

[23] K. Sardashti, K. T. Hu, K. Tang, S. Madisetti, P. McIntyre, S. Oktyabrsky, S. Siddiqui, B. Sahu, N. Yoshida, J. Kachian, L. Dong, B. Fruhberger and A. C. Kummel, *Nitride passivation of the interface between high-k dielectrics and SiGe,* Appl. Phys. Lett., 2016. **108**: p. 011604.

[24] L. Zheng, X. Cheng, P. Ye, L. Shen, Q. Wang, D. Zhang, Z. Wang, Y. Yu and X. Yu, *Semiconductor-like nanofilms assembled with AlN and TiN laminations for nearly ideal graphene-based heterojunction devices,* J. Mater. Chem. C., 2016. **4**: p. 11067-11073.

[25] N. M. Johnson, J. Walker, C. M. Doland, K. Winer and R. A. Street, *Hydrogen incorporation in silicon thin films deposited with a remote hydrogen plasma,* Appl. Phys. Lett., 1989. **54**: p. 1872.

[26] M. S. Kavrik, E. Thomson, E. Chagarov, K. Tang, S. T. Ueda, V. Hou, T. Aoki, M. Kim, B. Fruhberger, Y. Taur, P. C. McIntyre and A. C. Kummel, *Ultralow Defect Density at Sub-0.5 nm HfO_2/SiGe Interfaces via Selective Oxygen Scavenging,* ACS Appl. Mater. Interfaces, 2018. **10**(36): p. 30794-30802.

[27] E. H. Nicollian and A. Goetzberger, *The Si-SiO_2 interface – electrical properties as determined by the metal-insulator-silicon conductance technique,* Bell Syst. Tech. J., 1967. **46**: p. 1055.

[28] H. P. Chen, Y. Yuan, J. Ahn, P. C. McIntyre, P. M. Asbeck, M. J. W. Rodwell and Y. Taur, *Interface-State Modeling of Al_2O_3 –InGaAs MOS From Depletion to Inversion,* IEEE Trans. Electron Devices, 2012. **59**: p. 2383.

[29] Y. Yuan, B. Yu, P. C. McIntyre, P. M. Asbeck, M. J. W. Rodwell and Y. Taur, *A distributed bulk-oxide trap model for Al_2O_3 InGaAs MOS devices,* IEEE Trans. Electron Devices,

2012. **59**: p. 2100.

[30] M. Bosman, M. Watanabe, D. T. L. Alexander and V. J. Keast, *Mapping chemical and bonding information using multivariate analysis of electron energy-loss spectrum images,* Ultramicroscopy, 2006. **106**(11-12): p. 1024-1032.

[31] E. H. Poindexter, G. J. Gerardi, M. E. Rueckel and P. J. Caplan, *Electronic traps and Pb centers at the Si/SiO_2 interface: Band-gap energy distribution,* J. Appl. Phys., 1984. **56**: p. 2844.

[32] N. H. Thoan, K. Keunen, V. V. Afanas'ev and A. Stesmans, *Interface state energy distribution and Pb defects at Si(110)/SiO_2 interfaces: Comparison to (111) and (100) silicon orientations,* J. Appl. Phys., 2011. **109**: p. 013710.

[33] V. V. Afanas'ev, Y. G. Fedorenko and A. Stesmans, *Interface traps and dangling-bond defects in (100)Ge/HfO_2,* Appl. Phys. Lett., 2005. **87**: p. 032107.

[34] M. Houssa, G. Pourtois, M. Caymax, M. Meuris, M. M. Heyns, V. V. Afanas'ev and A. Stesmans, *Ge dangling bonds at the (100)Ge/GeO_2 interface and the viscoelastic properties of GeO_2,* Appl. Phys. Lett., 2008. **93**: p. 161909.

[35] Y. Saito, K. Sekine, M. Hirayama and T. Ohmi, *Low-Temperature Formation of Silicon Nitride Film by Direct Nitridation Employing High-Density and Low-Energy Ion Bombardment,* Jpn. J. Appl. Phys., 1999. **38**: p. 2329.

[36] M. Edmonds, K. Sardashti, S. Wolf, E. Chagarov, M. Clemons, T. Kent, J. H. Park, K. Tang, P. C. McIntyre, N. Yoshida, L. Dong, R. Holmes, D. Alvarez and A. C. Kummel, *Low temperature thermal ALD of a SiN_x interfacial diffusion barrier and interface passivation layer on Si_xGe_{1-x}(001) and Si_xGe_{1-x}(110),* J. Chem. Phys., 2017. **146**: p. 052820.

[37] L. Soukup, V. Peřina, L. Jastrabík, M. Šícha, P. Pokorný, R. J. Soukup, M. Novák and J. Zemek, *Germanium nitride layers prepared by supersonic r.f. plasma jet,* Surf. Coat. Technol., 1996. **78**: p. 280.

Chapter 3

Proximity Effects of the Selective Atomic Layer Deposition of Cobalt on the Nanoscale: Implications for Interconnects

3.1 ABSTRACT

The continued scaling of transistor sizes has motivated the need to replace Cu with alternate metals to minimize resistivity, with cobalt being of interest for both interconnect via metallization as well as emerging die-bonding processes. The atomic layer deposition of cobalt using $Co(tBu_2DAD)_2$ and tertiary-butyl amine (TBA) has nearly infinite selectivity (>1000 cycles) on metallic vs. insulating (SiO_2 or low-k SiCOH dielectric) planar samples. However, on patterned samples, selectivity under identical ALD conditions is limited, due to the diffusion of molecularly-adsorbed metal precursors from reactive to non-reactive surfaces. X-ray photoelectron spectroscopy (XPS) and scanning electron microscopy (SEM) were employed to investigate the effects of process parameters on surface precursor diffusion to determine the mechanism of selectivity loss on the nanoscale. Top-down SEM and XPS spectra of a striped test pattern of Cu and SiO_2 indicated that selective vapor-phase passivation of SiO_2 improved selectivity for deposition on Cu vs SiO_2 by reducing the number of insulator defects that facilitate trapping of precursor molecules and subsequent Co nucleus growth. The remaining nuclei were present due to incomplete defect passivation. Conversely, near-perfect selectivity during Co ALD was obtained with the periodic annealing of the substrate, consistent with a low temperature reflow process allowing Co nuclei on SiO_2 defects to merge with the metallic growth surface.

3.2 Introduction

With continued scaling of transistors to smaller nodes, the increasing resistivity of Cu interconnects deposited by electrodeposition in middle-of-line (MOL) and back-end-of-line (BEOL) processing motivates the search for alternate interconnect metals and deposition techniques at the M0/M1 interconnect layers [1][2]. One such metal is Co, which has been shown to be effective as a Cu capping layer to protect Cu from oxidation and as a Cu replacement in tightly confined vias where electroplating Cu is more difficult [3][4]. Atomic layer deposition (ALD) is an effective method to deposit Co due to its controllability of thickness and conformality over high-aspect ratio structures. In addition, different surface chemistries can be exploited to allow for area-selective deposition, enabling bottom-up fill on metals [5]. Bottom-up fill in interconnect vias has previously been explored as a means of avoiding void formation during ALD of metals [6], but is also hypothesized to encourage vertical grain growth, thereby limiting the effects of grain boundary scattering. Another novel application of such a selective Co ALD process is in the bonding of suspended Cu pads to form electrical contacts, enabling tighter-packed connections between bonded dies during packaging [7]. Selective ALD of Co metal has previously been reported using several precursors such as $Co(AMD)_2$ and (^{t}Bu-Allyl)$Co(CO)_3$ [8][9]. Of special interest is one selective Co ALD process reported by the Winter group using bis(1,4-di-tert-butyl-1,3-diazadienyl) cobalt ($Co(tBu_2DAD)_2$) and formic acid at 180 C, exhibiting very high selectivity towards metals vs insulators [10][11]. Additional studies on the deposition of Co using $Co(tBu_2DAD)_2$ were performed using tert-butyl amine to avoid oxidation of metallic substrates [12][13].

During area-selective ALD on conductors vs insulators, loss of selectivity can result from surface defects (such as hydroxyl groups) on insulators causing unwanted nucleation [14]. This problem is magnified by close proximity to the desired growth surface, where it is hypothesized

that excess precursor remaining weakly-bound on the growth surface may diffuse onto the insulator. The diffused precursor may then bind with surface defects and subsequently react with the ALD coreactant (for example, a metal precursor reacting with a reducing agent) in the next ALD half-cycle to form nuclei for subsequent growth [15]. Grillo *et. al.* argue that the surface diffusion of excess metal precursor on insulator surfaces can lead to the formation of nanoparticle nuclei which can serve as points for unwanted nucleation on insulators [16][17]. Hydroxyl groups present on SiO_2-based insulators which serve as binding sites for precursors can be deactivated through the use of Si-based vapor-phase passivants prior to deposition, thereby enhancing area-selectivity during metal ALD [18]. This study seeks to understand the mechanism by which unwanted Co nuclei appear on insulators within a few nanometers of the metallic growth surface, and compares optimization techniques to improve selectivity and determine the atomistic mechanisms of selectivity enhancement. In-situ XPS and ex-situ SEM are used to characterize the loss of selectivity during Co deposition on nanoscale test strips of alternating Cu/SiO_2 surfaces. SEM and transmission electron microscopy (TEM) illustrate that periodic anneals induce low temperature reflow of these nanoscale nuclei, greatly improving selectivity on the nanoscale.

3.3 Experimental Methodology

In this report, Co ALD was performed using the coreactants $Co(tBu_2DAD)_2$ (EMD Performance Materials, Inc.) and TBA at 180 °C on a test pattern consisting of Cu stripes embedded in SiO_2 [12][13]. In this process, the $Co(tBu_2DAD)_2$ precursor bound to the Cu metal surface engages in ligand exchange with the dosed TBA to form Co metal plus amine ligands, which are subsequently desorbed during pump-down as described in Eq. 1 and Fig. 3.1.

Co half-cycle: $Co(tBu_2DAD)_2(g) + Co(s) \rightarrow Co(tBu_2DAD)_2(ad)$

TBA half-cycle: $Co(tBu_2DAD)_2(ad) + 2tBuNH_2(g) \rightarrow (tBuNH_2)_2Co(ad) + 2(tBu_2DAD)(g)$

Desorption step: $(tBuNH_2)_2Co(ad) \rightarrow Co(s) + 2tBuNH_2(g)$

Eq. 1. Half-cycle reactions for Co(DAD)$_2$ + TBA Co ALD process

Fig. 3.2a) is a top-down SEM image (see full image in Fig. S1 in Supporting Information) of the test pattern prior to Co ALD, consisting of 85 nm wide strips of Cu deposited via electrodeposition on a TiN/Si substrate, then planarized by chemical-mechanical polishing (CMP). A degrease and 0.5% HF clean were performed on the post-CMP samples to minimize surface contamination. Prior to deposition, all samples were cleaned with acetone, methanol, and water rinses, followed by a final 30 second 0.5% HF dip prior to being mounted on a sample holder and loaded into the load lock of the deposition and analysis chamber. The analysis chamber (Fig. S2 in Supporting Information) consists of a load-lock, deposition chamber for ALD, and UHV chamber (~10^{-10} Torr base pressure) containing the x-ray source and analyzer for XPS. Once loaded, samples were first transferred into the UHV chamber for a 30 minute 350 ºC vacuum anneal using a pyrolytic boron nitride heater to remove residual airborne carbon contaminants and leave a clean starting substrate. The deposition chamber and dosing lines were pumped with a turbomolecular pump (Pfeiffer TMP-151C) with a base pressure of 10^{-6} Torr, and the wall temperature was maintained at 125 ºC. The sample stage was heated to 180 ºC through an enclosed cartridge heater inside a Cu block welded to a high-vacuum flange to eliminate the possibility of hot-wire CVD reactions. The turbomolecular pump was used to pump away precursor gas between pulses to avoid possible O_2 contamination from purge gas and to prevent any parasitic CVD component that might lead to undesired nucleation. The Co(tBu_2DAD)$_2$ precursor bottle temperature was 120ºC, and the dosing lines were kept 10-20ºC higher to avoid condensation of precursor in lines. Ultrahigh purity N_2 was passed through a purifier before being sent through the precursor bottle at 1 Torr to act as a carrier gas for delivery to the deposition chamber. The Co(tBu_2DAD)$_2$ precursor bottle was refilled with carrier gas for 200 ms, followed by a 200 ms

pulse into the ALD reactor at a pressure of ~200 mTorr, which is repeated for each pulse of precursor. To achieve the required precursor dose, multiple pulses of precursor per half-cycle were employed, as the compression ratio of the turbomolecular pump drops drastically above the mTorr range, limiting pumping speed. The co-reactant tert-butyl amine (Me_3CNH_2, TBA, Sigma-Aldrich) was kept at 25°C and dosed in 20 ms pulses to limit pressure spikes to 1 Torr. No purge gas was used between half-cycles to limit potential oxygen incorporation in the deposited Co, with the pump-out time of precursor varied as a process parameter. The resulting ALD sequence was $Co(tBu_2DAD)_2$ dose followed by pump-out, dose of TBA, and finished with a 20 s pump-out.

After deposition, samples were transferred *in situ* to the UHV chamber for XPS. A monochromatic XM1000 MkII/SPHERA system (Omicron Nanotechnology GmbH) was used to collect XPS spectra with an Al kα source at 1486.7 eV, with an analyzer pass energy of 50 eV and linewidth of 0.1 eV. XPS spectra were collected at 60° with respect to the sample surface normal. XPS quantification was performed using CASA XPS 2.3 software, with raw peak areas corrected via Scofield photoionization cross-sectional relative sensitivity factors. Due to the presence of uncompensated sample charging during XPS, the location of the Si 2p peak was used to establish the charge shift in XPS spectra based on the known Si 2p peak location for SiO_2 of 103 eV per-sample, and applied to the Co 2p3/2 peak to verify the presence of Co metal. Top-down SEM was also performed after Co ALD using a FEI Apreo SEM at 2 kV electron voltage and 0.05 nA emission current using a backscatter electron detector. Finally, cross-sectional transmission electron microscopy (TEM) of the Cu/SiO_2 striped patterns was performed.

3.4 Results & Discussion

The $Co(tBu_2DAD)_2$ + TBA ALD process was employed on patterned substrates with Cu lines separated by SiO_2 (Fig. 3.2a, Fig. S1 in Supporting Information). In Fig. 3.2(b) (Fig. S3 in Supporting Information), XPS quantification shows significant attenuation of both Cu and Si signals from 18% to 2.1% Cu coverage and 34% to 20% Si coverage compared with the pre-deposition surface. SEM imaging shows the presence of a significant amount of Co nuclei on the SiO_2, with a density highest near the Cu and decreasing with distance from the stripes. In addition, nearly all of the nuclei are of similar diameter, with 95% of particles being between 230 nm^2 to 298 nm^2 with oblong disc shapes as observed in SEM and TEM imagery. From the work of *Wolf et. al*, observed selectivity on un-patterned SiO_2 during Co ALD with $Co(tBu_2DAD)_2$ is consistent with the lack of molecular adsorption [12]. Nuclei 2-4nm tall are observed by AFM on blanket SiO_2, but it is hypothesized that there are more hydroxyl groups on patterned SiO_2 due to defects formed during CMP of the surface compared with thermally-grown SiO_2, so that the proximity of the Co/Cu surfaces is more likely to result in unwanted adsorption of Co precursor on the hydroxyl groups, and, therefore, unwanted nucleation.

3.4.1 Passivation of insulator defects

To confirm this hypothesis, a Cu/SiO_2 patterned sample was passivated with vapor-phase dimethylamino-dimethyl-silazane ($(Me_2N)_2SiMe_2$, DMADMS) and tetramethyl-disilazane ($(Me_2SiH)_2NH$, TMDS) in a 50% mixture of both species at 5 Torr for 10 minutes at 70°C, followed by deposition of 200 Co ALD cycles. TMDS and DMADMS are commonly used for SiCOH repair, as they readily bind to hydroxyl groups formed via plasma damage during dry etching [19]. Simultaneous vapor-phase dosing of both TMDS and DMADMS was employed to silylate both isolated and geminal hydroxyl groups on SiO_2 [20]. Fig. 3.2(c) (Fig. S4 in Supporting Information) shows the SEM of the passivated SiO_2/Cu striped surface after Co ALD. On the

passivated surface, XPS quantification (raw XPS spectra shown as Figs. S9 before deposition, S10 after deposition without passivation, and S7 after deposition with passivation in Supporting Information) shown in the bottom of Fig. 3.2(c) after 200 ALD cycles shows only 13% Co and 33% Si, similar to the clean surface and therefore consistent with lower Co coverage on the SiO_2. To determine the chemical state of the Co layer deposited, the chemical shift of the Co2p peak was measured. On both the unpassivated and the passivated samples, the peak location of the Co2p3/2 peak after correction for uncompensated sample charging was centered at 778 eV, consistent with metallic Co formation (see Figs. S10 and S11 in Supporting Information for peak shifts and charge correction factors).

SEM imaging in Fig. 3.2(b,c) shows a high density of Co nuclei on the unpassivated SiO_2, with a far lower density on the unpassivated SiO_2, consistent with the XPS data. Unlike the unpassivated sample, however, the distribution of Co nuclei on the insulator is far more evenly distributed. For any unwanted nuclei formed on the unpassivated insulator surface in the initial ALD cycles, it is hypothesized that subsequent cycles will see these nuclei act as adsorption sites in subsequent cycles. Since the number of defect sites on SiO_2 is expected to be a fixed number throughout the process, nucleation should occur within the first few cycles for most sites, resulting in further growth leading to nuclei of a similar size. The nuclei density on the passivated SiO_2, however, is expected to be lower due to the presence of fewer defect sites, with remaining nuclei being present due to incompletely passivated hydroxyl groups. These SEM and XPS observations, therefore, are consistent with unwanted nuclei being formed by diffusion of the $Co(tBu_2DAD)_2$ precursor from the Cu strip to a fixed number of defects on the SiO_2, where it is trapped and converted to Co with subsequent TBA pulses. The fixed number of defects can be reduced by vapor-phase passivation of hydroxyl groups, resulting in a lower density of Co nuclei.

As mentioned, the presence of unwanted nuclei on the unpassivated insulator is significantly greater than that of the unpassivated insulator. To quantify the density of unwanted nuclei on the insulator, the image analysis software ImageJ was used to identify and sort nuclei as a function of distance from the stripe edges [21]. Fig. 3.3 illustrates the difference in unwanted nucleation density with a histogram of the number of nuclei as a function of distance from the top striped pattern in the 600 nm wide insulator alley. On the unpassivated Cu/SiO_2 pattern (Fig. 3.3a), there is a gradual drop off in nuclei density with distance from the top edge of the striped pattern to the middle of the alley with an overall nuclei coverage of 19% and density of 294 nuclei/μm^2. On the passivated sample (Fig. 3.3b), a decrease in nuclei count to a density of 114 nuclei/μm^2 and an overall coverage overall coverage of 5% is observed, with a near-constant nuclei density across the insulator. As the pump-out time between cycles is on the order of seconds, precursor molecules should have sufficient time to diffuse or desorb off the insulator surface before the co-reactant can react to form a nucleus, leaving the defect density on the insulator as the limiting factor in nuclei density. With the passivated surface, the defect density is reduced by the presence of fewer hydroxyl groups, further limiting the number of sites where a nucleus can be formed. This result, therefore, is consistent with passivation offering $Co(tBu_2DAD)_2$ physisorbed on the insulator fewer sites to be trapped on before diffusing back to the growth surface or desorbing entirely. Future work in the numerical modeling of surface diffusion in area-selective ALD, therefore, should account for the presence of defects that trap excess precursor to capture this effect.

3.4.2 Size distribution of nuclei on insulator defects

Fig. 3.4 (full histograms in Fig. S5 and S6 for unpassivated and passivate surfaces, respectively) illustrates the nuclei size distribution on the insulator surface. The mean nucleus size on the passivated surface is 458 nm^2, with a standard deviation of 181 nm^2 and skewness of -.22.

On the unpassivated sample, the average nucleus size is 503 nm^2 with a standard deviation of 155 nm^2 and skewness of 0.83. Given the model of surface diffusion onto insulator defects, it is expected that mean nuclei sizes be larger on the passivated surface due to the presence of fewer total sites for a given flux of excess precursor. However, a smaller mean nuclei size is observed on the passivated surface with a negatively-skewed distribution, contrary to this model. One possible explanation for this is that delayed nucleation on marginally passivated sites occurs later during deposition, resulting in smaller nuclei at those sites. On the unpassivated surface, the distribution is positively-skewed, with many larger nuclei observed. One possibility is that two nuclei in close proximity grow together to form a single large nucleus during growth. The second possibility is an artifact of the finite sharpness of the SEM images, resulting in two (or more) close nuclei falsely appearing as a single larger nucleus. Due to the far higher nuclei density on the unpassivated surface, the positive skewness of the nuclei size distribution is consistent with a combination of these two factors.

The small insulator areas in between the Cu stripes were also examined for undesired nuclei. As the area of the insulator is comparable to the area of the Cu fingers, precursor molecules are equally likely to land on insulator as they are on metal. Once precursors trapped by insulator defects form initial nuclei, further cycles may result in precursor directly adsorbing on these nuclei, with the growing nuclei likely to form an undesired bridge between the Cu lines. Quantification in this region was again performed using the above-mentioned method. Any detected nuclei overlapping the Cu stripes were discarded from the count, as well as nuclei touching the edge of the image in order to get a consistent count of nuclei sizes. Fig. 3.5(a) is a top-down SEM image of the striped portion of the Cu/SiO_2 pattern without passivation along with a histogram of the nuclei size distribution (Fig. S3 in Supporting Information, full histogram in Fig. S7), while 3.5(b)

is the same portion with passivation (Fig. S4 in Supporting Information, full histogram in Fig. S8). The distribution of nuclei sizes on the passivated sample is centered around a mean value of 496 nm^2 with a standard deviation of 123 nm^2 and skewness of 0.62, while on the unpassivated sample, a similar distribution with a mean nuclei size of 470 nm^2, standard distribution of 185 nm^2, and skewness of 0.60 is observed. Although the nuclei density is far lower for the passivated surface, the size distribution of nuclei on both surfaces is similarly skewed upward, with the unpassivated surface having a longer tail of sizes reflecting the greater presence of multiple nuclei in proximity being counted as one. The presence of larger particles on average after passivation is consistent with a lower defect density allowing precursor to more readily diffuse and re-absorb onto the metal strips, with the remaining nuclei able to capture more excess precursor.

While the possibility that Cu contamination on the insulator during the CMP process is the source of Co nucleation was considered, if Cu contamination were the driving force behind undesired nucleation, the spatial distribution of nuclei should remain unchanged after passivation; however, the observed distribution is consistent with defect sites primarily being hydroxyl groups, not Cu contaminant sites. These results, therefore, confirm the hypothesis that the loss of selectivity on the nanoscale is due to surface precursor diffusion to defects. With a higher sticking probability, metal surfaces will experience precursor saturation before the insulator surface, resulting in a concentration gradient that can drive diffusion and cause unwanted growth.

3.4.3 Effect of dose and cycle time on nucleation density

The $Co(tBu_2DAD)_2$ + TBA ALD is unusual because XPS data is consistent with molecular instead of dissociative chemisorption of $Co(tBu_2DAD)_2$ at 180 °C; previous XPS studies with this precursor show that the tBu_2DAD ligands are largely intact after the surface is dosed with $Co(tBu_2DAD)_2$ [12]. This implies that the $Co(tBu_2DAD)_2$ adsorption is reversible; therefore, it

was hypothesized that selectivity could also be improved by increasing the pump-out time so that $Co(tBu_2DAD)_2$ which diffused onto the SiO_2 could desorb before the subsequent TBA pulse reacted with the tBu_2DAD ligands from $Co(tBu_2DAD)_2$ to induce irreversible adsorption. To study the effect of these process parameters on nucleation density, pump-out time and dose amount were varied without the use of a passivant. As shown in Fig. 3.6 (SEM images Figs. S12 and S13, cross-sectional TEM Figs. S14 and S15 respectively in Supporting Information), increasing the pump-out time from 5 s to 20 s decreased the density of unwanted nuclei, consistent with the $Co(tBu_2DAD)_2$ diffusion and the reversible adsorption hypotheses. As with the passivation comparison, nuclei density on the insulator surface away from the edges of the stripes was quantified, with a decrease from 52 nuclei/μm^2 to 9 nuclei/μm^2 when the pump-out time is increased. However, inspecting the narrow insulator stripes between adjacent Cu stripes shows relatively little decrease in nucleation density, and XPS quantification (raw XPS spectra Fig. S16 and S17 in Supporting Information, respectively) shows a negligible difference in the surface coverage of Co vs Cu.

The $Co(tBu_2DAD)_2$ likely initially adsorbs strongly to the Co metallic growth surface, but during each ALD cycle, excess $Co(tBu_2DAD)_2$ is employed to ensure saturation on the growth surface as illustrated in Fig. 3.7(a). Therefore, at the end of each $Co(tBu_2DAD)_2$ pulse, weakly adsorbed $Co(tBu_2DAD)_2$ is present on the metal surface, as illustrated in Fig. 3.7(b). It was hypothesized that during each ALD cycle, once the growth surface was saturated with $Co(tBu_2DAD)_2$, further dosing would result in this weakly-adsorbed precursor to diffuse onto the SiO_2 (Fig. 3.7c). This excess precursor can diffuse across the SiO_2 until it reaches a surface hydroxyl or a preexisting Co defect nucleus to react (Fig. 3.7d), or desorbs. To test this hypothesis, a lower $Co(tBu_2DAD)_2$ dose was employed by reducing the number of pulses per cycle. As shown

by SEM in Fig. 3.6 (Fig. S13 and S18 in Supporting Information), this was very effective in reducing the number of unwanted nuclei on the SiO_2, with zero observed nuclei on the insulator surface, but the growth rate was significantly reduced. XPS quantification of the 8x and 2x pulse conditions shows a factor of 2 reduction in Co surface coverage as seen in the XPS quantification in Fig. 3.6, and lower Cu attenuation, consistent with a lower growth rate. To confirm this growth rate decrease, thickness was estimated by TEMs in Figs. S14 and S19 in Supporting Information. The average thickness of the Co film deposited with the 8x pulse condition was determined to be 15nm, while the average thickness under the 2x pulse condition was 7.6nm, a factor of 2 reduction.

Cross-sectional TEM was performed as shown in Fig. 3.8 to further illustrate the effects of pump time and dose process parameters absent passivation. In Fig. 3.8(a) (full image included in Supporting Information as Fig. S14), unwanted nucleation density on the Cu/SiO_2 strip pattern is high, consistent with the top-down SEM results. In Fig. 3.8(b) (full image included Supporting Information as Fig. S19), reduced Co dosing resulted in a thinner layer of Co on Cu, consistent with a lower growth rate as confirmed by XPS studies (see Fig. S24 in Supporting Information for raw XPS spectra). In Fig. 3.8(c) (full image included in Supporting Information as Fig. S15), the increased pump-out time reduces, but does not eliminate, unwanted nucleation.

3.4.4 Reflow of nuclei on insulator

Current Co CVD fill processes for interconnect vias use reflow to ensure a void-free via fill. During Co CVD growth, the Co film layer grows inward until the via closes up, leaving behind a void. To eliminate this void, an anneal is performed at roughly 350-400 °C to reflow the Co metal to fully fill the via [22]. Another method hypothesized to improve selectivity is to introduce a periodic anneal step in between sets of cycles to act as a mid-deposition reflow. According to the simple Ostwald ripening model, atoms from small nuclei can more readily diffuse than atoms from

large nuclei; therefore, by annealing the surface periodically during deposition while nuclei are smaller, it may be possible to induce Co diffusion from the nuclei to the Co/Cu stripes at a lower temperature than a typical reflow process. To test this hypothesis, after each 100 Co ALD cycles an anneal to 260°C for 30 minutes in ultra-high-vacuum was performed, which is around 140°C below the normal Co reflow temperature [22][23][24]. As the temperature of Co ALD is far below the anneal temperature and cycle times are on the order of 50x shorter than the anneal time, diffusion of Co nuclei is expected to be negligible during growth, necessitating the periodic anneal step.

TEM cross-sections of the Cu/SiO_2 fingers along with XPS quantification are shown in Fig. 3.9 for both non-annealed and annealed samples. TEM (full images available in Supporting Information as Figs. S14 and S21, respectively) shows that without periodic anneals (Fig. 3.9a), nuclei are observed on the insulator in addition to the Cu stripes. On the annealed sample in Fig. 3.9(b), however, the formation of a bulge (seen using the red arrow) at the edges of the stripes is observed. Furthermore, SEM imagery of the non-annealed and annealed samples (Supporting Information Figs. S22 and S23, respectively) shows that periodically annealing the sample every 100 cycles completely prevented the formation of nuclei on the insulator. XPS of the non-annealed and annealed samples (full XPS spectra of each element available in Supporting Information as Figs. S16 and S24, respectively), likewise, shows less insulator attenuation and greater Co signal on the annealed sample than on the non-annealed sample, consistent with near-perfect selectivity on the Cu/SiO_2 pattern without the use of passivation. This observation is consistent with the reflow of Co nuclei below a critical diameter on the SiO_2 to the edges of the Cu growth surface, forming an edge bulge as it binds to the existing Co metal layer. As the temperature of this anneal is 140 °C lower than that of typical reflow processes, this has the potential to further scale the

thickness of the diffusion barrier between the Co and the SiCOH. An alternative to the periodic anneal process while exploiting this reflow effect would be a hypothetical higher-temperature selective ALD process for Co where dissociation occurs only on metal surfaces at temperatures around 250-300 °C to continually reflow during deposition and prevent nuclei from forming on insulator. Selective Co ALD processes have been reported around 350 °C, but require the use of a self-assembled monolayer to block deposition on the undesired growth region first [25]. Periodically annealing allows the high selectivity of passivated area-selective ALD while avoiding the need for a long blocking layer which may limit the usefulness of Co in highly-confined interconnect vias.

3.5 CONCLUSION

The proximity effect of unwanted nucleation of metals on insulator by excess precursor during of selective-area ALD of Co is demonstrated using the precursor $Co(tBu_2DAD)_2$ with tert-butyl amine as a co-reactant. Four strategies have been found to improve Co ALD selectivity: adding a passivant to remove insulator defect sites, increasing the pump-out time, decreasing the precursor dose, and periodic annealing. The periodic annealing technique allows reabsorption of the Co nuclei from the insulator surface to the growth surface and is consistent with a low temperature reflow process. The strategies of passivation and periodically annealing the film to avoid Co nuclei are of great importance when considering integration of selective Co deposition by ALD in tightly-confined patterns for interconnects, as well as emerging applications in the bonding of suspended Cu pads for die-die bonding in IC packaging.

3.6 ACKNOWLEDGMENT

This work was supported in part by the Applications and Systems-Driven Center for Energy Efficient Integrated Nano Technologies (ASCENT), one of six centers in the Joint University Microelectronics Program (JUMP), an SRC program sponsored by the Defense Advanced Research Program Agency (DARPA). The authors would also like to gratefully acknowledge support from Applied Materials. This work was also performed in part at the San Diego Nanotechnology Infrastructure (SDNI) of UCSD, a member of the National Nanotechnology Coordinated Infrastructure, which is supported by the National Science Foundation (Grant ECCS-1542148).

Chapter 3, in full, is a reprint of the material as it appears in ACS Applied Nano Materials. M. Breeden, V. Wang, J. Spiegelman, A. Anurag, S. F. Wolf, D. Moser, R. K. Kanjolia, M. Moinpour, J. Woodruff, S. Nemani, K. Wong, C. H. Winter, A. C. Kummel. *Proximity Effects of the Selective Atomic Layer Deposition of Cobalt on the Nanoscale: Implications for Interconnects*. ACS Appl. Nano Mater., 2021. **4**: p. 8447-8454.

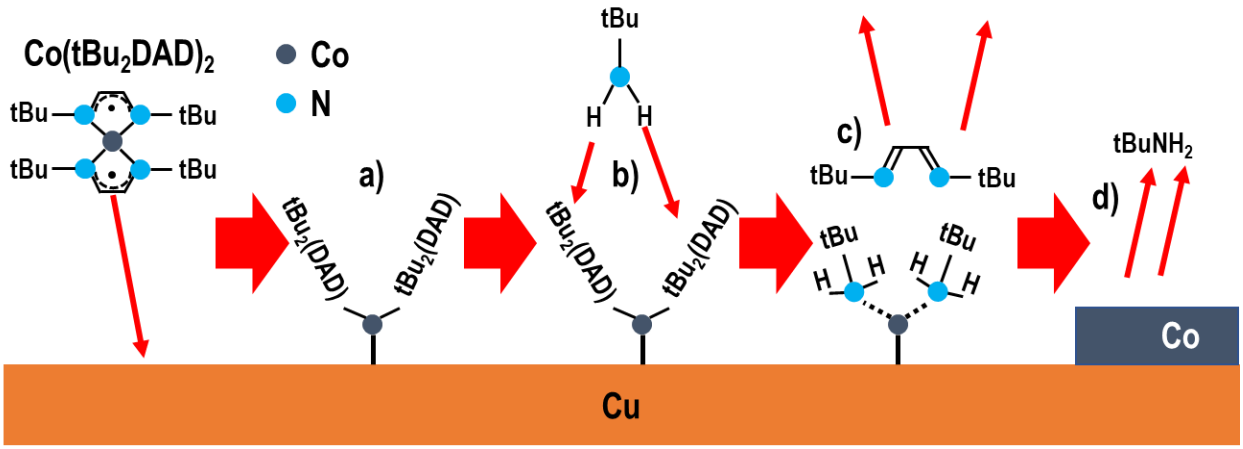

Figure 3.1: Mechanism of $Co(tBu_2DAD)_2$ + TBA ALD at 180 ° C. (a) During the $Co(tBu_2DAD)_2$ cycle, $Co(tBu_2DAD)_2$ chemisorbs to the metal surface, leaving two $tBu_2(DAD)$ ligands bound to Co on surface. (b) During the TBA half-cycle, $tBuNH_2$ exchanges with $tBu_2(DAD)$ ligands. (c) $tBu_2(DAD)$ ligands desorb from surface, leaving behind metal surface with the N atom in $tBuNH_2$ coordinated to Co metal. (d) $tBuNH_2$ subsequently desorbs from the surface, leaving behind Co metal.

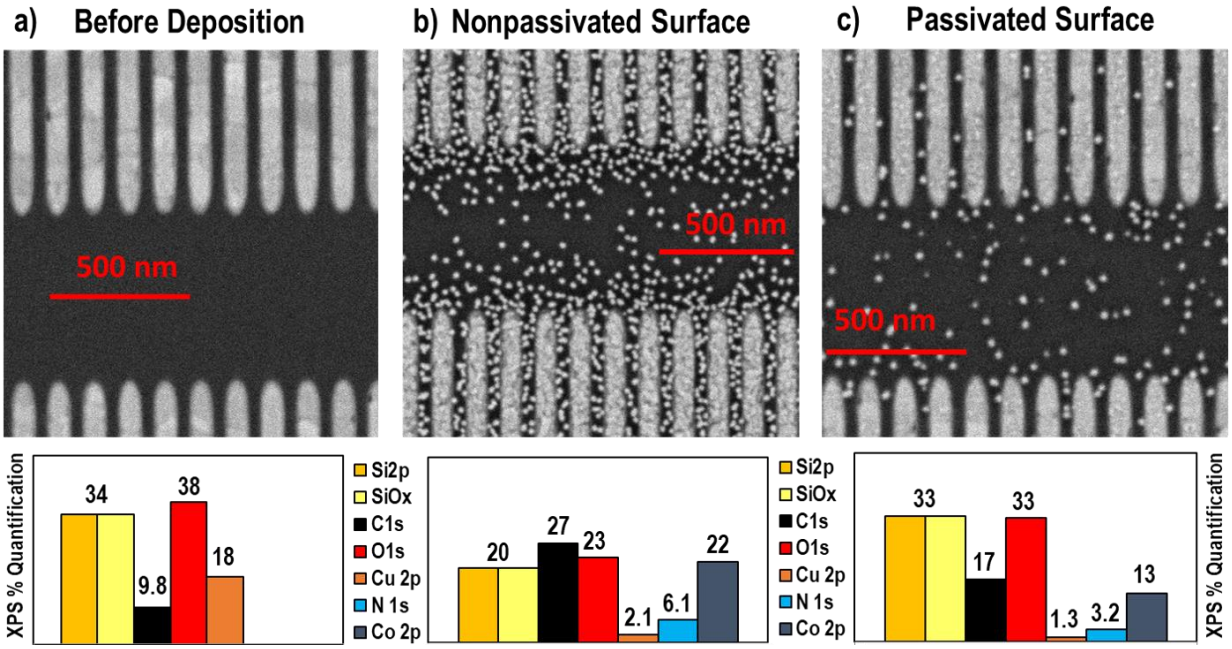

Figure 3.2: SEM of 200 Cycles of Co(tBu_2DAD)$_2$ + TBA at 180°C on a Patterned Cu/SiO_2 structure. (a) Top-down SEM of Cu/SiO_2 pattern showing ~85nm wide Cu (light gray) stripes deposited planar to SiO_2 (dark gray) prior to deposition of Co by ALD. Before deposition, 18% Cu and 34% Si are observed by XPS. (b) After 200 cycles (with 8x pulses of Co and 5 second pump-out times) on the unpassivated sample, unwanted Co nuclei are observed close to the Co/Cu stripes. XPS quantification shows 22% Co and 20% Si on the unpassivated surface, suggesting significant coverage of unwanted nuclei attenuating the Si signal. (c) On a passivated sample, the density of unwanted nuclei is 4x lower and more uniform. XPS quantification shows 13% Co, with 33% Si signal, consistent with less Co coverage over the passivated SiO_2 surface.

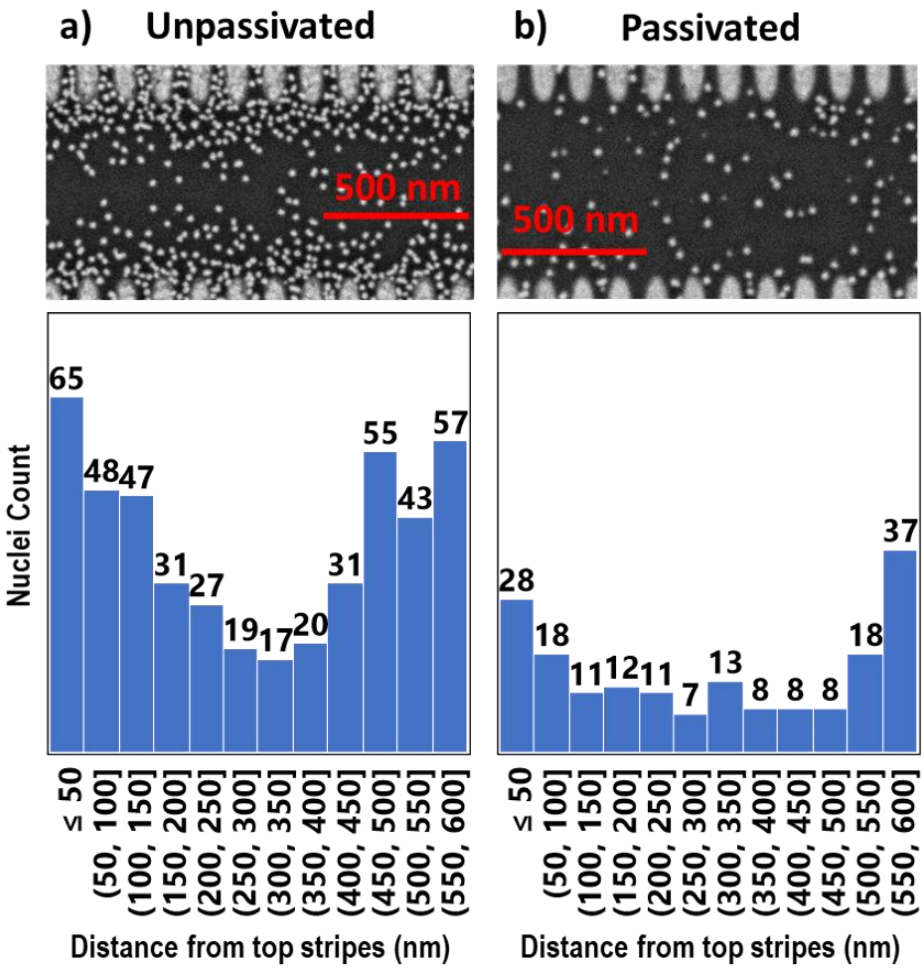

Figure 3.3: SEM and nuclei distance distribution from stripes on passivated vs unpassivated Cu/SiO_2 pattern after Co ALD. Co is light grey and SiO_2 dark grey in SEM images above. Below, nuclei counts are plotted in bins of 50 nm. (a) After 200 cycles on the unpassivated sample, there is a decay in nuclei density until the middle of the alley. (b) On a passivated sample, the density of unwanted nuclei is lower and more uniform across SiO_2.

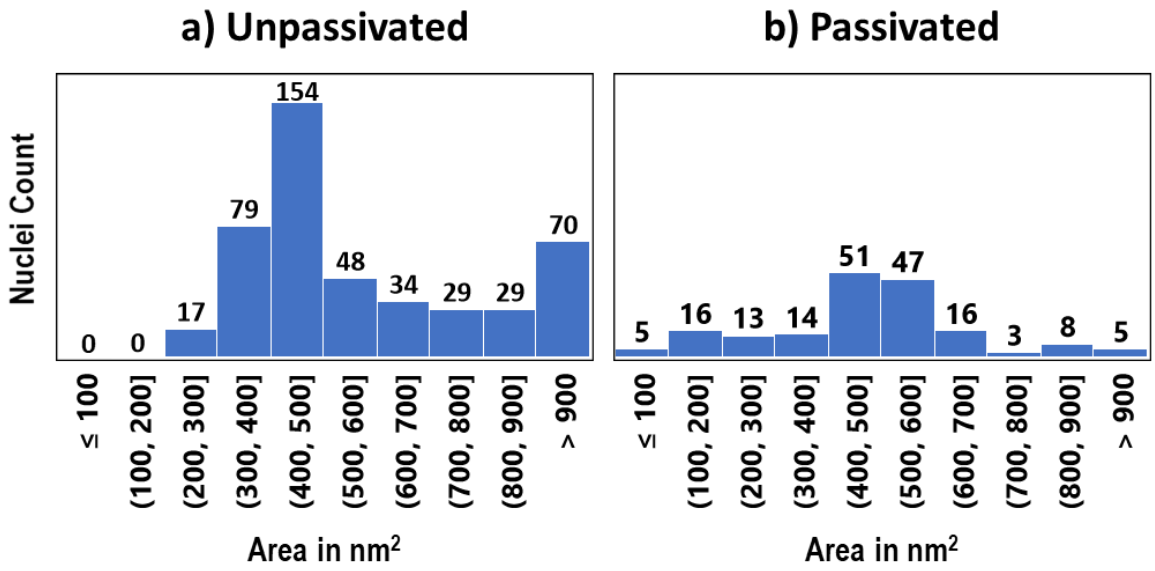

Figure 3.4: Nucleus size distribution on passivated vs unpassivated Cu/SiO_2 striped pattern after Co ALD. Nuclei areas are plotted in bins of 50 nm^2. (a) Unpassivated surface (b) Passivated surface.

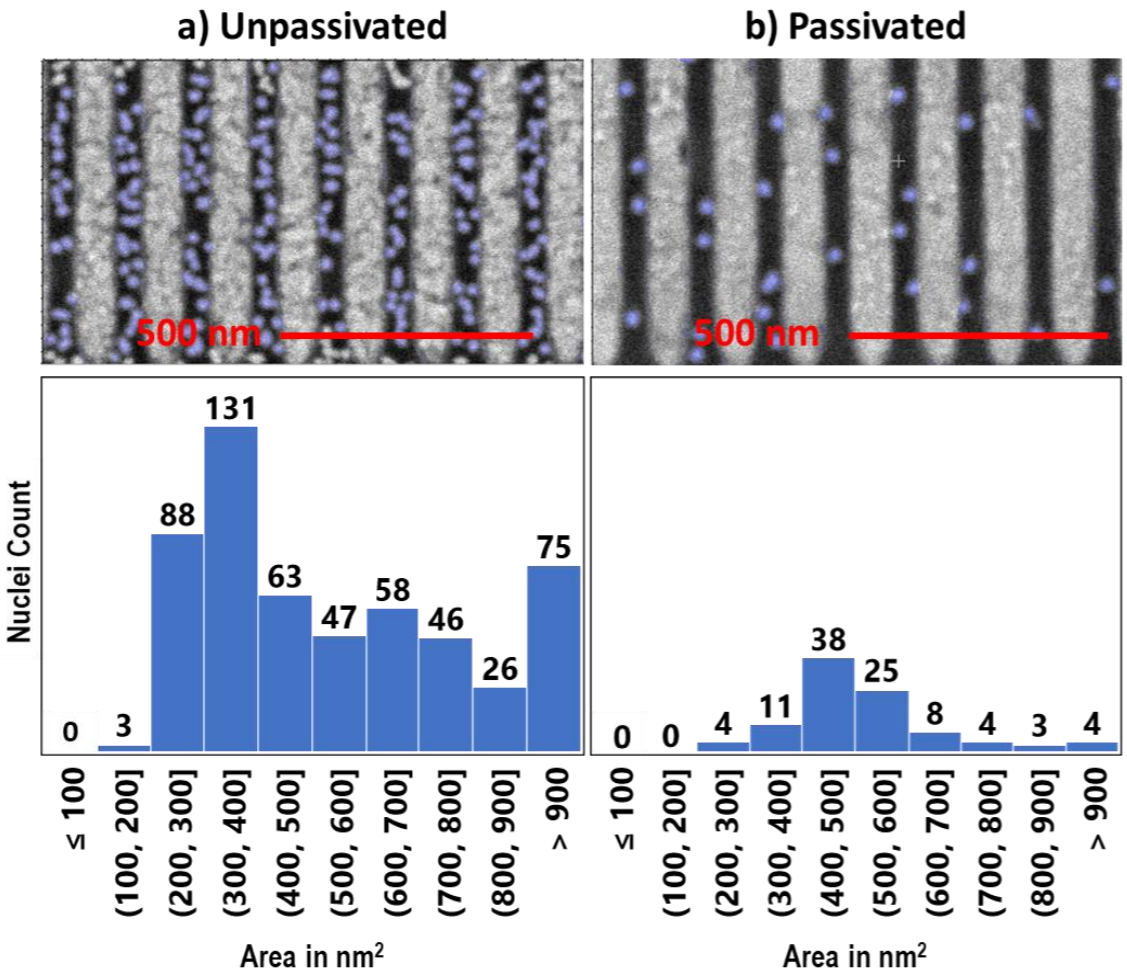

Figure 3.5: Nuclei quantification in confined Cu/SiO_2 pattern of 200 cycles of Co ALD with and without insulator passivation. The Cu stripes are grey and the SiO_2 areas are black. (a) Without passivation, 186 nuclei/μm^2 are observed with an average size of 470 nm^2 and positively-skewed distribution. (b) With passivation, 33 nuclei/μm^2 are observed with a similar distribution centered around a larger mean nucleus size.

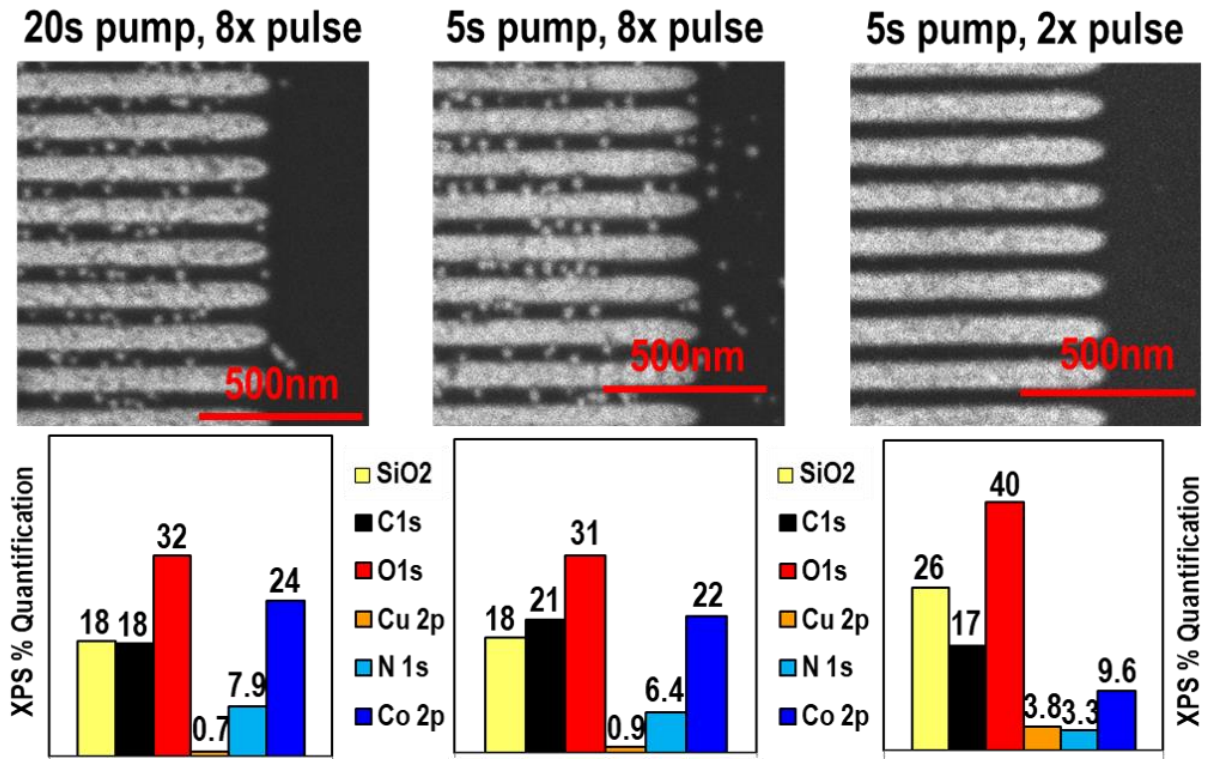

Figure 3.6: Effect of dose and pump-out time during Co ALD on a patterned Cu/SiO_2 sample without insulator passivation. The Cu stripes are grey and the SiO_2 areas are black. Increasing pump-out time has a strong effect on nuclei density in the large open SiO_2, areas but a weak effect on nucleation density on the narrow SiO_2 regions between the metal strips. The dose of $Co(tBu_2DAD)_2$ in each cycle was then reduced by 4x, with near perfect selectivity with 2x pulse and half the growth rate. Raw SEM images and XPS spectra of the above samples are included in Supporting Information as Figs. S13 and S17 for the 8x Co pulse/20s pump-out time condition; S12 and S16 for the 8x Co pulse/5s pump-out time condition; and S18 and S20 for the 2x Co pulse/5s pump-out time condition, respectively.

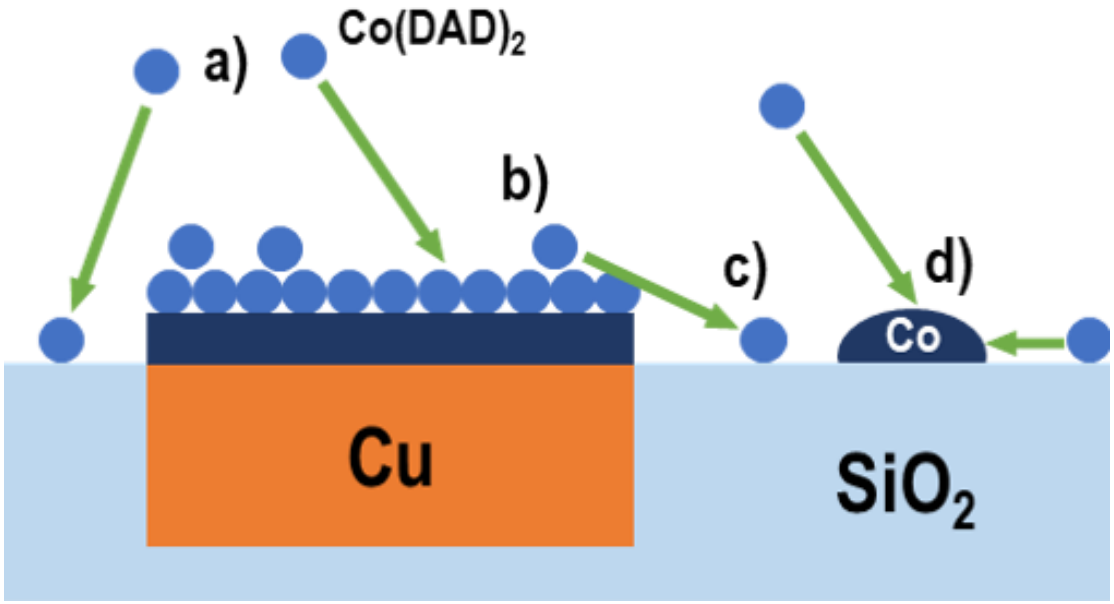

Fig. 3.7: Mechanism of excess $Co(tBu_2DAD)_2$ precursor surface diffusion onto insulator. (a) Dosing of $Co(tBu_2DAD)_2$ precursor onto both metal and insulator surfaces, with precursor binding to metal while only physisorbing on insulator. (b) Saturated metal surface with excess precursor being weakly-bound to surface and free to diffuse. (c) Diffusion of excess precursor off saturated metal surface onto insulator. (d) Co nuclei formed on insulator defects - excess precursor diffusing across the insulator will bind with the nucleus in addition to dosed precursor.

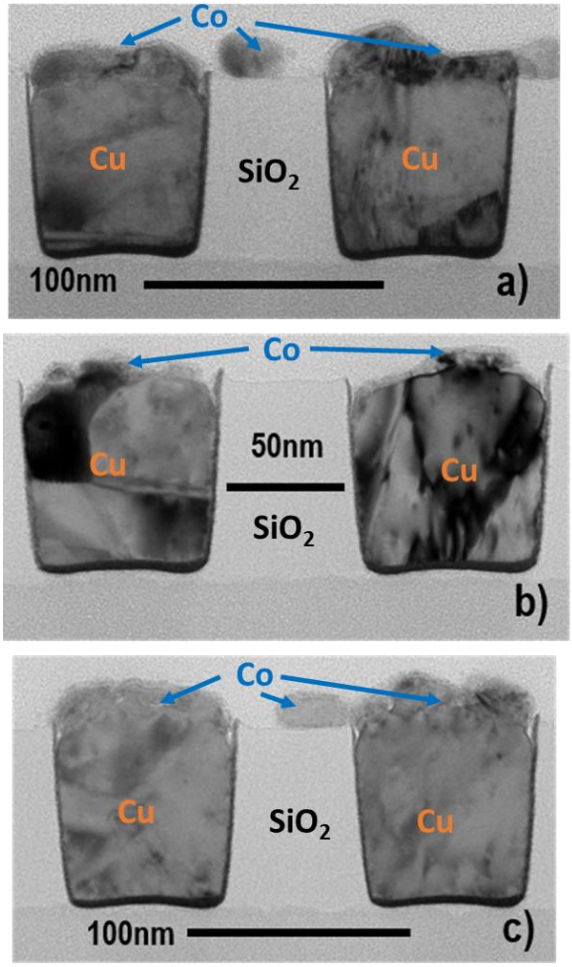

Figure 3.8: TEM of 200 Co ALD cycles with varying pump-out time and dose without passivation. The Cu stripes are dark grey and the SiO_2 areas are white. (a) With 8 pulses of Co precursor per cycle, and 5s pump-out time, unwanted nucleation density is high. (b) Reducing Co pulse count to 2 pulses/cycle with 5 s pump-out time lowers the growth rate (c) Increasing the pump-out time from 5s to 20s for 8 pulses of Co precursor per cycle improves unwanted nucleation density, but higher precursor does not eliminate unwanted nucleation.

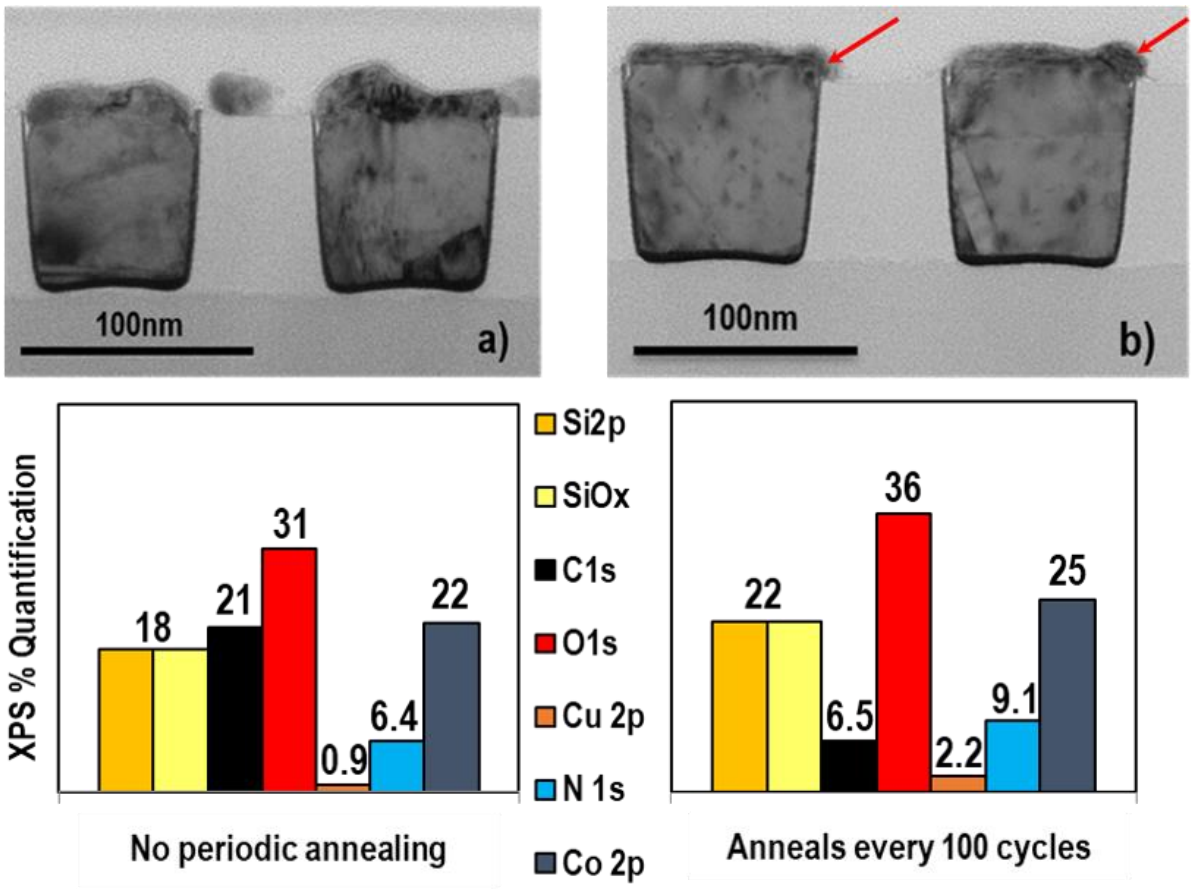

Figure 3.9: TEM and XPS of 200 Co ALD cycles on a Patterned Cu/SiO_2 sample with periodic anneal. TEM of the Cu stripes after deposition with Cu in dark grey and SiO_2 in light grey. Co ALD was performed on an unpassivated surface. 8 pulses of Co precursor were dosed per Co half-cycle, followed by a 5 second pump-out. (a) Without periodic anneal, unwanted nucleation is observed on SiO_2, with the Si signal in XPS being more attenuated than on the annealed sample. (b) After periodic anneals every 100 cycles, a denser film is observed, with the formation of bulges at stripe edges (red arrow) consistent with nanoscale reflow of Co. The periodically-annealed surface exhibited near-perfect selectivity, with no observed nuclei on the insulator (SEM images in Supporting Information Figs. S22 and S23, respectively).

3.7 REFERENCES

[1] D. Gall, *The search for the most conductive metal for narrow interconnect lines*. J. Appl. Phys. 2020. **127**: p. 050901.

[2] J.J Plombon, E. Andideh, V. M. Dubin, and J. Maiz, *Influence of phonon, geometry, impurity, and grain size on Copper line resistivity*. Appl. Phys. Lett., 2006. **89**: p. 113124.

[3] C. C. Yang, P. Flaitz, P. C. Wang, F. Chen, and D. Edelstein, *Characterization of selectively deposited cobalt capping layers: Selectivity and electromigration resistance.* IEEE Electron Device Letters, 2010. **31**: p. 728-730.

[4] R. Carpio and A. Jaworski, *Management of Copper Damascene Plating*. Journal of The Electrochemical Society, 2019. **166**: p. D3072-D3096.

[5] G. Parsons and R. Clark, *Area-Selective Deposition: Fundamentals, Applications, and Future Outlook.* Chem. Mater., 2020. **32**: p. 4920-4953.

[6] I. Zyulkov, M. Krishtab, S. De Gendt, and S. Armini, *Selective Ru ALD as a Catalyst for Sub-Seven-Nanometer Metal Interconnects*. ACS Appl. Mater. Interfaces., 2017. **9**(36): p. 31031–31041.

[7] M. J. Li, M. Breeden, V. Wang, J. Hollin, N. M. K. Linn, C. H. Winter, A. C. Kummel, and M. S. Bakir, *Cu-Cu Bonding Using Selective Cobalt Atomic Layer Deposition for 2.5-D/3-D Chip Integration Technologies*, IEEE Trans. Components, Packaging and Manufacturing Technology, 2020. **10**(12): p. 2125-2128.

[8] T. Elko-Hansen and J. Ekerdt, *Selective Atomic Layer Deposition of Cobalt for Back End of Line.* ECS Trans., 2017. **80**(29): p. 29-37.

[9] J. Kwon, M. Saly, M. Halls, R. Kanjolia, and Y. Chabal, *Substrate Selectivity of (^{t}Bu-Allyl)Co(CO)$_3$ during Thermal Atomic Layer Deposition of Cobalt*. Chem. Mater., 2012. **24**: p. 1025-1030.

[10] J. P. Klesko, M. M. Kerrigan, and C. H. Winter, *Low Temperature Thermal Atomic Layer Deposition of Cobalt Metal Films*. Chem. Mater., 2016. **28**: p. 700-703.

[11] M. Kerrigan, J. Klesko, S. Rupich, C. Dezelah, R. Kanjolla, Y. Chabal, and C. H. Winter, *Substrate selectivity in the low temperature atomic layer deposition of cobalt metal films from bis(1,4-di-tert-butyl-1,3-diazadienyl)cobalt and formic acid.* J. Chem. Phys., 2017. **146**: p. 052813.

[12] S. Wolf, M. Breeden, S. Ueda, J. Woodruff, M. Moinpour, R. Kanjolla, and A. C. Kummel, *The role of oxide formation on insulating versus metallic substrates during Co and Ru selective ALD.* Appl. Surf. Sci., 2019. **510**: p. 144804.

[13] M. M. Kerrigan, J. P. Klesko, and C. H. Winter, *Low Temperature, Selective Atomic Layer Deposition of Cobalt Metal Films Using Bis(1,4-di-tert-butyl-1,3-diazadienyl)cobalt and Alkylamine Precursors*. Chem. Mater., 2017. **29**: p. 7458-7466.

[14] H. Kim, H. B. R. Lee, W. H. Kim, J. W. Lee, J. Kim, and I. Hwang, *The degradation of deposition blocking layer during area selective plasma enhanced atomic layer deposition of cobalt*. J. Korean. Phy. Soc., 2010. **1**(56): p. 104-107.

[15] A. Mackus, M. Merkx, and W. Kessels, *From the Bottom-up: Toward Area-Selective Atomic Layer Deposition with High Selectivity*. Chem. Mater., 2019. **31**: p. 2-12.

[16] J. Soethoudt, F. Grillo, E. A. Marques, J. R. van Ommen, Y. Tomczak, L. Nyns, S. V. Elshocht, and A. Delabie, *Diffusion-mediated growth and size-dependent nanoparticle reactivity during ruthenium atomic layer deposition on dielectric substrates*. Adv. Mater. & Interfaces, 2018. **24**(5): p. 1800870.

[17] F. Grillo, J. A. Moulijn, M. T. Kreutzer, and J. R. van Ommen, *Nanoparticle sintering in atomic layer deposition of supported catalysts: Kinetic modeling of the size distribution*. Catal. Today, 2018. **316**: p. 51-61.

[18] R. Khan, B. Shong, B. G. Ko, J. K. Lee, H. Lee, J. Y. Park, I. L. Oh, S. S. Raya, H. M. Hong, K. B. Chung, E. J. Luber, Y. S. Kim, C. H. Lee, W. H. Kim, and H. B. R. Lee, *Area-selective atomic layer deposition using Si precursors as inhibitors*. Chem. Mater., 2018. **30**: p. 7603-7610.

[19] T. Imada, Y. Nakata, S. Ozaki, Y. Kobayashi, and T. Nakamura, *Systematic investigation of silylation materials for recovery use of low-k material plasma damage*. Jpn. J. Appl. Phys., 2015. **54**: p. 071502.

[20] O. Sneh, and S. M. George, *Thermal Stability of Hydroxyl Groups on a Well-Defined Silica Surface*. J. Phys. Chem., 1995. **99**: p. 4639-4647.

[21] M. D. Abramoff, P. J. Magalhaes, and S. J. Ram, *Image processing with ImageJ*. Biophotonics Intl., 2004. **7**(11): p. 36-42.

[22] Y. Kokaze, S. Kodaira, Y. Endo, J. Hamaguchi, M. Harada, S. Kumamoto, Y. Sakamoto, and Y. Higuchi, *Performance of Integrated Cu Gap-Filling Process with Chemical Vapor Deposition Cobalt Liner*. Jpn. J. Appl. Phys., 2013. **52**: p. 05FA01.

[23] H. Kim, V. Kamineni, M. G. Sung, and C. Park, *Low line resistivity and repeatable metal recess using CVD cobalt reflow*. Patent # US9362377B1 filed 02-27-2015.

[24] T. Nogami, R. Patlolla, J. Kelly, B. Briggs, H. Huang, J. Demarest, J. Li, R. Hengstebeck, X. Zhang, G. Lian, B. Peethala, P. Bhosale, J. Maniscalco, H. Shobha, S. Nguyen, P. McLaughlin, T. Standaert, D. Canaperi, D. Edelstein, and V. Paruchuri, *Cobalt/copper composite interconnects for line resistance reduction in both fine and wide lines*. 2017 IEEE

International Interconnect Technology Conference (IITC). Hsinchu, Taiwan. 2017: p. 1-3.

[25] H. Lee, W. Kim, J. Lee, J. Kim, K. Heo, I. Hwang, Y. Park, S. Hong, and H. Kim, *High Quality Area-Selective Atomic Layer Deposition Co Using Ammonia Gas as a Reactant.* J. Electrochem. Soc. 2010. **157**: p. D10.

Chapter 4

Ruthenium atomic layer deposition with near-bulk resistivity for interconnects

4.1 ABSTRACT

Ruthenium is viewed as a promising alternative to Cu and Co interconnect metals at M0/M1 interconnect layers due to its lower effective resistivity in highly-confined layers and vias, as well as its resistance to diffusion into porous low-k dielectrics and to electromigration. Atomic layer deposition (ALD) of Ru has been reported with a variety of precursors, but the search for a Ru ALD process with a close-to-bulk resistivity is ongoing. In this work, Ru films with close-to-bulk resistivity were deposited using $Ru(CpEt)_2 + O_2$ as well as a two-step ALD process using $Ru(DMBD)(CO)_3$ + TBA (tertiary butyl amine) to nucleate and $Ru(EtCp)_2 + O_2$ to increase film thickness. In-situ X-ray photoelectron spectroscopy (XPS) showed the grains were oxygen free while X-ray diffraction (XRD/XRR) and transmission electron microscopy (TEM) showed grain diameters approaching film thickness with sharp, nearly vertical grain boundaries. The data are consistent with ALD forming an intermediate RuO_2 which facilitates diffusion and no carbon incorporation to form large grains while the high temperature deposition results in an oxygen-free film. The grain structure evolves during growth so that the grain sizes at the top and bottom of the films are nearly identical.

4.2 INTRODUCTION

Due to its low bulk resistivity, copper has been used as the interconnect and via metal of choice in VLSI process nodes since the early 2000s [1] [2]. However, as transistor density continues to increase, via width continues to decrease, and at small dimensions (~<10nm), the mean free path of electrons in Cu is larger than the layer thickness, resulting in increased electron

scattering that contributes to an increase in resistivity [3]. In addition, present Cu interconnects and vias require a thin diffusion barrier layer, typically TiN or TaN which have much higher resistivities than Cu, to prevent migration of Cu into the dielectric layer [4] [5]. Due to this barrier layer, a much higher fraction of the via width is taken up by the barrier in narrower vias, further increasing resistance due to the higher resistivity of the barrier [6]. Ru, with an electron mean free path of 6.6 nm compared with 40 nm for Cu, maintains its bulk resistivity to much narrower via widths due to reduced scattering [7]. In addition, Ru shows higher resistance to electromigration and can potentially be used without a barrier layer, filling the entire via with the lower-resistivity metal and decreasing via resistance [8]. Due to this high electromigration resistance, reduction of the effect of thickness on resistivity compared to Cu, and etching by a non-halogen (oxygen), Ru has been proposed for the emerging semidamascene process, in which a blanket metal film is deposited, holes are etched, and the holes are filled with dielectric followed by CMP [9].

Ru can be deposited in a variety of methods such as DC sputtering [10] or chemical vapor deposition (CVD) [11], but special focus is placed on atomic layer deposition (ALD) for interconnect applications due to its thickness controllability and the potential to exploit differences in surface reactivity for area-selective ALD [12] [13]. Ru thermal ALD has been reported with a variety of Ru(II) based precursors such as $RuCp_2$ [14] and $Ru(EtCp)_2$ [15], as well as zero-valent Ru compounds like EBECHRu [16]. Typically, these reactions are run around 300-360 °C with O_2 as a co-reactant, where combustion reactions with the organic ligands leave behind metallic Ru with resistivities roughly 1.5-2x that of bulk Ru. However, many of these processes also result in long nucleation delays which can result in rough films and reduce controllability [17]. Lower-temperature processes with shorter or zero nucleation delay have also been reported using $Ru(DMBD)(CO)_3$ + tertiary butyl amine (TBA) and other non-oxidizing co-reactants, but these

films result in higher resistivity compared with the high-temperature processes [18].

In this study, the resistivities for ALD Ru films as thin as 12 nm are reported that are close to bulk resistivity. To overcome the slow nucleation of $Ru(EtCp)_2 + O_2$, a two-step ALD was performed in which nucleation was promoted by $Ru(DMBD)(CO)_3$ + TBA, with additional Ru deposited using the $Ru(EtCp)_2 + O_2$ ALD process. The films were characterized using in-situ X-ray photoelectron spectroscopy (XPS) for in-situ chemical analysis. X-ray diffraction and reflectometry (XRD/XRR) to determine film thickness and grain structure, atomic force microscopy (AFM) for film roughness, and scanning electron microscopy (SEM) and transmission electron microscopy (TEM) for film morphology and cross-sectional chemical analysis. The two step ALD process was found to have the lower resistivity associated with the $Ru(EtCp)_2 + O_2$. The ultra-low resistivity films correlate with large grain size consistent with ALD having a surface intermediate (RuO_x) which can readily diffuse on the growth surface to form large grains.

4.3 EXPERIMENTAL METHODOLOGY

In this report, Ru ALD was performed by two processes at high and low temperature. The high temperature process employed $Ru(CpEt)_2$ ("CpEt process", EMD Electronics) with 10% O_2 and 90% He carrier gas as a co-reactant. The low-temperature process employed $Ru(DMBD)(CO)_3$ ("DMBD process", EMD Electronics) with tert-butyl amine (TBA) as co-reactant to avoid any substrate oxidation. Both precursors were heated to allow sufficient vapor pressure, with the $Ru(CpEt)_2$ heated to 80 °C and the $Ru(DMBD)(CO)_3$ heated to 50 °C. Experiments were carried out in a custom-designed multi-chamber (Fig. 4.1) consisting of a load-lock chamber, two cold-wall (~120 °C) deposition chambers to the high and low-temperature processes respectively, and a UHV chamber (base pressure ~10^{-10} Torr) containing the x-ray source and hemispherical

analyzer used for XPS. 2 mm wide sample coupons were used to facilitate simultaneous deposition on multiple substrates. Prior to deposition, samples were degreased using acetone, methanol, and DI water, then dipped in 0.5% HF solution for 30 seconds, followed by a 30 minute 350 °C UHV anneal at ~10^{-8} Torr to remove adventitious carbon using a pyrolytic boron nitride heater.

The deposition chambers were pumped via turbomolecular pump (Pfeiffer TMP-151C for the low-temperature chamber, base pressure ~10^{-6} Torr; Edwards EPX-500NE for the high-temperature chamber, base pressure ~10^{-6} Torr) to minimize background contamination during deposition. Each chamber contained a manipulator arm compatible with the sample holder for XPS and with an embedded cartridge heater external to the chamber to avoid any potential shorting of heater leads during deposition as well as hot wire CVD. The CpEt process was performed at 330-360 °C deposition temperature at a pressure of ~1 Torr, while the DMBD process was performed at 160-180 °C at a pressure of ~1 Torr. To determine if substrate selectivity was present, several substrates including SiO_2, HF-cleaned Si, low-k dielectric (SiCOH), Cu, and W substrates were used. After deposition, samples were transferred *in-situ* to the attached UHV chamber for XPS. A monochromatic XM1000 Mk. II/SPHERA system (Scienta Omicron) was used to collect XPS spectra with an Al kα source at 1486.7 eV at an angle of 60° with respect to the sample surface normal. An analyzer pass energy of 50 eV and linewidth of 0.1 eV were used, and quantification was performed using CASA XPS 2.3 software with raw peak areas corrected using the Scofield relative sensitivity factors and Shirley background subtraction [19]. Due to the overlap of the C1s and Ru $3d_{3/5}$ peak positions, quantification of C is complicated by the need to deconvolute the two signals, with the difference in relative sensitivity factors between Ru and C resulting in large uncertainties. Morgan [20] employed an asymmetric peak fit with empirically determined parameters to provide a closer fit for Ru $3d_{3/5}$, but the lack of an in-situ ion gun for surface

contamination sputtering before XPS prevents the determination of these parameters on a known-pure Ru surface.

After deposition and in-situ analysis, samples were removed and 4-point-probe (Ossila Four-point-probe System, Ossila, Ltd.) measurements were performed on Ru films of 6 mm x 2 mm with a probe spacing of 1.27 mm, corresponding to a geometric sheet resistance correction factor of 0.34 to account for the narrow sample dimensions [21]. Resistivity measurements were also independently performed using a Jandel linear four-point probe with 1 mm inter-probe spacings and a corresponding geometric correction factor of 0.4297 to convert the obtained resistance values to sheet resistance. XRD measurements were performed on the films to determine grain orientation and size using the Scherrer approximation [22] [23] [24]. X-ray reflectivity (XRR) analyses were performed using a PANalytical X'pert PRO MPD system with a Cu source and a parabolic mirror yielding a parallel beam with a <0.055° divergence. ω-2θ scans were performed at shallow angles, 0.2–5.0° and the resulting data comprising of thickness oscillations was fit to the Parratt formalism for reflectivity using the PANalytical X'pert Reflectivity software. The fitting yields the layer thickness and density [25] [26]. Hayes *et. al.* showed that a post-deposition forming gas anneal (FGA) can be used to further improve the resistivity of the film [27], so these measurements were repeated for samples after a 30 minute 450 °C FGA, and SEM and AFM were used to inspect the morphology of the surface. Finally, TEM of the deposited Ru films on SiO_2, W, and Cu was performed to obtain cross-sectional chemical profiles by energy-dispersive spectroscopy (EDS).

4.4 RESULTS & DISCUSSION

4.4.1 High-temperature Ru ALD with $Ru(CpEt)_2 + O_2$

A study was first performed using the cyclopentadienyl-based Ru precursor, $Ru(CpEt)_2$ with O_2 as a co-reactant. SiO_2, Si, and low-k dielectric were first loaded and annealed in UHV as described above, followed by 100 cycles of Ru ALD by alternating pulses of $Ru(CpEt)_2$ and O_2. The maximum pressure in the chamber was limited to maintain high pumping speed and protect the turbomolecular pump; this was accomplished by using multiple doses during each half-cycle, with chamber pressure during dosing rising to around 10 mTorr for $Ru(CpEt)_2$ and ~1 Torr O_2/He (O_2 partial pressure ~100 mTorr). Deposition was carried out at 330 °C with pump-out times between half-cycles of 50 seconds for $Ru(CpEt)_2$ and 30 seconds for O_2 to give enough time for precursor to desorb from the walls after dosing, avoiding any potential gas-phase reactions leading to CVD-like growth.

Fig. 4.2 illustrates a step-by-step comparison of the surface elemental composition as measured by XPS. Increments of 100 ALD cycles were performed, with significant nucleation delay occurring on all three samples. Previous studies with the $Ru(CpEt)_2$ precursor have noted a high nucleation delay, typical of other high-temperature O_2-based processes [15]. Comparison of the substrates showed that this nucleation delay was significantly longer on the Si substrate than on SiO_2 or the low-k dielectric. On SiO_2 after 300 ALD cycles, the Si XPS signal decreased to 6%; using the Thickogram method of thickness estimation [28], assuming a uniformly thick film, this corresponded to a Ru layer 1.7 nm thick. After 500 total cycles on SiO_2, the substrate signal is sub-1%, implying a film thicker than 3 nm.

On HF-cleaned Si, nucleation was still poor after 500 cycles, with sub-monolayer coverage persisting even after 500 cycles. On the low-k dielectric, an intermediate nucleation delay was

observed, with a near-monolayer (~0.3 nm) coverage after 400 cycles. Yim *et. al.* proposed that nucleation of Ru is enhanced by the presence of reactive hydroxyl groups on the surface, and these results were consistent with only a trace amount of hydroxyl groups on the low-k SiCOH substrate as well as an even lower density of hydroxyl groups on HF-cleaned Si. [17].

After the nucleation study, an additional 500 cycles of Ru were deposited to provide a film thick enough for a bulk resistivity measurement. Fig. 4.3a) shows the XPS quantification of the resulting 1000 cycle process on SiO_2, Si, and low-k dielectric. All three substrates were fully attenuated in XPS, consistent with a continuous Ru film >5nm thick, with oxygen levels remaining around the noise floor (<1%). After deposition, four-point-probe measurements resulted in a sheet resistance of 1.2 Ω/□ on SiO_2, corresponding to a resistivity of 6.5±0.4 μΩ·cm. The latter is obtained using a thickness of 53±3 nm, determined from XRR measurements shown in Fig. 4.3d). The XRR fitting also provides a value for the surface roughness of 3.6±0.5 nm, in reasonable agreement with the AFM analysis presented below. Fig. 4.3b) shows the XRD pattern of the Ru film deposited on SiO_2 with distinct Ru (100), (002), and (101) peaks, consistent with the formation of a polycrystalline film with grain sizes of roughly 27 nm for the (002) orientation. It is noted that typical reported values of Ru bulk resistivity vary, but range from 7.1-7.8 μΩ·cm to values as low as 5.8 μΩ·cm for electron transport in the hexagonal axis. [25] [29]. As the (002) plane is perpendicular to the hexagonal axis, this is consistent with the observed resistivity value. This has the potential to be useful for the emerging semi-damascene process as the lowest resistivity transport direction is the vertical direction of the via [9]. Fig. 4.3c) shows an AFM image over a 2x2 μm region on the SiO_2 film showing a root-mean-square roughness of 2.4 nm which is small compared to the thickness of the film.

After the full 1000 cycles, a C content of 20-22% was observed on all three substrates; note

this is just surface carbon from residual ligands not bulk carbon. Fig. 4.4 shows the high-resolution scan of the binding energies corresponding to Ru 3d for Ru and C 1s for C during the saturation study and after 1000 cycles. Fig. 4.4 shows the XPS spectra for the first 500 cycles on SiO_2. After the initial UHV anneal, a small peak at 285.3 eV corresponding to adventitious C remaining after anneal was present. Depositing 100 cycles of the $Ru(CpEt)_2 + O_2$ process at 330 °C, a split-peak corresponding to Ru 3d appeared, with the $3d_{5/2}$ spin orbit split centered at 280.5 eV. With an additional 100 cycles, the Ru 3d peak further shifted to 280.9 eV, corresponding to the reported value for RuO_2 [20]. After 300 total cycles, the peak shifted back to 279.8 eV, the value reported for metallic Ru, and remained at 279.8 eV after 1000 total cycles deposited. As mentioned above, precise C quantification with Ru present was complicated by the direct overlap between the C1s and Ru $3d_{3/2}$ peaks, with the Ru peak having a significantly higher relative sensitivity factor. Small changes in the measured C 1s fit on the high-energy shoulder of the Ru $3d_{3/2}$ peak can significantly change the calculated amount of carbon. Therefore, cross section TEM-EDX is used below to better quantify the carbon in the Ru film.

4.4.2 Effect of substrate during high-temperature Ru ALD

As the intended purpose of Ru metallization is to serve as a low resistance via between interconnect layers, compatibility with other used metals is key. Fig. 4.5 demonstrates the deposition of the low-resistance Ru film using the CpEt process on SiO_2, Cu, and W substrates. After the first 200 cycles of Ru ALD at 340 °C, the W substrate was fully attenuated, compared with a 4% Si signal consistent with a ~2 nm film thickness on SiO_2. However, on the Cu substrate, growth appeared to be significantly slower, with an estimated 0.3 nm film thickness using the Thickogram method [28]. An additional 300 cycles deposited resulted in complete coverage on

both SiO_2 and W, but significant Cu signal remains, with an estimated thickness of 0.5 nm assuming a uniform thin film. After deposition, the Ru film thickness on SiO_2 was measured by XRR to be 30 nm with a sheet resistance of 2.7 Ω/□, for a resistivity of 8.1 μΩ·cm, slightly higher than the bulk value of Ru.

Next, a TEM cross-section of each of the samples deposited above was performed. In Fig. 4.6a) a Ru film with columnar grains was observed on the SiO_2 substrate. By EDS, the average C content in the Ru film was estimated at 19%. Previous studies of Ru-C films showed a film resistivity of 110 μΩ·cm with a similar C concentration; as the Ru film deposited on SiO_2 had a resistivity near the bulk level, this C content is likely to be overestimated [30]. XRD performed on the Ru film deposited on the SiO_2 substrate showed an average crystallite size of 23 nm for the (002) orientation and 20 nm for the (101) orientation using the Scherrer approximation for crystallite size.

To estimate the degree to which grains are arranged vertically, a 400nm long section of the film by TEM was visually inspected to count the number of grains, as well as their average lateral grain size (Fig. 4.6e). To estimate the degree to which the columnar grains are continuous to the top of the film, a count of grain boundaries was done at 5 nm, 15 nm, and 25 nm from the Ru/SiO_2 interface, showing a count of 23, 21, and 19 boundaries respectively. As the number of grain boundaries remains similar throughout the depth of the film, columnar grains are observed. Damayanti *et. al.* demonstrated the deposition of Ru films by DC sputtering at room temperature having columnar grains of around 5 nm width. After post-deposition annealing at 350 C for 30 minutes, these grains increase in size to 10-15 nm [31]. Comparison of this result with the ALD-deposited Ru films in this work, the grain sizes during ALD are around 2x larger. As the anneal of the DC sputtered Ru films was carried out for 30 minutes compared with the multiple-hour-long

high-temperature ALD processes, this result is consistent with the increased length of time at temperature during ALD encouraging larger grain growth. Estimation of the TEM grain sizes of the ALD Ru film showed an average grain size of 19 nm, compared with the 23 nm estimate by XRD for the (002) oriented grains. As this is smaller than the mean grain size determined by the Scherrer approximation with XRD, the discrepancy may be due to the lamella thickness including multiple grains, complicating the identification of grains by visual inspection.

TEM of the Ru film deposited on W shown in Fig. 4.6b) was similar in morphology to the film deposited on SiO_2, with a lighter layer visible below the Ru film. XPS of the pre-deposition substrate shows significant O content, implying this layer consists of WO_x (x=2.5-3) native oxide instead of metallic W [32]. W native oxide is known to be etched by SF_6 or CF_4 plasma etchants; as no *in-situ* plasma etch was available, the pre-deposition HF clean was insufficient to remove the native oxide [33]. TEM of the Ru film deposited on Cu (Fig. 4.6c), however, showed significant intermixing of the Cu into Ru by TEM-EDS cross-section (Fig. 4.6d), as well as delamination from the Cu surface and void formation towards the top of the film. One hypothesis for this is the O_2-based process formed an oxide on the Cu surface before Ru nucleation has completely covered the substrate, inhibiting growth and resulting in poor film adhesion.

To test this hypothesis, a 4 nm thick seed layer of Ru was first deposited on SiO_2 and Cu surfaces by DC sputtering (Denton Vacuum) at 100 W, 2 mTorr, and 25 ^oC substrate temperature, followed by 300 cycles of Ru ALD at 360 °C with the $Ru(CpEt)_2 + O_2$ process. (see diagrams of structures in Fig 4.7a and 4.7b). Both substrates were Si (100) with a 300 nm thermal SiO_2 layer, with the Ru PVD seed layer on the PVD Cu surface deposited by DC sputtering at 200 W, 2.5 mTorr, and 25 ^oC substrate temperature.

Fig. 4.7a) and 4.7b) also show top-down SEM images of the film after Ru ALD on the a)

PVD Ru/SiO_2 and the b) PVD Ru/PVD Cu/SiO_2 surfaces. Note that, for the PVD Ru/PVD Cu/SiO_2 sample, the Ru and Cu depositions were performed in the same sputter tool without a vacuum break to minimize any CuO_x formation. The ALD Ru film with PVD Ru seed layer on SiO_2 appeared uniform, without pinhole formation, while the Ru seed layer on PVD Cu/SiO_2 showed voids in the Ru film. Comparison of this result with XPS is consistent with these voids being the underlying Cu surface. It was hypothesized that this is due to film de-wetting as a result of the difference in surface free energies of Ru (3.0 J/m^2) and Cu (1.8 J/m^2). To test this hypothesis, a sample was prepared with PVD W/SiO_2 (diagram top of Fig. 7c) due to its similar surface free energy (3.2 J/m^2) to Ru [34]. 600 cycles of ALD Ru were deposited via the CpEt process at 360 ^oC on the PVD W/SiO_2 substrate, and SEM of the ALD Ru layer showed a similar morphology to the ALD Ru film deposited on the PVD Ru/SiO_2 layer, consistent with the surface free energy mismatch between Cu and Ru being the driving force for the formation of these voids.

4.4.3 Low-temperature Ru ALD with $Ru(DMBD)(CO)_3$ + TBA

A study was performed to see if the de-wetting of ALD Ru from Cu could be bypassed by first depositing an Ru film with a low-temperature ALD process. This low temperature process has a second advantage even for deposition on SiO_2 and W. As previously reported, the $Ru(DMBD)(CO)_3$ + TBA process has zero nucleation delay even at deposition temperatures as low as 160 °C [18] [35]. Deposition was performed at a temperature of 150 to 160 °C through a turbomolecular pump for 50 ms at 100 mTorr during dosing of $Ru(DMBD)(CO)_3$ and 15 ms at 1 Torr while dosing TBA. Fig. 4.8 shows XPS quantification for the deposition of Ru using the Ru-DMBD process at 150 °C after the first 100 cycles and after an additional 400 cycles for a total of 500 cycles deposited. On SiO_2 and Cu, the substrate was near-fully attenuated after the first 100

cycles, while SiCOH had a substrate attenuation consistent with sub-monolayer (~0.2 nm) coverage of Ru. After an additional 400 cycles, Cu and SiO_2 were fully buried, but some SiCOH substrate signal remained consistent with ~2 nm film thickness. XRR measurement of the film deposited on SiO_2 showed a film thickness of 23 nm and density of 7.3 g/cm^3, with a sheet resistance of 79 Ω/□ for a resistivity of ~180 μΩ·cm. XRD showed no clear crystalline peaks, consistent with the observed high level of C in the film and the measured high resistivity. A 450 °C forming gas anneal was then performed for 30 minutes, after which a sheet resistance of 11 Ω/□ was measured. Thickness of the post-anneal film on SiO_2 as measured by XRR was 12 nm and density of 11.9 g/cm^3, consistent with a resistivity of 12.5 μΩ·cm. XRD of the post FGA film showed the presence of (002) and (101) grain orientations, with Scherrer-equation derived grain sizes of 11 and 12 nm respectively. As shown below, this resistivity can be brought close to bulk by combining the $Ru(DMBD)(CO)_3$ + TBA ALD with subsequent $Ru(CpEt)_2$ + O_2 ALD.

4.4.4 Bi-layer Ru ALD Process with $Ru(CpEt)_2$ and $Ru(DMBD)(CO)_3$

Due to the surface de-wetting issue with the high temperature Ru ALD process, it was hypothesized that first depositing a sufficiently thick layer of Ru using the low-temperature Ru-DMBD process could act as a seed layer for the subsequent low-resistivity Ru-CpEt process. As a high level of C in the film along with a low film density were present after the DMBD process, an *ex-situ* 30 minute 450 °C forming gas anneal was first performed on the seed layer prior to deposition of Ru with the high-temperature CpEt process. This also avoided stress in the films from the densification of the DMBD seed layer while depositing low-resistivity Ru by the CpEt process. Fig. 4.9a) shows the XPS data after 500 cycles of the Ru-DMBD process, *ex-situ* FGA, and the subsequent deposition of 300 ALD cycles of Ru by the CpEt process on SiO_2 and Cu. After

the DMBD process, both substrates were near-fully attenuated. After the FGA, the apparent thickness of the Ru layer decreased from 2 nm to 0.4 nm on SiO_2, and from 1.4nm to 0.7 nm on Cu. After 300 cycles of the CpEt process, the SiO_2 substrate was again fully attenuated, but the Cu remained visible.

After deposition, the film thickness on SiO_2 was measured by XRR as 15.4 nm with a sheet resistivity of 6.5 Ω/□, corresponding to a film resistivity of 10 μΩ·cm, likely due to the higher resistivity of the DMBD-deposited Ru even after FGA. To further decrease the film resistivity, an additional 30 min 450 °C FGA was performed, decreasing the film resistivity to 8.2 μΩ·cm, a value 10% above that of bulk Ru. Fig. 4.9(b) shows both SEM images and AFM images of the film on SiO_2 and Cu, where a smooth continuous film of sub-nanometer roughness was observed on SiO_2. It is hypothesized that the post CpEt process induced the film from the DMBD process to adopt the favorable grain structure of the CpEt process. However, on Cu, the formation of voids in the film was again observed, with the addition of smaller pits likely due to the de-wetting of the film during the ex-situ FGA. AFM roughness of the Ru film on Cu was 2x that of the film on SiO_2 over a 2x2 μm region.

Fig. 4.10a) shows an XRD scan of the Ru film deposited after a seed layer of the DMBD process at 160 °C, followed by an ex-situ FGA and afterward, the CpEt process at 360 °C. No post-deposition anneal was performed, and a sheet resistance of 3.5 Ω/□ was obtained. By XRD, intensities of both (002) and (101)-oriented grains were observed to be similar, with estimated grain sizes of 15 and 19 nm respectively.

TEM was performed on the bi-layer samples to probe the chemical makeup and grain structure of the film bulk with and without a post CpEt forming gas anneal. In Figs. 4.10b) and c) TEM of the film showed a 23 nm thick Ru film devoid of O, with an average bulk C concentration

of 4.8% in the film compared with the value of surface carbon measured during XPS of 20%, highlighting the difficulty of obtaining an accurate fit for C 1s. Given the thickness measured by TEM and the measured sheet resistance, a resistivity value of 8.2 μΩ·cm was measured. In Fig. 4.10d-e), this deposition was repeated with a post-CpEt process FGA for 30 minutes at 450 °C. Fig. 4.10d) shows a clear difference in intensities between the (002) and (101) peaks, with grain sizes estimated at 19 and 23nm respectively. Film thickness as measured by XRR was 23 nm, with a sheet resistance measured as 3.0 Ω/□, implying a resistivity of 6.9 μΩ·cm. Fig. 10e) contains a EDX line-trace of the film, showing zero O content in the film and C content at an average 2.4% in the film; since the film resistivity is very low, it is hypothesized this carbon is due to contamination during sample preparation of the thin lamella. The data is consistent with CpEt ALD process inducing the film from the DMBD process to adopt the favorable grain structure of the CpEt process as shown by the lack of any boundary in TEM between the DMBD and the CpEt layers and the large grains spanning the full thickness of the film.

4.5 CONCLUSION

Deposition of Ru films by ALD with resistivities close to the bulk value has been demonstrated by the use of a three-step process with a seed layer deposited by an oxygen-free low-temperature Ru ALD process using DMBD and TBA, followed by a post-deposition forming gas anneal of the seed layer, and a thick, high temperature deposition to form large grains with the $Ru(CpEt)_2 + O_2$ process. Near-bulk resistivities have been obtained for 30 nm films deposited by the bi-layer process, with XRD confirming the presence of grains of a size close to the film thickness. Cross-sectional TEM shows the width of grains throughout the film thickness remaining constant within 20%, consistent with continuous grains spanning the full thickness of the film.

Comparison of this result with the measured low sheet resistance is consistent with the underlying Ru seed layer adopting the larger grain structure of the low-resistivity O_2-based Ru ALD process after forming gas anneal, forming continuous large grains spanning the full film thickness, improving out-of-plane electron transport with a corresponding decrease in resistivity. With optimized ALD conditions, these low-resistivity processes have the potential to allow for viable Ru films in barrierless via-fills as well as for the interconnect layers themselves at the M0/M1 level for metals with surface-free-energies close to that of the Ru such as W. However, further work remains to integrate the Ru films on top of existing Cu films without voids or impurities.

4.6 ACKNOWLEDGEMENTS

This work was supported in part by the Applications and Systems-Driven Center for Energy Efficient Integrated Nano Technologies (ASCENT), one of six centers in the Joint University Microelectronics Program (JUMP), an SRC program sponsored by the Defense Advanced Research Program Agency (DARPA). The authors would also like to gratefully acknowledge support from Applied Materials, Rasirc, and EMD Electronics. This work was also performed in part at the San Diego Nanotechnology Infrastructure (SDNI) of UCSD, a member of the National Nanotechnology Coordinated Infrastructure, which is supported by the National Science Foundation (Grant ECCS-1542148).

Chapter 4, in full, is currently being prepared for submission for publication of the material, and reprinted with permission from M. Breeden, V. Wang, R. Kanjolia, M. Moinpour, D. Moser, J. Woodruff, H. Simka, A. Jog, D. Gall, and A. C. Kummel. *Ruthenium atomic layer deposition with near-bulk resistivity for interconnects*. (manuscript in preparation). The dissertation author was the primary investigator and author of this paper.

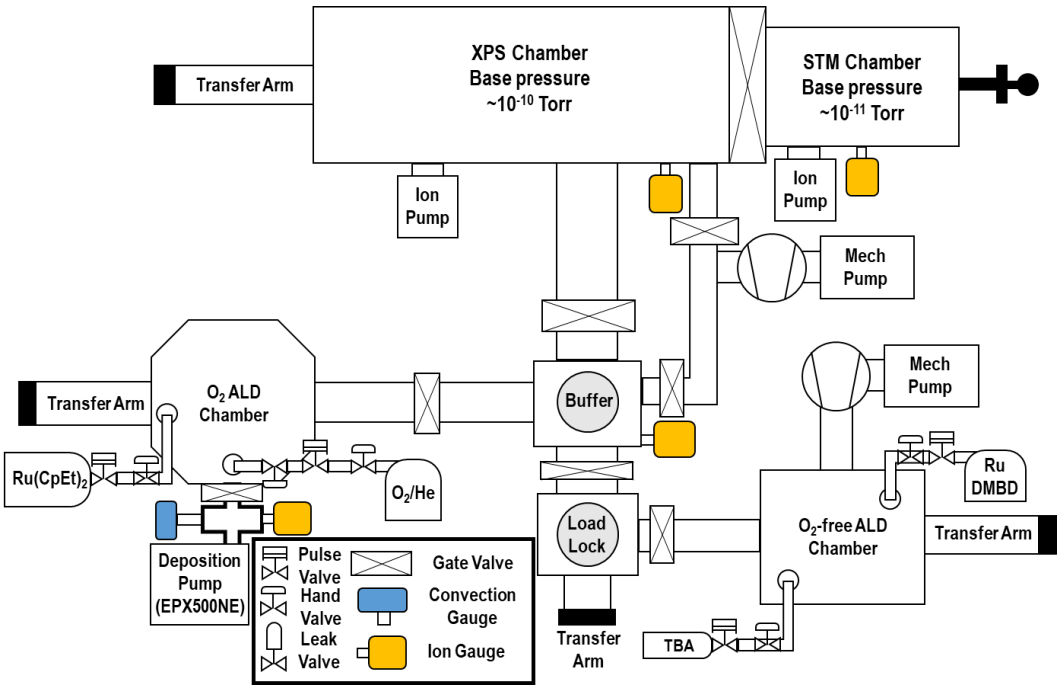

Figure 4.1: Chamber Schematic. XPS system with an attached load-lock and ALD chamber allows for in situ chemical composition characterization without exposure to oxygen.

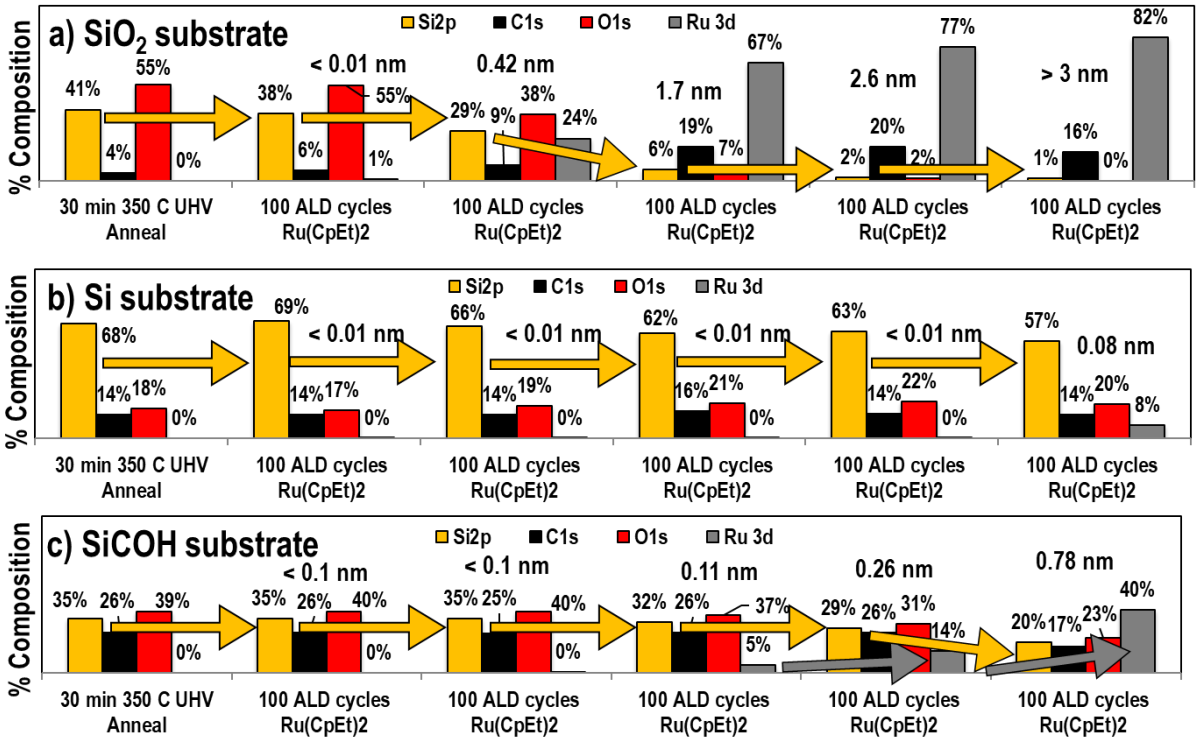

Figure 4.2: XPS of Ru ALD nucleation at 330 °C with $Ru(CpEt)_2$ + O_2 on SiO_2, Si, and SiCOH. On all three substrates, a significant nucleation delay was observed. a) On the SiO_2 substrate, a nucleation delay of ~200 cycles was observed. b) On Si substrate, growth was inhibited for the first 500 cycles, with sub-monolayer coverage persisting even after 500 cycles of deposition. c) On low-k dielectric, a nucleation delay of ~300 cycles was observed.

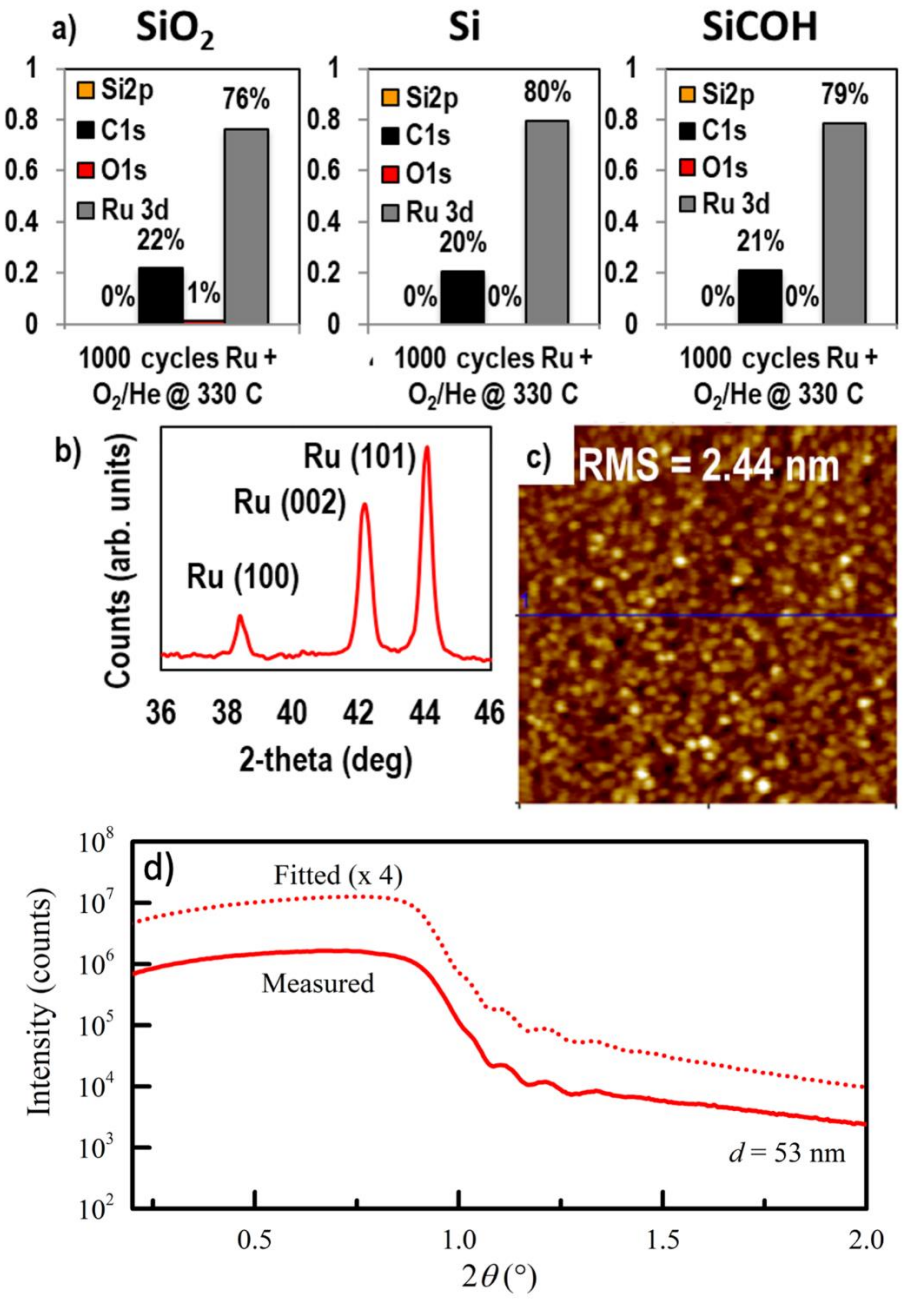

Figure 4.3: XPS/XRD/AFM of Ru ALD after 1000 cycles at 330 °C with $Ru(CpEt)_2$ + O_2 on SiO_2, Si, and SiCOH. a) After 1000 cycles, all three substrates are fully covered by the Ru film, with oxygen levels below the noise floor. b) XRD shows relative intensities of the (002) and (101) peaks are similar. c) AFM over a 2x2 µm region shows a film RMS roughness of ~2.4 nm. d) Measured XRR intensity and curve fit, indicating a layer thickness d = 53 nm.

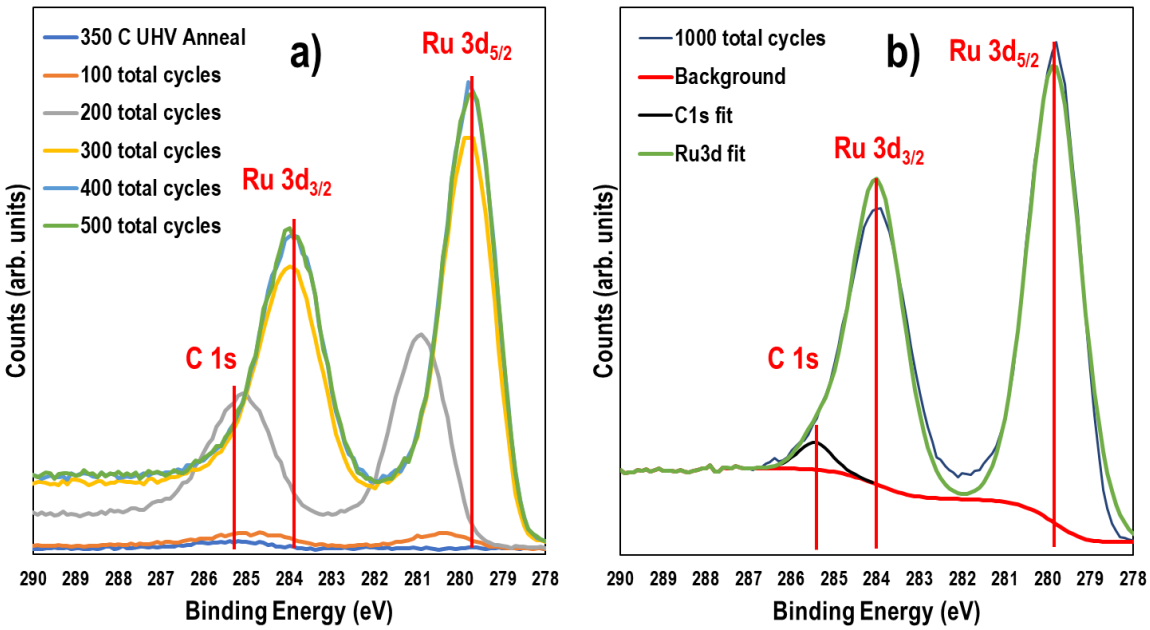

Figure 4.4: High-resolution XPS of Ru ALD nucleation at 330 °C with $Ru(CpEt)_2$ + O_2 on SiO_2. After the first hundred cycles, Ru 3d peaks begin to appear, with the shoulder of the higher energy spin-orbit split overlapping C1s. With the addition of an additional 100 cycles, the Ru $3d_{5/2}$ peak shifts to 280.9 eV, consistent with RuO_x formation, but after a total of 300 cycles, the location of the Ru $3d_{5/2}$ peak returns to 279.8 eV and remains after additional cycles, consistent with metallic Ru. b) The peak fitting after 1000 cycles is shown, with the C shoulder centered at 285.7 eV. Note that due to the difference in relative sensitivity factors between Ru 3d and C 1s, the C peak represents 20% composition.

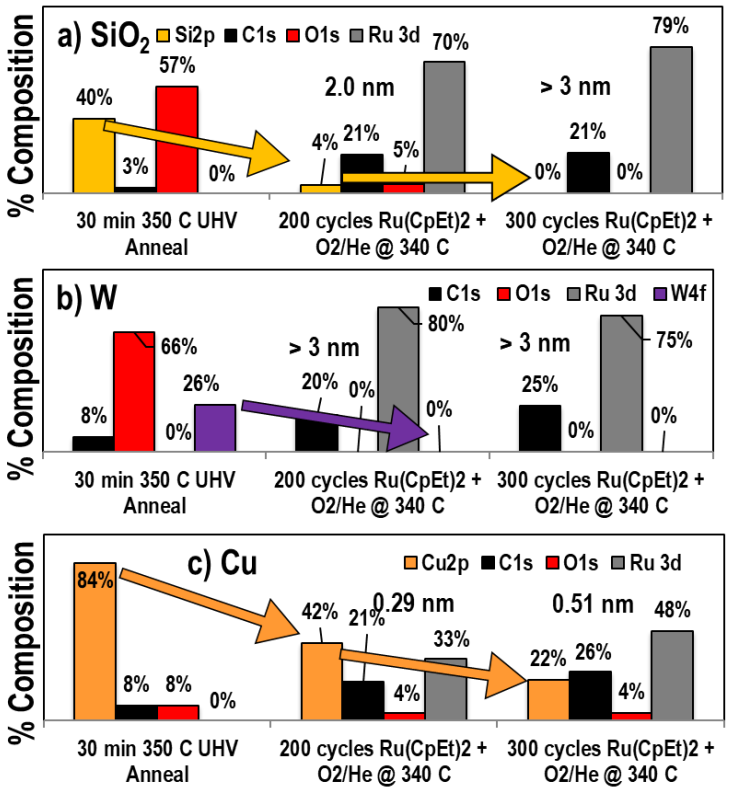

Figure 4.5: XPS of Ru ALD at 340 °C with $Ru(CpEt)_2 + O_2$ on SiO_2, W, and Cu. a) Substrate near-fully attenuated after first 200 cycles, and fully attenuated after 500 total cycles. b) Substrate is fully attenuated after first 200 cycles. c) Substrate remains visible in XPS even after 500 cycles.

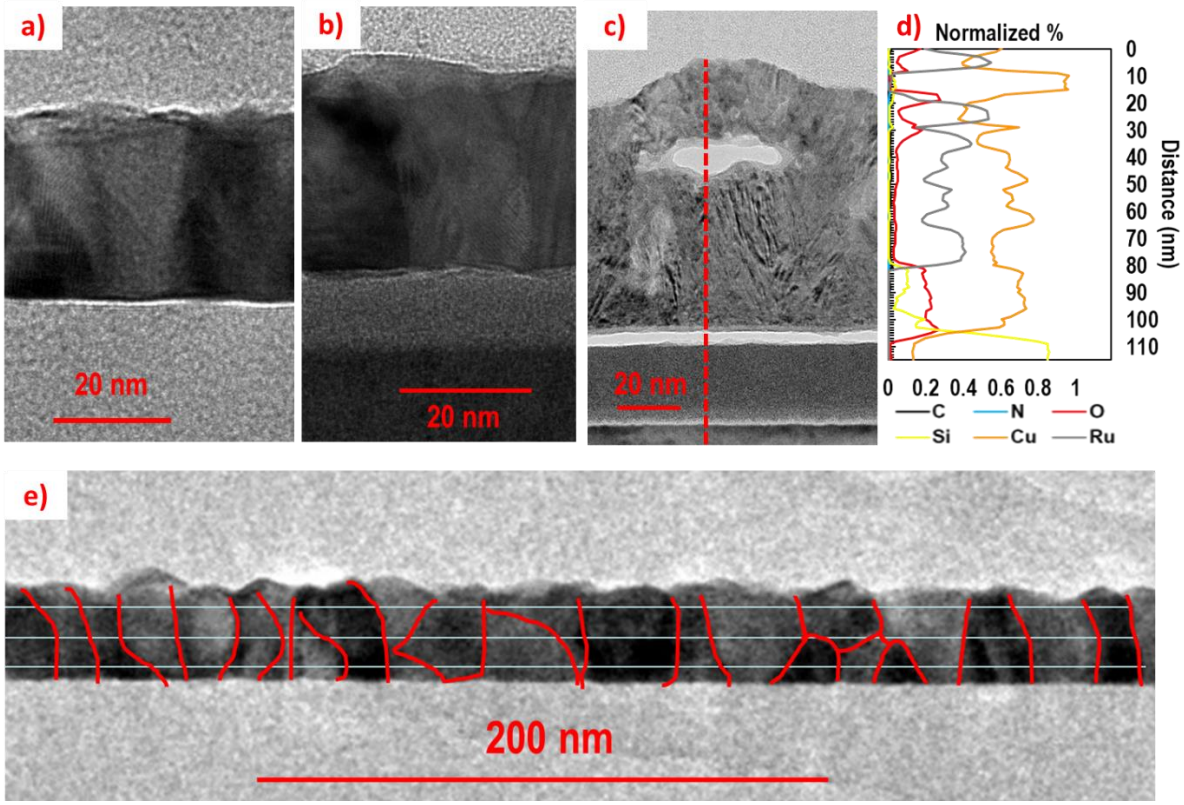

Figure 4.6: TEM of Ru ALD at 340 °C with $Ru(CpEt)_2$ + O_2 on SiO_2, W, and Cu. a) SiO_2 TEM. b) W TEM. c) Cu TEM and d) Cu EDS showing significant void formation and delamination from the underlying Cu surface along with Ru intermixing. e) Outline of grains across 400nm length of Ru film deposited on SiO2, showing mostly vertically-oriented grains.

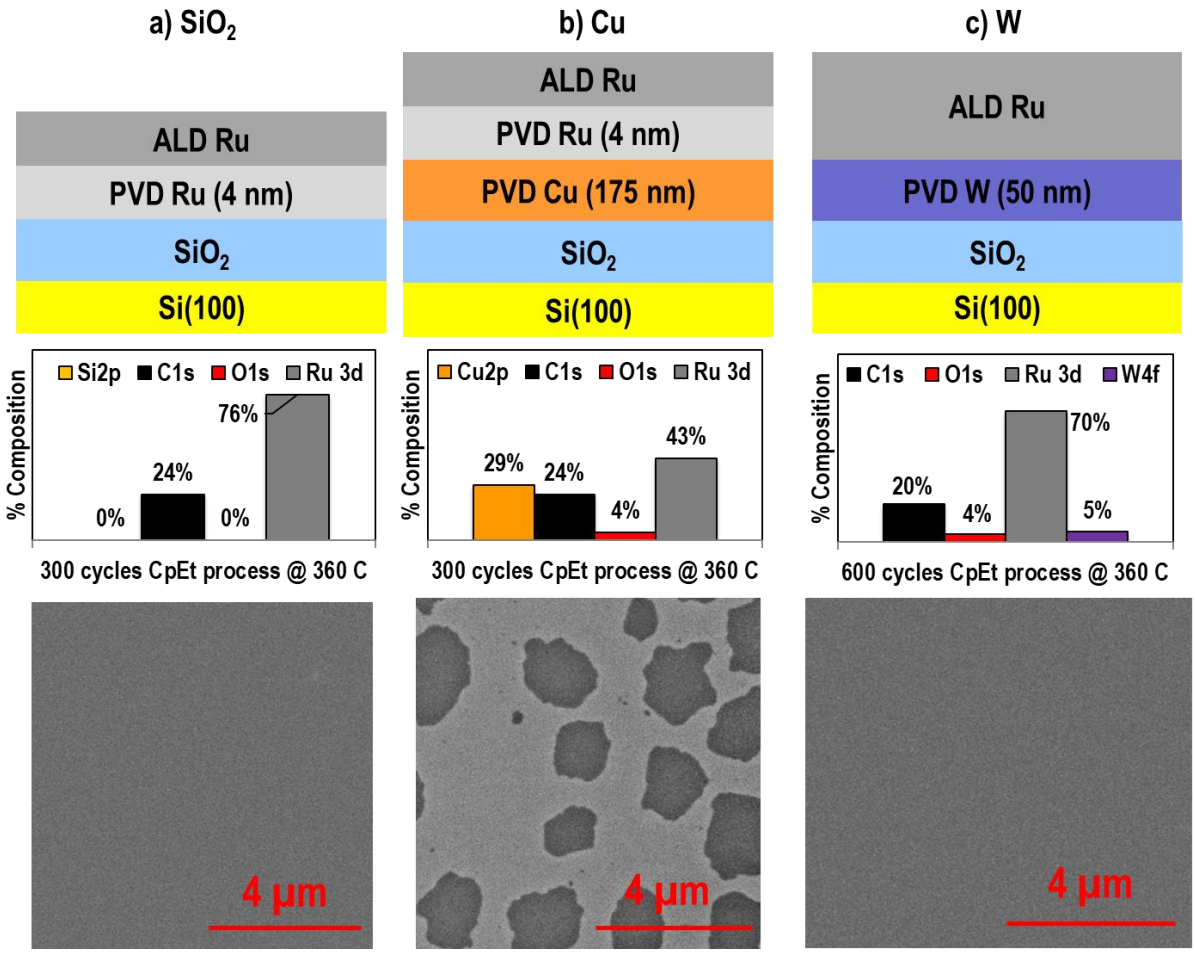

Figure 4.7: XPS and SEM of Ru ALD with $Ru(CpEt)_2 + O_2$ on PVD Ru/SiO_2, PVD W/PVD Cu/SiO_2, and PVD W/SiO_2 surfaces. a) ALD Ru on the PVD Ru seed layer on SiO_2 showing a uniform surface, with oxygen below detection limit in XPS and no visible Si substrate. b) ALD Ru on the PVD Ru seed layer on the Cu surface showing the presence of Cu on the surface in XPS, with SEM imagery showing voids in the film after deposition. c) ALD Ru on the PVD W surface showing a similar morphology to the SiO_2 surface after deposition, with a small amount of W consistent with pinholes formed due to incomplete native oxide clean.

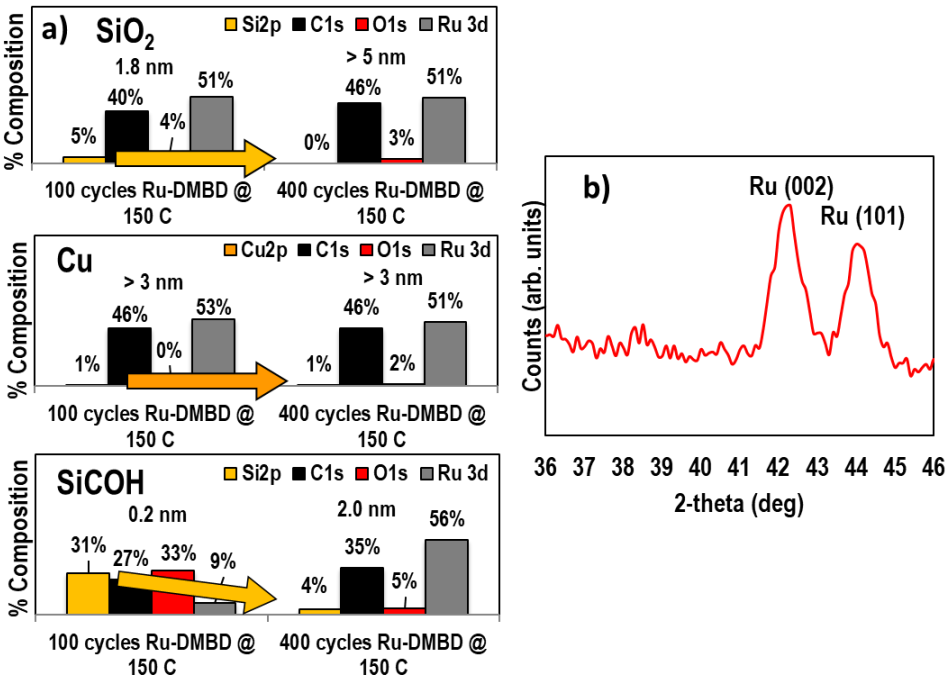

Figure 4.8: XPS of Ru ALD with Ru(DMBD)(CO)$_3$ + TBA on SiO$_2$, Cu, SiCOH. a) SiO$_2$ substrate completely attenuated by Ru ALD, while on Cu and SiCOH substrates are near-fully attenuated. b) XRD of the film after post-deposition forming gas anneal at 450 C shows a mix of (002) and (101) oriented grains of 11 and 12 nm respectively.

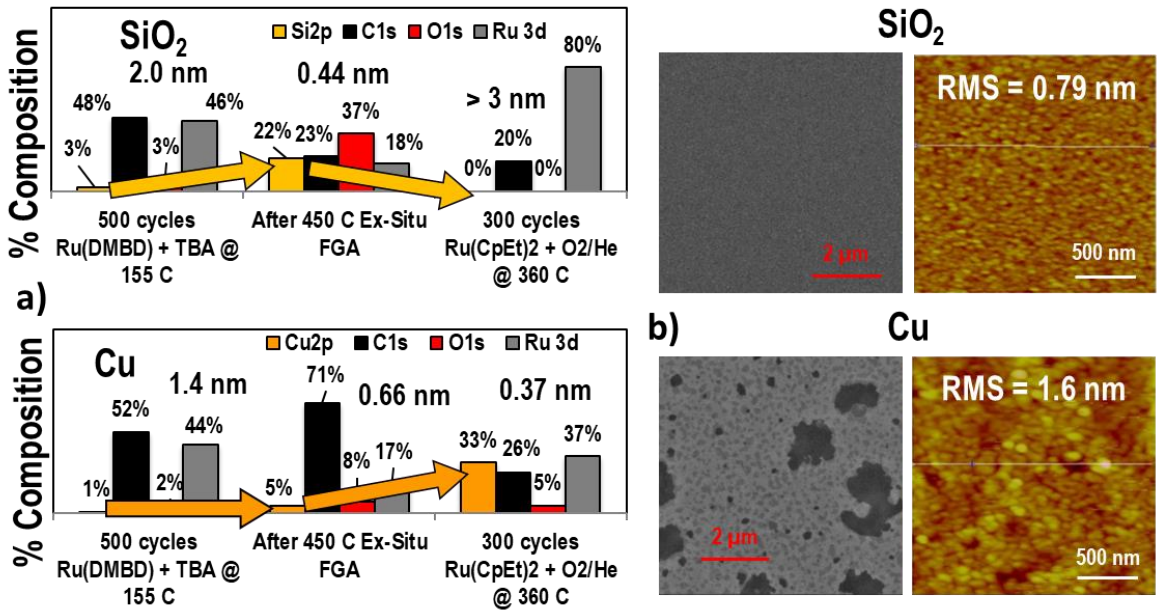

Figure 4.9: XPS/SEM/AFM of Ru ALD with the dual ALD process: seed DMBD process + FGA + enhancement CpEt process on SiO_2 and Cu. a) After 500 cycles of Ru ALD by the DMBD process at 155 °C, substrate attenuation was near-complete. The ex-situ 450 °C FGA caused a reduction in the film thickness, visible in XPS as increased substrate signal. Subsequently, 300 cycles of the CpEt process were deposited at 360 °C. b) SEM showed a uniform surface on SiO_2 compared with the surface of the Cu, which exhibited voids in the film due to de-wetting. AFM showed clear grains with sub-nanometer roughness on the SiO_2, while pinholes were visible in the Cu surface.

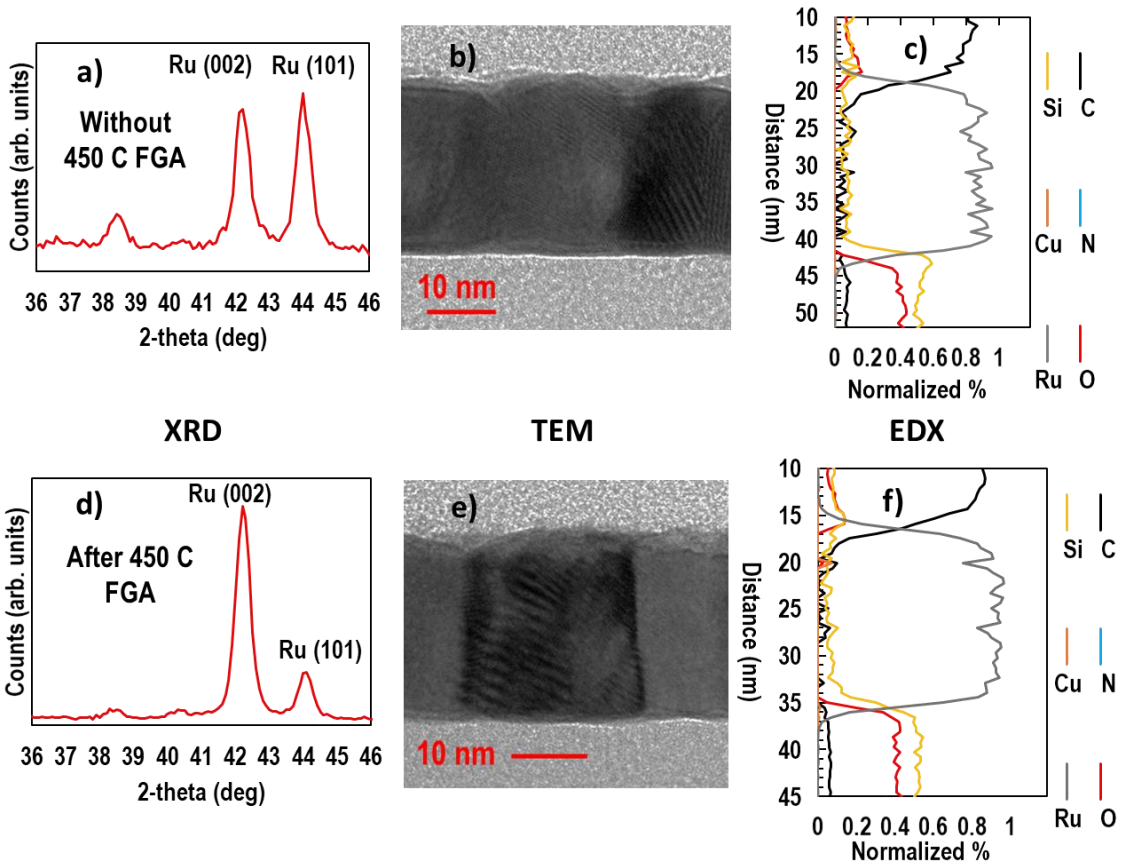

Figure 4.10: XRD/TEM/EDX of Ru ALD with the bi-layer ALD process: seed DMBD process + FGA + low-resistivity CpEt process on SiO_2. a) Without a post CpEt-process FGA, the relative intensities of the (002) and (101) oriented grains are similar, with grain sizes of 15 and 19 nm respectively. b) TEM image of the film showing both plane orientations c) TEM-EDX shows a layer of Ru 24 nm thick, with no detectible O and 4.8% C average in the film. b) With a post CpEt FGA, the (002) peak is heavily dominant, with grain sizes of 19 nm and 23 nm respectively. TEM shows a clearly defined grain roughly the film thickness in size, with no detectible O and an average C content of 2.4%.

4.7 REFERENCES

[1] L. Chen, N. Magtoto, B. Ekstrom and J. Kelber, *Effect of surface impurities on the Cu/Ta interface,* Thin Solid Films. 2020. **376**: pp. 115-123.

[2] D. Josell, S. H. Brongersma and Z. Tőkei, *Size-Dependent Resistivity in Nanoscale Interconnects,* Annual Review of Materials Research, **2009**. 39: pp. 231-254.

[3] D. Gall, *Electron mean free path in elemental metals,* J. Appl. Phys., 2016. **119**: p. 085101.

[4] M. Y. Kwak, D. H. Shin, T. W. Kang and K. N. Kim, *Characteristics of TiN barrier layer against Cu diffusion,* Thin Solid Films, 1999. **339**: pp. 290-293.

[5] M. Lane, R. H. Dauskardt, N. Krishna and I. Hashim, *Adhesion and reliability of copper interconnects with Ta and TaN barrier layers,* J. Mater. Res., 2011. **15**: pp. 203-211.

[6] M. H. van der Veen, M. Heylen, O. Varela Pedreira, I. Ciofi, S. Decoster, V. Vega Gonzalez, N. Jourdan, H. Struyf, K. Croes, C. J. Wilson and Z. Tokei, *Damascene benchmark of Ru, Co and Cu in scaled dimensions,* in Proc. of the IITC 2018, 2018.

[7] D. Gall, *The search for the most conductive metal for narrow interconnect lines,* J. Appl. Phys., 2020. **127**: p. 050901.

[8] O. Varela Pedreira, K. Croes, A. Lesniewska, C. Wu, M. H. van der Veen, J. de Messemaeker, K. Vandersmissen, N. Jourdan, L. G. Wen, C. Adelmann, B. Briggs, V. Vega Gonzalez, J. Bommels and Z. Tokei, *Reliability Study on Cobalt and Ruthenium as Alternative Metals for Advanced Interconnects,* in IEEE IRPS, 2017.

[9] G. Murdoch, Z. Tokei, S. Paolillo, O. Varela Pedreira, K. Vanstreels and C. J. Wilson, *Semidamascene interconnects for 2nm node and beyond,* in Proc. of the IITC 2020, Virtual, 2020.

[10] H. Y. Lee, Y. W. Hsieh, C. H. Hsu and K. S. Liang, *Characteristics of sputter-deposited Ru thin films on Si substrates,* Mater. Chem. and Phys., 2003. **82**: pp. 984-990.

[11] M. L. Green, M. E. Gross, L. E. Papa, K. J. Schnoes and D. Brasen, *Chemical Vapor Deposition of Ruthenium and Ruthenium Dioxide Films,* J. Elec. Soc., 1985. **132**: p. 2677.

[12] R. Khan, B. Shong, B. G. Ko, J. K. Lee, J. Y. Park, I. Oh, S. S. Raya, H. M. Hong, K. Chung, E. J. Luber, Y. Kim, C. Lee, W. Kim and H. Lee, *Area-selective atomic layer deposition using Si precursors as inhibitors,* Chem. Mater., 2019. **30**: pp. 7603-7610.

[13] A. J. M. Mackus, M. J. M. Merkx and W. M. M. Kessels, *From The Bottom-Up: Toward Area-Selective Atomic Layer Deposition with High Selectivity*, Chem. Mater., 2019. **31**: pp. 2-12.

[14] T. Aaltonen, P. Alen, M. Ritala and M. Leskela, *Ruthenium thin films grown by atomic layer deposition,* Chem. Vapor Dep., 2009. **9**: pp. 45-49.

[15] W. H. Kim, S. J. Park, D. Y. Kim and H. Kim, *Atomic layer deposition of ruthenium and ruthenium-oxide thin films by using a $Ru(EtCp)_2$ precursor and oxygen gas,* J. Korean Phys. Soc., 2009. **55**: p. 32.

[16] M. Popovici, B. Groven, K. Marcoen, Q. Phung, S. Dutta, J. Swerts, J. Meersschaut, J. A. van den Berg, A. Franquet, A. Moussa, K. Vanstreels, P. Lagrain, H. Bender, M. Jurczak, S. V. Elshocht, A. Delabie and C. Adelmann, *Atomic Layer Deposition of Ruthenium Thin Films from (Ethylbenzyl) (1-Ethyl-1,4-cyclohexadienyl) Ru: Process Characteristics, Surface Chemistry, and Film Properties*, Chem. Mater., 2017. **29**: pp. 4654-4666.

[17] S. S. Yim, D. J. Lee, K. S. Kim, S. H. Kim, T. S. Yoon and K. B. Kim, *Nucleation kinetics of Ru on silicon oxide and silicon nitride surfaces*, J. Appl. Phys., 2008. **103**: p. 113509.

[18] Z. Gao, D. Le, A. Khaniya, C. L. Dezelah, J. Woodruff, R. K. Kanjolia, W. E. Kaden, T. S. Rahman and P. Banerjee, *Self-Catalyzed, Low-Temperature Atomic Layer Deposition of Ruthenium Metal Using Zero-Valent $Ru(DMBD)(CO)_3$ and Water,* Chem. Mater., 2019. **31**: pp. 1304-1317.

[19] J. H. Scofield, *Hartree-Slater subshell photoionization cross-sections at 1254 and 1487 eV*, J. Elec. Spectroscopy and Rel. Pheno., 1976. **8**: pp. 129-137.

[20] D. Morgan, *Resolving ruthenium: XPS studies of common ruthenium materials*, Surf. Interface Anal., 2015. **47**: pp. 1072-1079.

[21] D. S. Perloff, *Four-point sheet resistance correction factors for thin rectangular samples*, Solid-State Elec., 1977. **20**: pp. 681-687.

[22] A. Patterson, *The Scherrer formula for X-ray particle size determination*, Phys. Rev., 1939. **56**: p. 978.

[23] A. Jog and D. Gall, *Resistivity size effect in epitaxial iridium layers*, J. Appl. Phys, 2021. **130**: p. 115103.

[24] A. Jog and D. Gall, *Electron scattering at surface and grain boundaries in Rh layers*, IEEE Trans. Elec. Dev., 2022 *(in press)*. pp. 1-7.

[25] E. Milosevic, S. Kerdsongpanya, A. Zangiabadi, K. Barmak, K. R. Coffey and D. Gall, *Resistivity size effect in epitaxial Ru(0001) layers*, J. Appl. Phys, 2018. **124**: p. 165105.

[26] E. Milosevic, S. Kerdsongpanya, M. E. McGahay, A. Zangiabadi, K. Barmak and D. Gall, *Resistivity scaling and electron surface scattering in epitaxial Co(0001) layers*, J. Appl. Phys, 2019. **125**: p. 245105.

[27] M. Hayes, M. A. Jenkins, J. Woodruff, D. F. Moser, C. L. Dezelah and J. F. Conley, Jr. , *Improved properties of atomic layer deposited ruthenium via postdeposition annealing,* J. Vac. Sci. Technol., 2021. **39**: p. 052402.

[28] P. J. Cumpson, *The Thickogram: a method for easy film thickness in XPS,* Surf. Interface Anal., 2000. **29**: pp. 403-406.

[29] R. W. Powell, R. P. Tye and M. J. Woodman, *The thermal conductivity and electrical resistivity of polycrystalline metals of the platinum group and of single crystals of ruthenium,*" J. Less Common Met., 1967. **12**: pp. 1-10.

[30] C. W. Chen, J. S. Jeng and J. S. Chen, *Comparative study of Cu diffusion in Ru and Ru-C films for Cu Metallization,* J. Elec. Chem. Soc., 2010. **157**(11): pp. G997-H1002.

[31] M. Damayanti, T. Sritharan, S. G. Mhaisalkar, H. J. Engelmann, E. Zschech, A. V. Vairagar and L. Chan, *Microstructural evolution of annealed ruthenium-nitrogen films,* Electrochem. and Solid State Lett., 2007. **10**(6): pp. P15-P17, 2007.

[32] D. M. Solina, R. W. Cheary, F. A. Lupscha and P. D. Swift, *An investigation of metal thin films using X-ray reflectivity and atomic force microscopy,* Adv. X-ray Anal., 1997. **40**.

[33] C. C. Tang and D. W. Hess, *Tungsten etching in CF_4 and SF_6 discharges,* Solid State Sci. and Tech., 1984. **131**(1): pp. 115-119.

[34] L. Vitos, A. V. Ruban, H. L. Skriver and J. Kollar, *The surface energy of metals,* Surf. Sci., 1998. **411**: pp. 186-202.

[35] S. Wolf, M. Breeden, S. Ueda, J. Woodruff, M. Moinpour, R. Kanjolia and A. Kummel, *The role of oxide formation on insulating versus metallic substrates during Co and Ru selective ALD,* Appl. Surf. Sci., 2020. **510**: p. 144804.